Transport in Ionic Liquid Gated and Superconducting Nanostructures

A THESIS
SUBMITTED TO THE FACULTY OF THE GRADUATE SCHOOL
OF THE UNIVERSITY OF MINNESOTA
BY

Terence Michael Bretz-Sullivan

IN PARTIAL FULFILLMENT OF THE REQUIREMENTS
FOR THE DEGREE OF
DOCTOR OF PHILOSOPHY

ALLEN M. GOLDMAN

August, 2016

Acknowledgements

I would first like to thank my friends and fellow graduate students.

I thank my past and present labmates for their assistance. Without my fellow Goldman lab members, past and present, I would not know the experimental techniques I know now. This list includes JJ Nelson, Joe Kinney, Boyi Yang, Ilana Percher, Joe Sobek, Javier Garcia Barriocanal, Stephen Synder, Yen-Hsiang Lin, and Xiang Leng.

I would like to thank Bryan Cord, Mark Fisher, Lage von Dissen, Kevin Roberts, Paul Kimani and Greg Haugstad at the Minnesota Nanofabrication Center and the Characterization Facility for teaching me the techniques and tricks of nanofabrication and scanning probe microscopy.

I would like to thank the CSE Machine Shop members: Mike Jensen, Ron Bystrom, Jon Kilgore and George Derks, and Bill Voje for liquifying helium for our experiments. I would also thank Shelley Frankel, Amy Nordlander, and Julie Murphy for their assistance with purchasing and administrative tasks.

I thank my advisor Allen Goldman for his encouragement and patience during my years in graduate school, and Alex Kamenev for his assistance and useful theory discussions. I also thank my committee members Paul Crowell, for use of the Helium-3 refrigerator insert, and Bharat Jalan.

I also thank our funding agencies. This work was supported by the U.S. Department of Energy Basic Energy Sciences Grant No. DE-FG0202ER46004. Samples were fabricated at the Minnesota Nanofabrication Center. Parts of this work were carried out at the University of Minnesota Characterization Facility, a member of the Materials Research Facilities Network funded via the NSF MRSEC program through Grant No. DMR-1420013.

Dedication

To my parents, Tom and Clare.

Abstract

Electrons, when subjected to low temperatures and to very short length scales, exhibit an array of unique quantum mechanical properties. In order to access this regime, one needs cryogenic measurement and nanofabrication techniques. Both experiments in this thesis, which were performed on nanoscale devices, used a ^3He cryostat to access low temperatures, and electron beam lithography to fabricate the devices. The first experiment focused on electron tunneling and transport in ionic liquid gated narrow channels (nanowires) of strontium titanate while the second experiment focused on transport in superconducting aluminum nanowires and magnetic field tuned reentrant superconductivity.

Measurements of the current-voltage ($I - V$) characteristics of ionic liquid gated nanometer scale channels of strontium titanate have been carried out. At low gate voltages, the $I - V$ characteristics exhibited a large voltage threshold for conduction and a nonlinear power law behavior at all temperatures measured. The source-drain current of these nanowires scaled as a power law of the difference between the source-drain voltage and the threshold voltage. The scaling behavior of the $I-V$ characteristic is reminiscent of collective electronic transport through an array of quantum dots. At large gate voltages, the narrow channel acts as a quasi-1D wire whose conductance follows Landauer's formula for multichannel transport.

Reenterant superconductivity in quasi-one dimensional superconductors, through the application of a magnetic field, is a counter-intuitive phenomenon. It was not until recently that a microscopic mechanism describing the phenomenon was developed in which superconductivity and phase slip driven dissipation coexist in a non-equilibrium state. Here we present new results on magnetic field induced reentrance to superconductivity in quasi-1D aluminum nanowires for in-plane magnetic fields both transverse to and longitudinal along the wire axis. Measurements in the transverse field configuration result in an abrupt transition into the superconducting state as well as quantized behavior related to the flux quantum in an area determined by the product of the distance between voltage probes and the film thickness. These results are different from those

found for the case of a perpendicular field, suggesting that different mechanism may be involved.

Contents

List of Tables

List of Figures

Chapter 1

Introduction

The physics of ionic liquid gated and superconducting nanowires is a rich area of research. At low temperatures and narrowly confined length scales, electrons and Cooper pairs exhibit a wonderful array of quantum mechanical phenomenon attributable to their discrete charge, wave nature and macroscopic phase coherence. Beginning in the early 1980s, this area of condensed matter physics became known as mesoscopic physics. Mesoscopic physics involves studies of devices whose characteristic size is sandwiched between atomic and macroscopic length scales.[1] The results of this area of research have not only provided fundamental physics results but have spawned advances in the microprocessor industry. In recent years, there has been a resurgence of research in superconducting nanostructures because they serve as the basic circuit elements and interconnects of superconducting qubits.[2, 3]

The two experiments I carried out and whose results I present in this thesis focus on electron tunneling and transport in ionic liquid gated narrow channels (nanowires) of strontium titanate ($SrTiO_3$) while the second on transport in superconducting aluminum nanowires. The common theme amongst both experiments is that they were fabricated by electron beam lithography and measured at low temperatures.

I begin by reviewing the theory of transport in single and arrays of quantum dots and quasi-1 dimensional normal state quantum wires. These theories are relevent to the results from my ionic liquid gating experiment. Then, I will discuss the physics of the bulk superconducting state and of quasi-1 dimensional superconductors. Following this, I will explain how I designed, fabricated and measured both narrow channels

on $SrTiO_3$ and superconducting aluminum nanowires. Finally, I will present data from both experiments on ionic liquid gated nanowire project and superconducting nanowires and discuss the observed effects.

Chapter 2

Physics of Quantum Dots and Quantum Wires

In this chaper, I will present the theoretical aspects of transport through quantum dots and quantum wires. I begin by treating transport through single quantum dots. Then, I explain the theory of Alan Middleton and Ned Wingreen on transport through arrays of quantum dots. I finish the chapter with a discussion of transport through quantum wires.

2.1 Transport in Single Quantum Dots

A quantum dot (QD) is a small metallic or semiconductor island in which the motion of the conduction electrons is confined in three dimensions. QDs thus exhibit discrete energy states just like an atom, due to this electron confinement. On the other hand, a quantum wire (QW) is a small metallic or semiconductor narrow channel in which the motion of its electrons is confined in two dimensions. QDs and QWs are typically refered to as 0-dimensional (0D) and 1-dimensional (1D) structures respectively. I begin with a discussion of transport through a single QD. Then I will expand the discussion of the physics of QDs when many QDs are strung together into an array and examine the role of frozen-in, or quenched disorder on electrical transport. Finally, I will examine electrical transport in QWs in terms of the Landauer formalism.

The name QD was originally coined by Mark Reed at Texas Instruments in 1988.[4]

It is a physical example of the textbook "particle in a box" problem every physics student encounters in the first quantum mechanics course. One observes the effects of the QD's quantized energy levels in electrical transport measurements provided the QD is within the Coulomb Blockade (CB) regime. To begin, we examine what an ideal, single QD "looks like" schematically as seen in Figure 2.1. I will stick to the description of QD transport given by Kouwenhoven *et al.* throughout this chapter.[5]

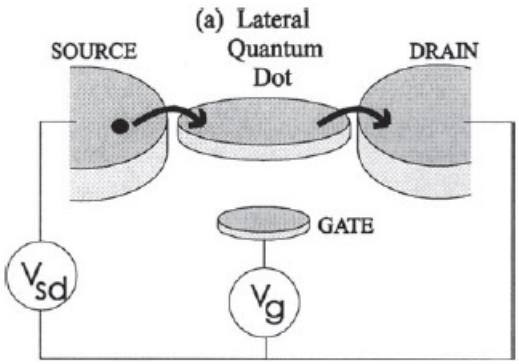

Figure 2.1: A schematic circuit of a QD.[5]

Figure 2.1 is a schematic of an idealized QD connected to a source-drain voltage (V_{sd}) and gate voltage (V_g). We first assume that the QD is only capacitively coupled to the gate electrode. The QD acts as an island for conduction electrons. Because the QD has discrete energy states, applying V_g populates or depopulates the island in integral charge units. Therefore, we can change the number of electrons on the QD a single electron at a time. The QD is populated with N electrons and carries a total charge of $Q_{total} = Ne$ where $e = 1.602 \times 10^{-19}$ Coulombs.

What happens when we bias the QD with V_{sd}? Electrons tunnel from the source electrode to one of the QD's energy levels and then tunnel from the QD to the drain electrode as portrayed by the arrows of Figure 2.1. Charges tunnel to minimize the total electrostatic energy of the circuit. However, to observe tunneling processes within the CB regime, one must satisfy the following conditions

$$R_t \gg \frac{h}{e^2} = 25.813\,k\Omega \tag{2.1}$$

$$E_c = \frac{e^2}{C} \gg k_B T \tag{2.2}$$

R_t is the tunneling resistance between the source and drain electrodes to the QD, h is Planck's constant, e the electron charge, E_c is the QD's charging energy, k_B is Boltzmann's constant, and T is the temperature. E_c is the Coulomb interaction energy between two electrons on the dot. For simplicity, it is typically taken to only depend on the self-capacitance of the dot. Assuming the dot is spherically symmetric for simplicity, $C = 4\pi\epsilon_o\epsilon R$ where $\epsilon_0 = 8.85 \times 10^{-15}$ F/m, ϵ is the dielectric constant of the surrounding material, and R is the radius of the sphere. However, I will later include a more general form for C to describe the transport properties. We can derive Equation 2.1 from a simple Heisenberg uncertainty principle argument.

The timescale for tunneling to and from the QD from the source and drain electrodes is of the order of $\delta t \approx R_t C$. From the energy-time version of the uncertainty principle, we have $\delta E \times \delta t \approx (e^2/C)(R_t C) > h$. Equation 2.2 states that E_c must be the dominant energy scale in the problem. Thus, the rule of thumb for a QD to satisfy Equation 2.1 and Equation 2.2 is to make the dimensions of the QD smaller than the Fermi wavelength of electrons on the dot, to surround it by a high dielectric constant material, and to measure its transport properties at very low temperatures.

Let us now examine what the conductance (G) as a function of V_g and the $I_{sd} - V_{sd}$ characteristic of a single QD device look like. Both measurements are a probe of the energy levels of the QD. The observed lineshapes in $G(V_g)$ are known as Coulomb oscillations and the Coulomb staircase in the $I_{sd} - V_{sd}$ characteristic are shown in Figures 2.2 and 2.3 respectively.

Let us first investigate the microscopic origin of the Coulomb oscillations in $G(V_g)$. It is helpful to consider the schematic of a QD in Figure 2.4 (a-c) to visualize the process. The black rectangles represent charge reservoirs while the taller, white rectangles represent tunnel barriers sandwiched on either side of a QD. We begin with blockaded transport in Figure 2.4a at $T = 0$.

The QD is populated up to an electrochemical potential $\mu_{dot}(N)$, with an energy level spacing ΔE. $\mu_{dot}(N) = U(N) - U(N-1)$ where $U(N)$ is the total ground state energy of the QD. As seen in Figure 2.4a, at a fixed N, the energy difference between the lowest unoccupied state and highest occupied state is

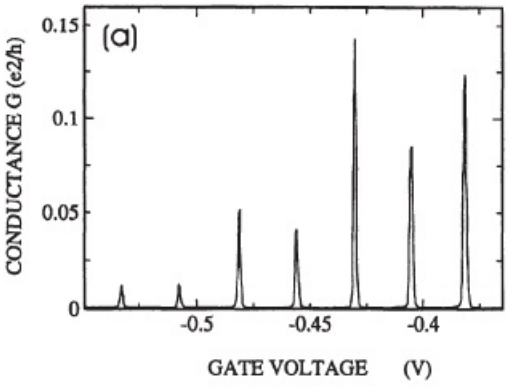

Figure 2.2: Coulomb oscillations in $G(V_G)$.[5]

$$\mu_{dot}(N+1) - \mu_{dot}(N) = \Delta E + E_c \tag{2.3}$$

E_c is only present between $\mu_{dot}(N+1)$ and $\mu_{dot}(N)$. The value of ΔE below $\mu_{dot}(N)$ and above $\mu_{dot}(N+1)$ is assumed to be constant and equal to $\Delta E_{N+1} - \Delta E_N$. The E_N are single particle energies which are measured from the bottom of the conduction band and depend on the details of the boundary conditions.

Let us apply $V_{sd} = (\mu_{left} - \mu_{right})/e$ where $\mu_{left,right}$ are the electrochemical potentials of the left and right leads respectively. Electrons will tunnel from the source electrode to the dot and from the dot to the drain electrode provided there are accessible energy levels within the V_{sd} window. However, if there are no accessible levels, transport through the QD is blockaded as seen in Figure 2.4a. Hence, the need to overcome $\Delta E + E_c$ and the name Coulomb Blockade (CB). The CB is overcome by either increasing V_{sd} to $\mu(N+1)$ or sweeping V_g with a small V_{sd} bias through the different energy levels. Coulomb oscillations result from the latter process while the Coulomb staircase results from the former.

Let us now take a more general form for C in terms of the circuit diagram in Figure 2.1. Now $C = C_l + C_r + C_g$ where C_l is the capacitance between the source electrode (left electrode in Figure 2.1) and the QD, C_r is the capacitance between drain electrode (right electrode in Figure 2.1) and the QD, and C_g is the capacitance between the gate electrode and the QD. In addition, provided $V_{sd} \ll \Delta E/e, e/C$, $\mu_{dot}(N)$ takes the form

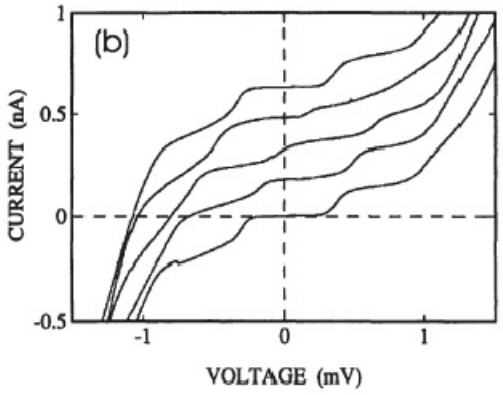

Figure 2.3: Coulomb staircase in the $I_{sd} - V_{sd}$ characteristic.[5]

$$\mu_{dot}(N) = E_N + (N - N_0 - 1/2)e^2/C - e(C_g/C)V_g = \mu_{chemical}(N) + e\phi_N \qquad (2.4)$$

Here $\mu_{chemical}(N) = E_N$, N_0 is number of electrons on the dot when $V_g = 0V$, and ϕ_N is the electrostatic potential of the dot. The electrostatic potential of the dot, ϕ_N, contains two parts, a discrete component and a continious component.

$$e\phi_N = e\phi_{N,discrete} + e\phi_{N,continous} = (N - N_0 - 1/2)e^2/C - e(C_g/C)V_g \qquad (2.5)$$

$\phi_{N,discrete}$ depends strictly on the number of charges on the QD while $\phi_{N,continous}$ does not depend on N.

Next, we sweep V_g through the different charge state configurations with $(...N - 1, N, N + 1...)$. We consider what happens when we align $\mu_{dot}(N + 1)$ in the window between μ_{left} and μ_{right} as seen in Figure 2.4(b),(c). An electron tunnels onto the dot from the source electrode Figure 2.4b. The QD's electrostatic energy increases by E_c while the electron resides on the dot. The energy of the QD then returns to $\mu_{chemical}(N)$ when the electron tunnels to the drain electrode. Therefore, within this electrochemical potential window, a stable configuration of both N and $N + 1$ exists. This is known as the charge degeneracy point. Each time the QD electron population transitions between

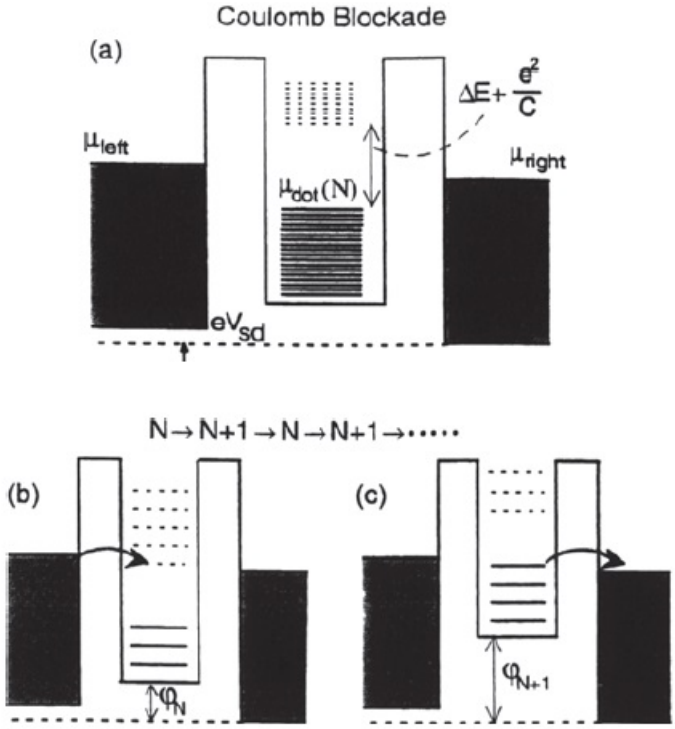

Figure 2.4: Energy schematic of an idealized QD.[5]

N and $N+1$, we observe a peak in the G vs. V_g as seen in Figure 2.2. However, if we are between the QD's energy levels, within the blockaded region, $G = 0$.

The peaks in $G(V_g)$ are periodic in V_g and have an intrinsic linewidth. We determine the periodicity of $G(V_g)$ from the following condition

$$\mu_{dot}(N, V_g) = \mu_{dot}(N+1, V_g + \Delta V_g) \tag{2.6}$$

It follows from Equation 2.6, that the spacing between peaks and position of the peaks are

$$\Delta V_g = \frac{C}{eC_g}(\Delta E + \frac{e^2}{C}) \tag{2.7}$$

$$V_g(N) = \frac{C}{eC_g}(\Delta E + (N - 1/2)\frac{e^2}{C}) \tag{2.8}$$

The functional form of $G(V_g, T)$ depends on the temperature regimes of which there are three. In addition, we must also consider the intrinsic broadening of the QD's energy levels $\delta E = h\Gamma$. For each of the following cases, we assume that $h\Gamma \ll k_B T$. The results are summarized in Table 2.1.[5]

Temperature limit	Constraint	Discrete charge transport?
High Temp.	$e^2/C \ll k_B T$	No, check Equation 2.2
Classical CB	$\Delta E \ll k_B T \ll e^2/C$	Yes, through several energy levels
Quantum CB	$k_B T \ll \Delta E \ll e^2/C$	Yes, through a single energy level

Table 2.1: Coulomb Blockade temperature regime table.

The high temperature limit is obvious considering it does not satisfy the necessary conditions for the CB, Equation 2.1 and Equation 2.2. In this case, G is just the series sum of the conductances of both the two barriers.

$$G = G_\infty = \frac{G_{left} G_{right}}{G_{left} + G_{right}} \tag{2.9}$$

In the classical CB limit, the functional form of $G(V_g, T)$ is

$$\frac{G(V_g, T)}{G_\infty} = \frac{1}{2}\cosh^{-2}(\frac{\delta}{2.5 k_B T}) \tag{2.10}$$

where $\delta = e(C_g/C)|V_{res} - V_g|$ is the distance from the center position of the resonance peaks and V_{res} is the gate voltage at peak center. Figure 2.5 is a plot of $G(\Delta E_F/E_c)/G_\infty$ at different $k_B T/E_c$ ratios. The microscopic calculation assumes a constant density of states and constant barrier conductances.

At the lowest temperature, in (a),(b), $G_{max} = G_\infty/2$ and the width of the line-shape decrease linearly with temperature. As we decrease the temperature further until $k_B T \ll \Delta E \ll e^2/C$, we enter the quantum CB regime. In this case, the single peak $G(V_g, T)$ takes the form

$$\frac{G(V_g, T)}{G_\infty} = \frac{\Delta E}{4 k_B T}\cosh^{-2}(\frac{\delta}{2 k_B T}) \tag{2.11}$$

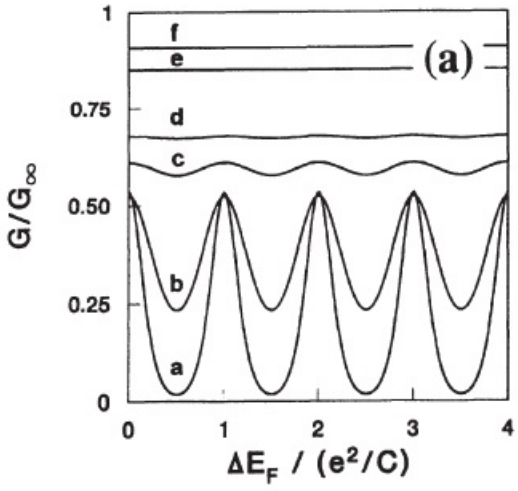

Figure 2.5: Calculated Coulomb oscillations in the classical regime. The different values, $(a, b, c, d, e, f) = (0.075, 0.15, 0.3, 0.4, 1, 2)$, are in units of k_BT/E_c.[5]

where δ is the same variable as in Equation 2.10. Both the classical and quantum regimes have a similar functional form. However, the peak heights, $G_{peak}(T)$, in the classical and quantum regimes exhibit a different temperature dependence.

In the classical regime, $G_{peak}(T) = G_\infty/2$. However, in the quantum regime, $G_{peak} \sim 1/T$. Figure 2.6 is a plot of $G(T)$ in the quantum regime.

A final comment relates to the role of the QD's energy level broadening. What happens to the $G(V_g, T)$ when we include energy level broadening of a finite width $h\Gamma$ and a regime where $h\Gamma \approx k_BT$? In this case, $G(V_g, T)$ takes on a resonant tunneling or Breit-Wigner tunneling form.

$$G_{BW}(V_g, T = 0) = \frac{2e^2}{h} \frac{(h\Gamma)^2}{(h\Gamma)^2 + (\delta)^2} \tag{2.12}$$

Here δ is again the same functional form as in Equation 2.10 and Equation 2.11. Equation 2.12 assumes non-interacting electrons and equal barrier conductances. At finite temperature, we convolute Equation 2.12 with the derivative of the Fermi-Dirac distribution function of the source electrode $(\partial f/\partial E)$ to get

$$G(V_g, T) = \int dE\, G_{BW}(V_g, T = 0)(-\partial f/\partial E) \tag{2.13}$$

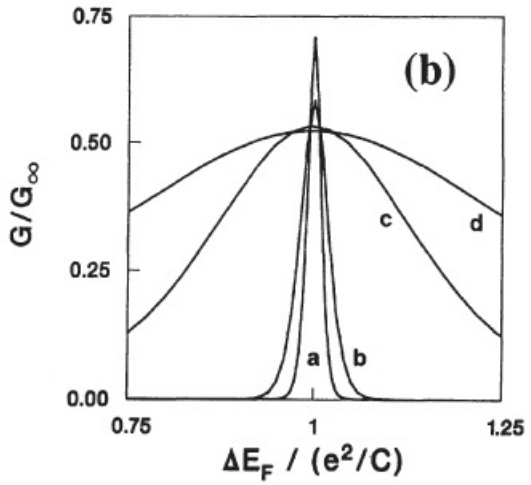

Figure 2.6: Calculated Coulomb oscillations in the quantum regime. $\Delta E = 0.01e^2/C$ and $(a, b, c, d) = (0.5, 1, 7.5, 15)$ in units of $k_BT/\Delta E$.[5]

Both the Equation 2.11 and Equation 2.12 have been experimentally verified in a single QD formed by electrostatically gating a GaAs/$Al_xGa_{1-x}As$ two-dimensional electron gas (2DEG) as seen in Figure 2.7 and Figure 2.8.

Let us now focus on briefly the other method for overcoming the CB. This is done by holding V_g constant and sweeping V_{sd}. By doing this one observes the Coulomb staircase in the $I_{sd} - V_{sd}$ characteristic as seen in Figure 2.3.

To keep it simple, we first consider the classical CB case with an asymmetric barrier as seen in Figure 2.9. With a strong asymmetric barrier, μ_{right} is essentially fixed with respect to μ_{left}.

As we increase $V_{sd} = (\mu_{left} - \mu_{right})/e$ from $\mu_{dot}(N)$ up to $\mu_{dot}(N + 1)$, charges can tunnel through the accessible state. In the $I_{sd} - V_{sd}$ characteristic, the current is initially zero until $V_{sd} \approx e/C$ when $\mu_{dot}(N + 1)$ becomes accessible. Each time a new charge state is accessed, the $I_{sd} - V_{sd}$ characteristic experiences a current rise due to the added conduction channel. In between energy levels, there is a constant current step as seen in Figure 2.3. Therefore, we ascend the Coulomb staircase. In the quantum CB case, the $I_{sd} - V_{sd}$ characteristic is roughly the same. However, in the quantum CB case, one can map out the energy level spacing,ΔE, in a spectroscopic sense. The caveat

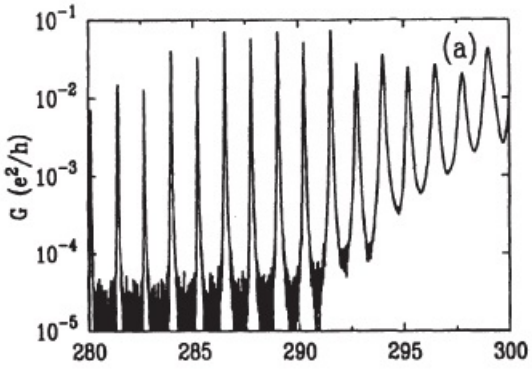

Figure 2.7: $G(V_g)$. Coulomb oscillations in an electrostatically gated 2DEG. The x-axis V_g in units of mV.[6]

of ascending the Coulomb staircase is that quantitative analysis is hampered because there is no functional form like for $G(V_g, T)$ as discussed earlier.

2.2 Transport in Arrays of Quantum Dots

In the previous section, we saw what happens when one probes the the electrical properties of a single QD in the CB regime. But what happens when we string QDs together in a periodic array and add static (quenched) disorder to the problem? The theory of charge transport transport in such arrays of metallic QDs was worked out by Middleton and Wingreen (MW) in 1993 and is the focus of this section.[7] What emerges is collective charge transport through the QD array. An elastic charge interface propagates through the array as a function of V_{sd}. Interestingly it leads to an $I_{sd} - V_{sd}$ characteristic which exhibits scaling behavior like that in critical phenomenon.[45] Thus,

$$I_{sd} \sim (V_{sd}/V_T - 1)^{\zeta} \tag{2.14}$$

V_T is the voltage threshold for conduction and ζ is the scaling exponent which is either $\zeta_{1D} = 1$ or $\zeta_{2D} = 5/3$ depending on the dimensionality of the QD array. What is key in MW's theory is that the QD array essentially exhibits a dynamical phase transition which is seen in the scaling behavior of Equation 2.14. The array

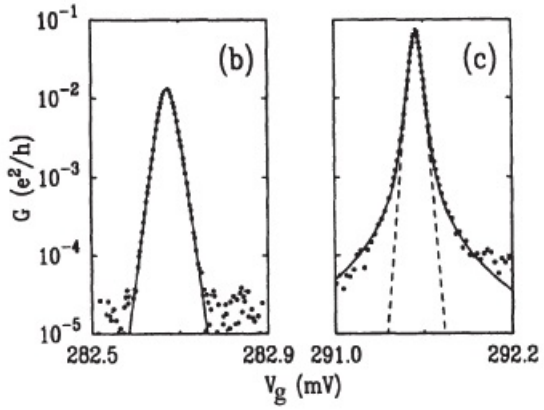

Figure 2.8: Coulomb oscillations fit to Equation 2.11 (b) and thermally broadened Coulomb oscillations fit to Equation 2.13 (c).[6]

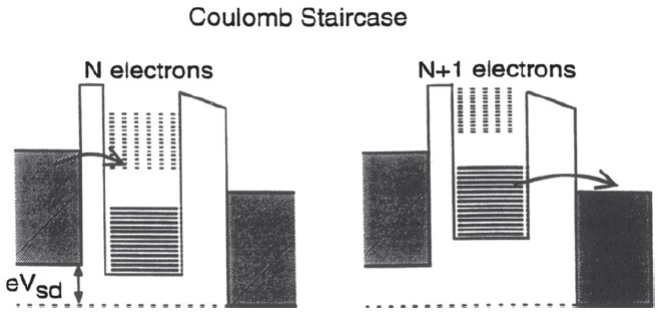

Figure 2.9: Coulomb staircase with an asymmetric QD.[5]

transitions from a static, non-conducting state to a dynamic, conducting state by tuning V_{sd}. Conduction through the array does not occur until V_{sd} exceeds V_T.

In general, 1D and 2D arrays are denoted by N or $N \times N$ for the number of QDs contained in the array. In this case, N is not the number of electrons on the dot as defined in the previous section. Figure 2.10 is a schematic of a 4×4 array. Each QD is denoted as a square in the array.

The array is situated between source and drain electrodes denoted V_L, V_R and placed on top of a back gate outlined by the large dashed line square and denoted by V_g. Each dot is capacitively coupled to its neighbors, V_L, and V_R with a capacitance C and

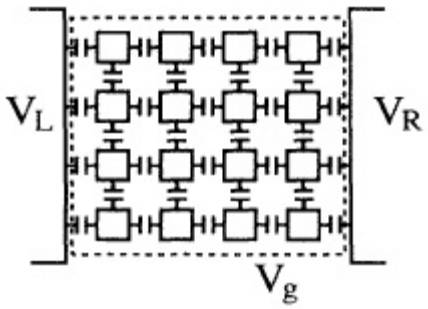

Figure 2.10: A 4×4 QD array. V_L and V_R are the source and drain electrodes. V_g is the gate coltage electrode which underlies to array (large dashed square).[7]

capacitively coupled to the back gate by C_g. The total energy of the array is purely electrostatic and is

$$E = \frac{1}{2} \sum_{dots\ i,j} (Q_i + q_i) C^{-1}_{i,j} (Q_j + q_j) + V_L Q_L + V_R Q_R + \sum_{dots\ i} V^{ext}_i Q_i \tag{2.15}$$

Q_i is the charge on the i^{th} dot and q_i represents an effective charge on the QD due to nearby ionized impurities. q_i is a measure of local quenched disorder in the model. $C_{i,j}$ are elements of an $N \times N$ capacitance matrix. Typically, $C^{-1}_{i,j} \sim \exp(-\lambda)$ where λ is the characteristic electrostatic screening length of the array. In general, if $(C/C_g) \to 0$ then $\lambda \to 0$ and if $C \gg C_g$ then $\lambda \to (C/C_g)^{1/2}$. The products $V_{L(R)} Q_{L(R)}$ are contributions to the total electrostatic energy from electrons in the source and drain electrodes. The last term in Equation 2.15 is the electrostatic potential contribution from the L, R, g leads to the charge on the i^{th} dot.

Following the MW prescription, let us consider an electron tunneling from $i \to j$ only when it lowers the total electrostatic energy of the array, Equation 2.15. The electron's kinetic energy gained by tunneling is assumed to be dissipative. The MW theory considers a transition between array charge configurations $S = (..., Q_i, ..., Q_j, ...)$ and $S' = (..., Q_i - 1, ..., Q_j + 1, ...)$, using Fermi's Golden Rule to calculate the transition rate from $S \to S'$ and I_{sd}.

At this point in MW's description, they considered the short screening length limit when $\lambda \to 0$. This limit ensures that hysteresis in the $I_{sd} - V_{sd}$ characteristic is minimal.

MW then solved for V_T numerically

$$\lim_{N\to\infty} V_T(N)C_g/Ne = \alpha(C/C_g) \tag{2.16}$$

where $\alpha(C/C_g)$ is a dimensionless scaling function. Figure 2.11 shows numerical solutions of Equation 2.16 for a 1D array.

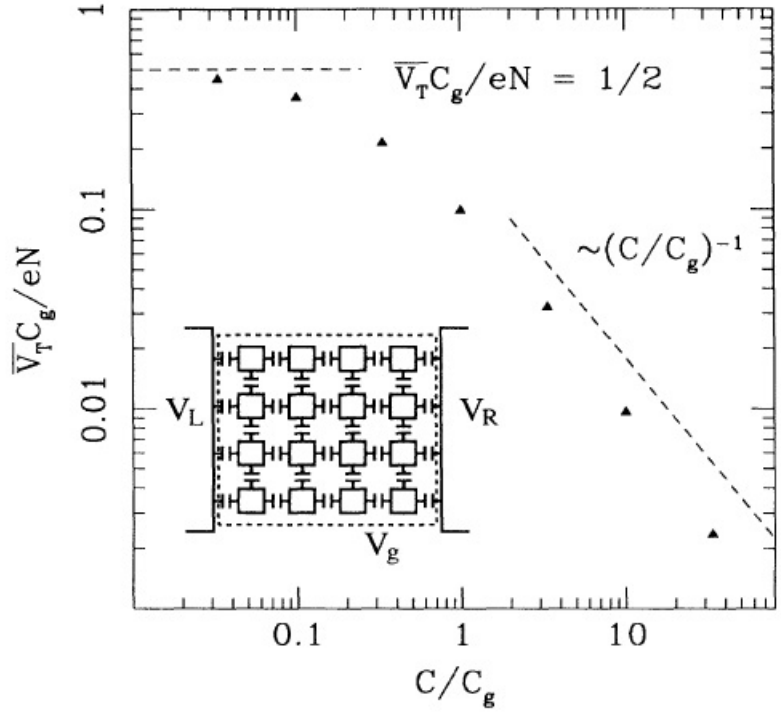

Figure 2.11: Numerical results for $\alpha(C/C_g)$ for a 1D array. Inset: Schematic of a 2D array. [7]

In the limit of $C/C_g \to 0$ in a 1D array,

$$V_T = \frac{Ne}{2C_g} \tag{2.17}$$

while as $C/C_g \to \infty$

$$V_T = \frac{Ne}{C} \tag{2.18}$$

For a 2D array, the numerical prefactor in Equation 2.17 changes from 1/2 to 0.338. Equation 2.18 remains valid for a 2D array. Now that we have both functional forms for the $I_{sd} - V_{sd}$ characteristic and V_T, we examine what the conduction mechanism through a 1D array looks like schematically. For simplicity, we consider a 1D array ($N = 9$) as represented schematically in Figure 2.12.

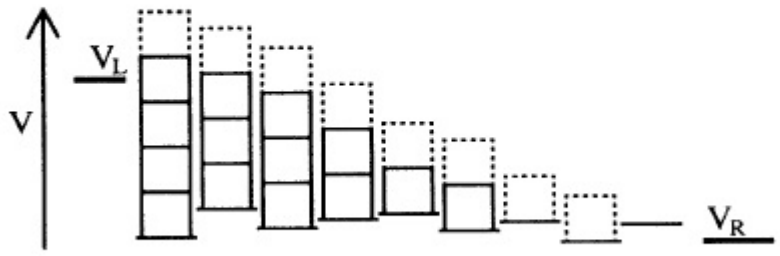

Figure 2.12: Energy landscape in a 1D array.[7]

When an electron is added to a specific QD, the QD's potential energy increases by e/C_g and is represented by a solid black square at a given site. Unoccupied states are represented by dashed squares. Each QD is offset by a random static potential energy from zero (V_R) due to q_i. Again, this is the result of quenched disorder used in the model. As one increases V_L relative to V_R, denoted by the arrow, charges tunnel onto the array. In order to tunnel from site $i \rightarrow j$, the voltage on site i must satisfy the following condition

$$V_i > V_j + e/C_g \tag{2.19}$$

However, if

$$V_i \leq V_j + e/C_g \tag{2.20}$$

an electron may not tunnel from site $i \rightarrow j$. The initial step in Figure 2.12, the

"foot", of this charge staircase defines a charge interface. In Figure 2.12, this occurs at the 6th dot in from the left. As seen in Figure 2.12, as V_L increases to $5e/C_g$, the interface moves two more units to the right. When $V_L = 6e/C_g$, the interface reaches the right lead and charges traverse the array. Charges "tumble" down the charge staircase. For a 1D array, following Fermi's Golden Rule, $I_{sd} \approx (e/2RC_g)(V_{sd}/V_T - 1)$ when V_{sd} is both close to and far away from V_T.

In the case of a 2D array, MW compared the CB condition of Equation 2.19 to that of models used to describe interfacial growth, notably the Kardar-Parisi-Zhang (KPZ) equation, Equation 2.21. The analog of Figure 2.12 for a 2D array is shown in Figure 2.13.

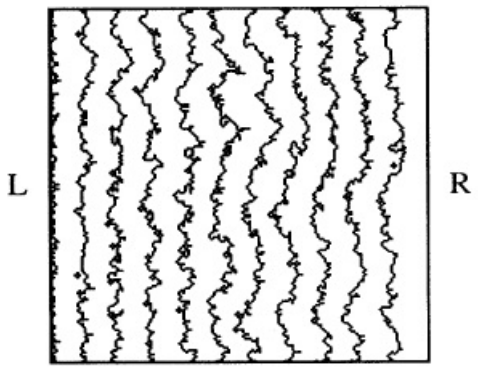

Figure 2.13: Bird's eye view of simulated 1D charge contours propagating through a 160×160 2D array.[7] The L and R denote the locations of the left and right electrodes contacting the 2D array. Each contour represents the distance charge propagates through the array below V_T.

In Figure 2.13, each wavefront represents a 1D charge interface moving an additional unit to the right. Like the 1D array, once the interface reaches the right lead charges can tunnel from the left to right lead. Then MW argued that the $d-1$ dimensional KPZ equation with stochastic noise is appropriate to describe the growing charge interface in d-dimensional QD arrays. Let us delve into the basics of the KPZ equation. What is key in the following discussion is to examine the scaling properties with the width of the interface. From this, MW argued that the 2D scaling exponent in Equation 2.14 should be 5/3.

KPZ developed their equation to describe growing interfaces.[8] These could be smoke fronts, colloidal aggregates, fire flame fronts or tumor growth. The KPZ equation for a 1D interface reads

$$\frac{\partial h(x,t)}{\partial t} = \nu \nabla^2 h(x,t) + \frac{\lambda}{2}(\nabla h(x,t))^2 + \eta(x,t) \tag{2.21}$$

Here $h(x,t)$ is the height profile of the interface which is a single-valued function of position, x ($h(x,t)$ doesn't overhang). The first term on the right hand side (RHS) of Equation 2.21 describes the relaxational properties of the interface with the prefactor (ν) being the surface tension. The next term on the RHS is a phenomenological term which is the lowest-nonlinear term needed for interface growth. $\eta(x,t)$ is a Gaussian noise term which obeys the following relations $\langle \eta(x,t) \rangle = 0$ and

$$\langle \eta(x,t)\eta(x',t') \rangle = 2D\delta(x-x')\delta(t-t') \tag{2.22}$$

where D is the diffusion constant.

KPZ justifies the nonlinear term's existence with the following argument. They consider the growth of an Eden cluster. An Eden cluster is an aggregate of particles, named after its first investigator Murray Eden.[65] For an Eden cluster, particles are added to a growing interface at the edge of the cluster. In addition, Eden cluster growth occurs only normal to the interface. When the interface grows a distance δh in a time interval δt due to the addition of a particle,

$$(\delta h)^2 = ((v\delta t)^2 + (v\delta t \nabla h)^2)^{1/2} \tag{2.23}$$

where $v = -\partial h/\partial x$ and can be seen in the upper inset of Figure 2.14. Furthermore, performing a Taylor series expansion and keeping only two leading terms we have

$$\frac{\delta h}{\delta t} = v(1 + (\nabla h)^2)^{1/2} \simeq v + \frac{v}{2}(\nabla h)^2 \tag{2.24}$$

KPZ then obtain Equation 2.21 by transforming into the comoving frame of the interface. In addition, KPZ solve the deterministic version ($\eta(x,t) = 0$) of Equation 2.21 and plot its solutions as seen in Figure 2.14.

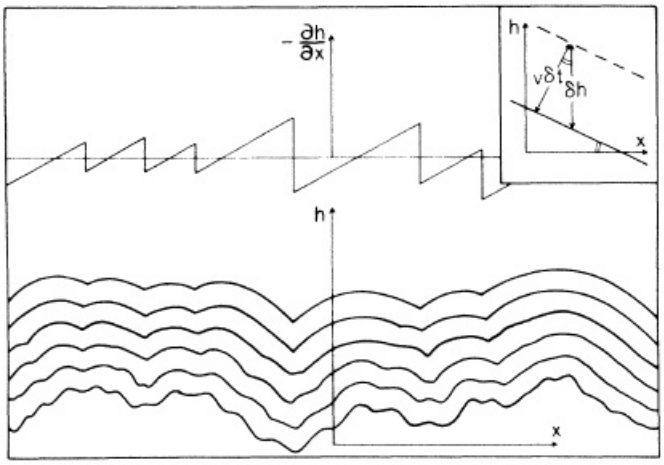

Figure 2.14: Bottom: $h(x,t)$ contours at different time increments. Top: $-\partial h(x)/\partial x$.[8]

Solving the full KPZ equation with stochastic noise ($\eta(x,t) \neq 0$) is highly non-trivial and requires intimate knowledge of dynamic renormalization group theory. The take-away is that by analyzing the asymptotics of Equation 2.21, the width of the interface (w) in a strip geometry of length ($x = L$) scales as

$$w(L,t) = L^{\chi} w_0(t/L^z) \tag{2.25}$$

where χ is the roughness exponent and z is the dynamical critical exponent. For an interface of dimension d=1, $\chi = 1/2$ and $z = 3/2$, and these values are found by solving the RG flow equations (Equation 5a in KPZ's original paper). As KPZ note, by considering a simple example of a spherical cluster whose radius ($R \sim t$),

$$w(R,t) \sim R^{\chi} w_0(t/R^z) \sim t^{\chi/z} \sim t^{1/3} \tag{2.26}$$

In the case of QD arrays, the dynamics of the problem (t in the KPZ equation) are dictated by V_L. Thus from Equation 2.26, $w_{interface} \sim V_L^{1/3}$ for a 1D charge interface in a 2D array. With this in mind, we examine the MW argument for the scaling forms of the $I_{sd} - V_{sd}$ characteristic. Unlike in 1D arrays, current in 2D arrays branches and recombines as seen in the dark current path in Figure 2.16.

Then MW argue that from work on the KPZ equation and from similiar work on roughness and pinning of domain walls in Ising systems, the length scale for transverse

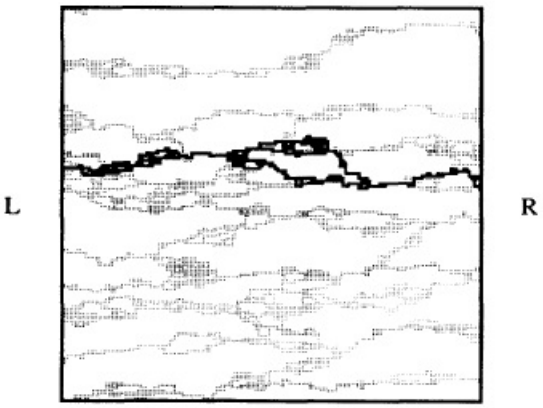

Figure 2.15: Percolating current paths through a 160 × 160 2D array.[7] The L and R denote the locations of the left and right electrodes contacting the 2D array. The dark line is a single current path right above V_T while the lighter lines are multiple channels $3e/C_g$ above V_T.

path fluctuations is

$$\xi_\perp \sim (\xi_\parallel)^{1/z} \tag{2.27}$$

where $\xi_\parallel$ is the distance between branch points. Furthermore, if $\xi_\parallel = eN/(V_L - V_T)C_G$ then

$$\xi_\perp \sim (V_L - V_T)^{-2/3} \tag{2.28}$$

Finally, provided that each current path is 1D between branch points, the total current for a 2D array will be

$$I_{sd} = (e)/(2RC_g)(V_{sd}/V_T - 1)\xi_\perp \sim (V_{sd}/V_T - 1)^{5/3} \tag{2.29}$$

which is Equation 2.14. In a final note, MW calculated numerically the scaling exponents for a 1D and 2D array as will be seen in Figure 3.3.

For 1D arrays, the scaling exponent values are $\zeta_{1D} = 1$ while for 2D arrays $\zeta_{2D} = 2.0 \pm 0.2$. A caveat regarding the numerical work is, as MW state, numerical calculations

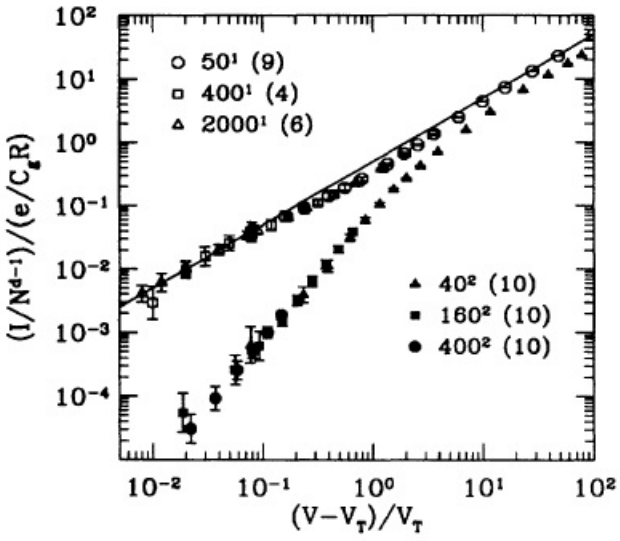

Figure 2.16: Numerical results for the scaling analysis.[7] The unfilled (filled) circles, squares, and triangles denote the size of the 1D (2D) array. The numbers in the parenthesis for each array denote the number of disorder realizations used in the numerical simulation.

did not converge in the limit of low V_{sd}. However, MW argue that 2D arrays of sizes upwards of 400×400 would exhibit the "true" scaling exponent.

2.3 Quantum Wires and the Landauer Formulism

In this final subsection, I will discuss transport in an idealized 1D wire. In a quantum wire, conduction electrons are confined by the boundary conditions in 2 dimensions, say (x, y). However, electrons move freely, as plane waves, along the z direction. If there is a barrier in the channel, electrons are both transmitted and reflected at this barrier. In 1957, Rolf Landauer at IBM developed the appropriate formulism to deal with this geometry.[66] The main idea is that conductance is transmission through the barrier and channel. I will start with the theory developed by Landauer for a single channel. Then, I will expand on this for multi-channel transport following Imry's chapter on Landauer-Type Formulation in *Introduction to Mesoscopic Physics*.[9]

We consider a system with a 1D channel with a single barrier in it as seen in Figure 2.17. We want to calculate the two terminal conductance of this system at $T = 0$.

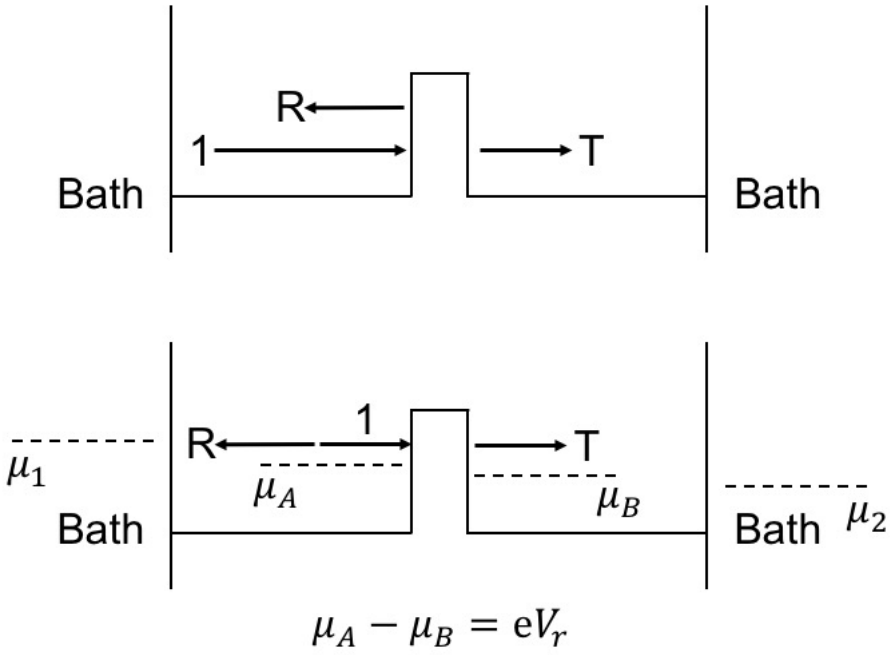

Figure 2.17: 1D elastic scattering center between two charge reserviors. Drawing adapted from Imry.[9]

Two charge reservoirs, at their respective electrochemical potentials $\mu_{1,2}$, feed a current I to the channel and barrier. The barrier is characterized by a transmission coefficient (T) and reflection coefficient (R) with $T + R = 1$. If one considers the density difference across the barrier and then uses the Einstein relation to calculate the barrier conductance G_b,

$$G_b = \frac{eI}{\mu_A - \mu_B} = \frac{e^2}{\pi\hbar}\frac{T}{R} \tag{2.30}$$

which is measured between the electrochemical potentials on either side of the barrier ($\mu_{A,B}$) seen in the bottom part of Figure 2.17. In addition, the conductance of the channel, G_c is

$$G_c = \frac{eI}{\mu_1 - \mu_2} = \frac{e^2}{\pi\hbar}T \tag{2.31}$$

Therefore, the total conductance is the series sum of G_b and G_c which is

$$G_{tot} = \frac{G_b G_c}{G_b + G_c} = \frac{e^2}{\pi\hbar}\frac{T}{2-T} \tag{2.32}$$

What is unique about Equation 2.32 is that if we have a perfectly transmitting barrier ($T = 1$), then $G_{tot} = \frac{e^2}{\pi\hbar}$. The conductance depends only on fundamental constants.

Now what happens when we add multiple conducting channels at a finite temperature? In this situation, we have multiple channels, each channel with a rectangular cross-section A, feeding a current to a generic elastic scatterer S seen in Figure 2.18.[9] One feeds this multi-channel system with a current I, the same as the single channel case.

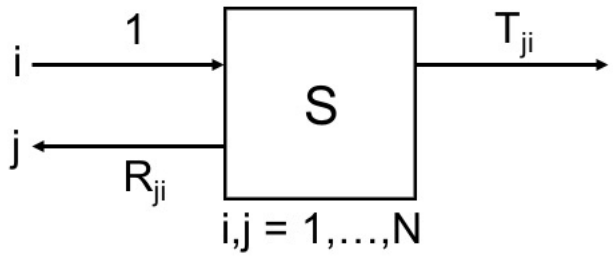

Figure 2.18: A generic elastic scattering center S. Drawing adapted from Imry.[9]

Motion along the transverse directions ((x, y)) is quantized while we have plane wave solutions along the z direction. This leads to electron energies

$$E_F = E_i + \frac{\hbar^2 k_i^2}{2m}, i = 1, ..., N_\perp \tag{2.33}$$

where E_F is the Fermi energy, E_i are the transverse quantized energies, m is the free electron mass, and $N_\perp = Ak_F/2\pi$ is the total number of transverse modes. k_i is the longitudinal wave vector associated with the i^{th} mode, and k_F is the Fermi wavevector.

Our literal black box elastic scatterer operates in the following way. For simplicity, we will also assume that the $T(E = E_F)$ and $R(E = E_F)$ are constant. An incoming wave of amplitude 1 comes in from the left hand side (LHS), i.e. from reservior 1, in the i^{th} channel. The wave is either reflected to channel j with an amplitude r_{ij} or transmitted to the j^{th} channel on the RHS with t_{ij}. The probabilities of these two events occuring are $R_{ij} = |r_{ij}|^2$ or $T_{ij} = |t_{ij}|^2$.

$G(T)$ of multi-channel device, as measured between the charge reserviors $1, 2$, is

$$G = \frac{eI}{\mu_1 - \mu_2} = \frac{e^2}{\pi\hbar} \int dE(-\partial f/\partial E) \sum_i T_i(E) \tag{2.34}$$

where f is the Fermi-Dirac distribution of the source. In the $T \to 0$ limit, Equation 2.34 reduces to

$$G = \frac{e^2}{\pi\hbar} \sum_{ij} T_{ij} \tag{2.35}$$

Equation 2.35 is convenient in the sense that it parallels the single channel case and only depends on the sum of the transmission coefficients. van Wees *et al.* observed clear conductance quantization in a ballistic point contact structure.[10] This device is seen in the inset in Figure 2.19. In their experiment, they used a metal top gate (shaded region in Figure 2.19) to pinch off a narrow, flared constriction of $w = 250nm$ and $L = 1\mu m$ formed between 2 charge reserviors formed in a GaAs/Al_xGa_{1-x}As 2DEG. They measured the two terminal resistance and conductance as a function of V_g through the constriction as seen in Figure 2.19 and Figure 2.20.

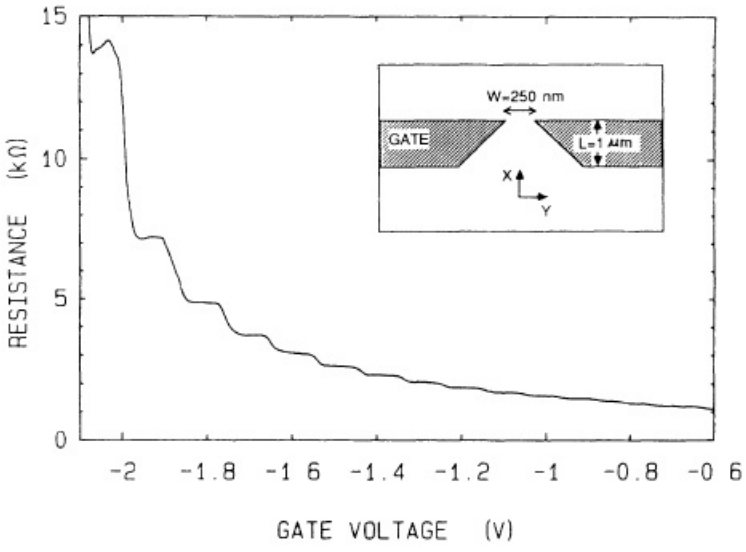

Figure 2.19: $R(V_g)$ at $T = 600mK$. The inset in the upper right hand corner is the device geometry.[10]

$G(V_g)$ in Figure 2.20 includes the subtraction of the contact resistance to the 2DEG. What is striking in Figure 2.20 are the flat plateaus in $G(V_g)$. These plateaus correspond

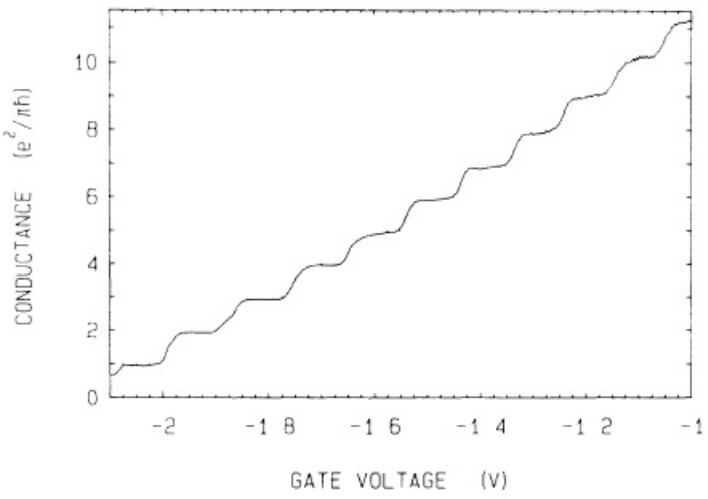

Figure 2.20: $G(V_g)$ at $T = 600mK$.[10]

to the conductance of a single perfectly transmitting channel ($T = 1$) between the reserviors as seen in Equation 2.31. Right below $V_g = -2V$, only a single channel is populated. As V_g increases, an additional conduction channel is added between the reserviors. The reason why these channels are perfectly transmitting is because they are within the ballistic limit with the elastic mean free path, $l = 8.5\mu m > w, L$.

Chapter 3

Superconductivity in a Nutshell

In this chapter, I will briefly review some theoretical and experimental aspects of superconductivity. This includes a discussion of the basic experimental facts of bulk superconductivity, of the London phenomenological theory and a sketch of the microscopic Bardeen-Cooper-Schrieffer theory of superconductivity. Then I will present the phenomenological theory of superconductivity as developed by Vitaly Ginzburg and Lev Landau. I will finish the chapter with brief treatments of the Josephson effect, and the theory phase slip events and dissipation in non-equilibrium quasi-1 dimensional superconductors.

3.1 Basics of Bulk Superconductivity

There are two hallmarks of bulk superconductivity, the first being a zero resistance state and the second being the Meissner effect. The first property was discovered by Kamerlingh Onnes in 1911.[12] Upon cooling down Mercury below $T = 4.2K$ the resistance fell to zero. The original figure by Onnes is seen below in Figure 3.1. The second property is the Meissner effect which was discovered by Meissner and Ochsenfeld in 1933.[13] The Meissner effect is the expulsion of an external magnetic field by a superconductor as seen in Figure 3.2. A superconductor is nearly a perfect diamagnet.

However, clean metals in the superconducting state can only expel magnetic fields up to a critical value, the thermodynamic critical field $H_c(T)$. It should be noted that this is strictly true for Type I superconductors. For Type II superconductors,

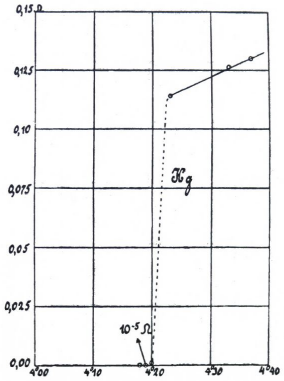

Figure 3.1: $R(T)$ showing the superconducting transition of Mercury.[12]

magnetic fields may penetrate the bulk superconductor at fields lower than $H_c(T)$.[11] The thermodynamic critical field is related to the condensation energy per unit volume $(H_c^2/(8\pi))$ of the superconducting state by the following relation

$$\frac{H_c^2(T)}{8\pi} = f_s(T) - f_n(T) \tag{3.1}$$

Here $f_{s(n)}(T)$ are the free energy densities of the normal and superconducting states respectively. The external magnetic field does not instantaneously go to zero from the exterior of a superconductor to the interior. Rather, $B \to 0$ in the superconductor with a characteristic decay length known as the London penetration depth (λ_L). Thus, the diamagnetism is only nearly perfect.

To understand where λ_L comes from, we will review the London equations which were the first attempt to describe the electrodynamic behavior of the superconducting state. Two years after the discovery of the Meissner effect, Fritz and Heinz London proposed the following phenomenological electrodynamic equations to describe the superconducting state. The first London equation is

$$\mathbf{E} = \frac{\partial}{\partial t}(\Lambda \mathbf{J}_s) \tag{3.2}$$

Here $\mathbf{E}$ is the microscopic electric field in the superconductor, Λ is a phenomenological parameter defined in Equation 3.6, and $\mathbf{J}_s$ is the supercurrent density. Equation 3.2 describes how a time varying supercurrent generates a microscopic electric field in

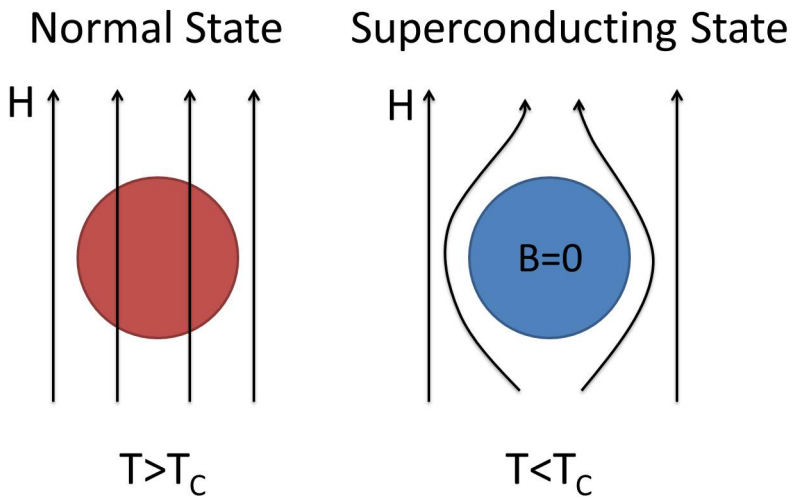

Figure 3.2: A solid metal sphere in the normal state (left) and in the superconducting state (right). For $T < T_c$, the configuration is independent of the order of cooling and application of the magnetic field.

the superconductor. Furthermore, the steady state supercurrent generates a magnetic field. The second London equation is

$$\mathbf{h} = -c\nabla \times (\Lambda \mathbf{J}_s) \tag{3.3}$$

Here $\mathbf{h}$ is the microscopic magnetic field generated by $\mathbf{J}_s$ and c is the speed of light. By taking the curl of Equation 3.3, we obtain

$$\nabla^2 \mathbf{h} = \frac{\mathbf{h}}{\lambda_L^2} \tag{3.4}$$

provided we use Maxwell's equations. If we place a bulk superconductor in an external magnetic field parallel to the surface, $\mathbf{h}$ will obey

$$h(x) = h(x = 0) \exp(-x/\lambda_L) \tag{3.5}$$

where x is measured from the surface of the superconductor inward.

Thus, $\mathbf{h}$ decays with a characteristic length λ_L. Λ and λ_L are related by

$$\Lambda = \frac{4\pi\lambda_L^2}{c^2} = \frac{m}{n_s e^2} \tag{3.6}$$

where m is the free electron mass and n_s is the number density of superconducting electrons.

Further discussion of the phenomenology of the superconducting state will be reserved for the next section on Ginzburg-Landau (GL) theory. This theory provides a powerful phenomenological technique which predicts various macroscopic properties of the superconducting state, like fluxoid quantization and the Josephson effect. However, GL theory does not provide a mechanism for superconductivity. In 1957, Bardeen, Cooper, and Schrieffer (BCS) developed a microscopic theory of superconductivity.[14]

The BCS theory is based on the following explanation of the superconducting state. Upon cooling down a superconductor below its critical temperature, T_c, electrons condense into a special zero center-of-mass moment ground state. Spin up electrons with momentum $+k$ pair with spin down electrons with $-k$ on the opposite side of the Fermi surface forming an energetically favored bound state. This is a consequence of a net attractive interaction mediated by the lattice. This bound state is effectively a composite boson of charge $|q| = 2e$ known as a Cooper pair. A cartoon of a Cooper pair is seen in Figure 3.3.

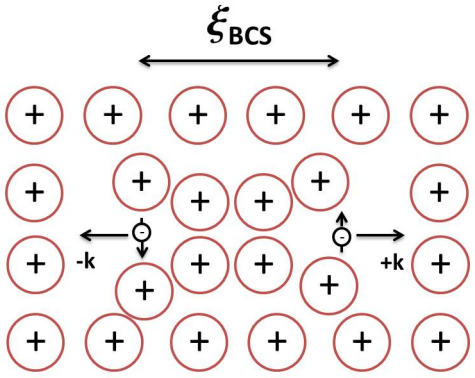

Figure 3.3: An idealized Cooper pair. ξ_{BCS} is the BCS coherence length and is the size of the Cooper pair in real space.

The effective attractive interaction between electrons is mediated by a distortion of the positively charged lattice as shown in Figure 3.3. The characteristic size of a Cooper

pair, the BCS coherence length, is $\xi_{BCS} \simeq \hbar v_F/\pi\Delta(T=0)$ where v_F is the Fermi velocity. $\Delta(T=0)$ is the BCS order parameter at $T=0$ and is equal to $\Delta(T=0) = 1.76 k_B T_c$. Furthermore, at the Fermi surface, an energy gap, $E_g(T=0) = 2\Delta(T=0)$, opens up as seen in Figure 3.4.

An energy of 2Δ separates the Cooper pair condensate from higher energy fermionic excitations, known as quasiparticles (QPs). The QPs are electron-like or hole-like excitations dressed with interactions. E_g is the energy needed to break a Cooper pair into two QPs. $\Delta(T=0)$ is related to the microscopic electronic properties of a material by

$$\Delta(T=0) \approx 2\hbar\omega_c \exp^{-1/N(0)V} \tag{3.7}$$

where ω_c is the Debye frequency, $N(0)$ is the single particle electronic density of states at the Fermi level, and $V = constant$ is the pairing potential energy. A "stronger" superconductor in BCS theory is one with a larger gap.

The temperature dependence of the BCS order parameter, valid for $T \leq T_c$, is given by

$$\Delta(T)/\Delta(T=0) \approx 1.74(1 - T/T_c)^{1/2} \tag{3.8}$$

The mean-field functional form is analogous to the Ginzburg-Landau superconducting order parameter, as seen later in this chapter.

Above and below the gap, the QP dispersion relation, with respect to E_F, is given by

$$E_k = \sqrt{\xi_k^2 + \Delta^2} \tag{3.9}$$

where $\xi_k = \hbar^2 k^2/2m$ is the single particle energy. The dispersion relation is shown in Figure 3.4.

The positive E_{ks} branch is the spectrum for electron-like quasiparticles while the negative E_{ks} branch is for hole-like quasiparticles. This picture is helpful in visualizing charge mode disequilibrium in nanowires, as I will discuss later in this chapter. Finally, the distribution function of QPs in thermal equilibrium is a Fermi-Dirac distribution function.

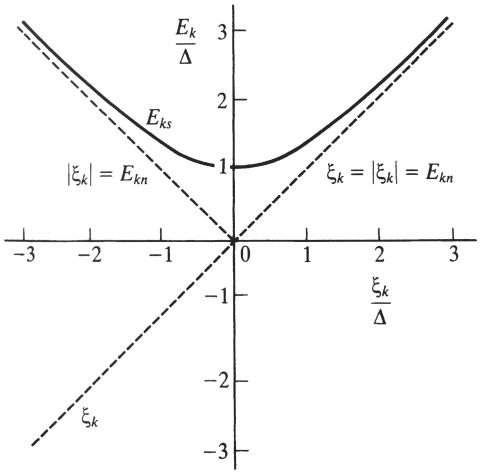

Figure 3.4: Black line: normalized superconducting quasiparticle dispersion relation (E_{ks}/Δ) plotted as a function of single particle energies (ξ_k/Δ) adapted from Tinkham. The dashed lines correspond to the normal state quasiparticle dispersion, $E_{kn} = \xi_k$.[11]

$$f_0(E_k/k_BT) = \frac{1}{e^{E_k/k_BT} + 1} \tag{3.10}$$

BCS theory is elegant because it describes the mechanism for the formation of the superconducting state. Additionally, it predicts the functional form for observable quantities such as the E_g and T_c. But, it is not helpful without significant extension in predicting the transport properties of superconducting devices. With this in mind, what is the easist way to describe the basic transport properties of superconducting nanowires? The answer lies in the phenomenological Ginzburg-Landau theory of superconductivity.

3.2 Ginzburg-Landau Theory of Superconductivity

The Ginzburg-Landau (GL) theory of superconductivity is nothing more than an extension of the GL theory of second order phase transitions to the superconducting state.[11] The carriers, Cooper pairs, are charged bosons which undergo a superfluid transition at T_c. The theory states that the superconducting state can be described by a spatially and temporally dependent two-component complex order parameter.

$$\Phi(r,t) = |\Phi(r,t)| \exp(i\varphi(r,t)) \tag{3.11}$$

$|\Phi(r,t)|$ is the amplitude and $\varphi(r,t)$ is the phase of the complex order parameter. The order parameter is a macroscopic pseudo wave function which describes the superconducting state. It takes on a non-zero average value only below T_c. As shown by Gor'kov, the time independent GL order parameter ($\Phi(r)$) is related to the BCS order parameter ($\Delta(r)$) by $\Phi(r) = \Delta(r)\sqrt{\frac{7\zeta(3)N(0)}{4\pi T_c}}$.[68] Here $\zeta(x)$ is the Riemann Zeta function and $N(0)$ is the single particle electronic density of states at the Fermi level.

By taking the square of the order parameter we obtain the density of Cooper pairs ($n_s(r,t)$)

$$n_s(r,t) = \Phi^*(r,t)\Phi(r,t) \tag{3.12}$$

Now in the next step, we assume that $n_s = n_s(r)$ and is time independent. Following the GL prescription, we assume that the superconducting free energy density ($f_s(T)$) can be expanded in powers of Φ and $\nabla\Phi$ for $T < T_c$ thus

$$f_s = f_n + \alpha|\Phi|^2 + \frac{\beta}{2}|\Phi|^4 + \frac{1}{2m^*}|(-i\hbar\nabla - \frac{e^*}{c}\mathbf{A})\Phi|^2 \tag{3.13}$$

Equation 3.13 also assumes that the order parameter varies slowly over large length scales and $\mathbf{h} = 0$. f_n is the normal state free energy density. α, β are phenomenological parameters. $e^* = 2e$ and $m^* = 2m$, twice the electron charge and mass, and $\mathbf{A}$ is the magnetic vector potential.

To show how the superconducting state becomes energetically favorable below T_c, we will keep the first three terms in the expansion and minimize with respect to $|\Phi|$. In this case,

$$f_s - f_n = \alpha|\Phi|^2 + \frac{\beta}{2}|\Phi|^4 \tag{3.14}$$

Setting $\frac{\partial(f_s - f_n)}{\partial|\Phi|} = 0$, we obtain the equilibrium value of the order parameter in the superconducting state.

$$|\Phi|^2 = |\Phi_\infty|^2 = \frac{-\alpha}{\beta} \tag{3.15}$$

where the subscript (∞) denotes the average value of the order parameter deep inside the superconductor. Figure 3.5 shows Equation 3.14 as a function of the real and imaginary parts of Φ. In this case, $f_s - f_n$ is typically refered to as the "Mexican Hat Potential". Furthermore, we must assume that $\alpha(T) = \alpha_0(\frac{T}{T_c} - 1)$ where $\alpha_0 = constant > 0$ and $\beta = \beta_0 = constant > 0$ below T_c.

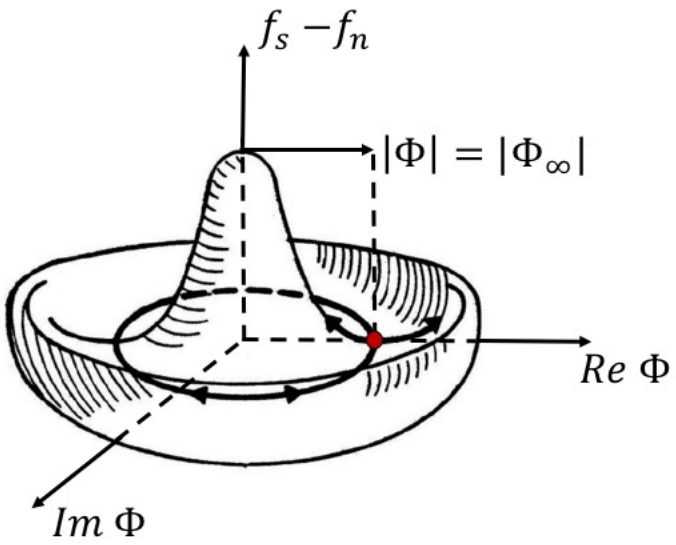

Figure 3.5: $f_s - f_n$ (Equation 3.14) as a function of the real and imaginary parts of Φ adapted from C.M. Varma.[70] The location of the red sphere denotes the minimum of the amplitude of the order parameter (Equation 3.15). Fluctuations in the amplitude and phase of the order parameter are denoted by the arrows radially away from the $f_s - f_n$ axis and around $f_s - f_n$ axis respectively. Fluctuations can be visualized by the mechanical analogy of rolling the red sphere along the arrowed contours.

If we substitute Equation 3.11 back into $f_s - f_n$ from Equation 3.10 and we obtain

$$f_s - f_n = \frac{-\alpha^2}{2\beta} = \frac{-H_c^2(T)}{8\pi} \tag{3.16}$$

which relates the theory's phenomenological parameters to $H_c(T)$. In addition, we find an expression for the temperature dependence of the order parameter by plugging $\alpha(T)$ into Equation 3.15.

$$|\Phi(T)| \sim (1 - \frac{T}{T_c})^{1/2} \tag{3.17}$$

As expected, Equation 3.17 has a mean-field exponent of 1/2 just like the BCS order parameter in Equation 3.8. To derive the GL equations equation which describe $\Phi(r)$ and $\mathbf{J}_s$, we must do a variational minimization of Equation 3.9. To obtain the two GL equations, we compute $\delta F_s = 0$ by varying separately both $\delta\Phi(r)$ and $\delta\mathbf{A}$.

This means we compute $\delta F_s = \delta \int f_s d^3\mathbf{r} = \int \frac{\delta f_s}{\delta\Phi(r)} d^3\mathbf{r} = 0$ to obtain the first GL equation (Equation 3.18) and $\delta F_s = \int \frac{\delta f_s}{\delta\mathbf{A}} d^3\mathbf{r} = 0$ to obtain the second GL equation (Equation 3.19).

Therefore, we obtain

$$\alpha\Phi + \beta|\Phi|^2\Phi + \frac{1}{2m^*}(\frac{\hbar}{i}\nabla - \frac{e^*}{c}\mathbf{A})^2\Phi = 0 \tag{3.18}$$

$$\mathbf{J}_s = \frac{e^*}{m^*}|\Phi|^2(\hbar\nabla\varphi - \frac{e^*}{c}\mathbf{A}) = 2e|\Phi|^2\mathbf{v}_s \tag{3.19}$$

Equation 3.18 is a nonlinear Schrodinger equation with eigenvalue $-\alpha$. This equation describes spatial variations in $\Phi(r)$. The β term is in some sense a self-repulsion term for Φ. It "forces" Φ to spread out in space. Equation 3.19 says that the supercurrent is driven by spatial variations in the phase of the order parameter and the presence of $\mathbf{A}$.

From Equation 3.18, we derive the natural length scale for spatial variations in Φ away from Φ_∞, the GL coherence length. For simplicity, we consider the case when $\mathbf{A} = 0$. We also normalize Equation 3.18 by $|\Phi_\infty|$ and define $\phi \equiv \frac{|\Phi|}{|\Phi_\infty|}$. In addition, we will deal with the simple case of a 1D version of Equation 3.18. In 1D and normalized by $|\Phi_\infty|$, we have

$$\frac{\hbar^2}{2m^*|\alpha(T)|}\frac{d^2\phi}{dx^2} + \phi - \phi^3 = 0 \tag{3.20}$$

By reading off the coefficient in front of the gradient term of Equation 3.20, we have

$$\xi_{GL}^2(T) = \frac{\hbar^2}{2m^*|\alpha(T)|} = \frac{\hbar^2}{2m^*\alpha_0(1 - T/T_c)} \tag{3.21}$$

This is the GL coherence length. It is the natural length scale for variations in the amplitude and phase of the order parameter as in Equation 3.11. However, in real

materials, such as elemental superconductors like aluminum, this result must reflect the presence of static scattering centers. This is the dirty limit GL coherence length. Following from a microscopic analysis of the GL equations as done by Gor'kov, the dirty limit GL coherence length is given by[68, 69]

$$\xi_{GL,dirty}(T) = 0.855\frac{(\xi_{BCS}l)^{1/2}}{(1-T/T_c)^{1/2}} \tag{3.22}$$

For Aluminum, $\xi_{BCS} = 1.6\mu m$. l is the elastic mean free path and can be estimated from measurements of the normal state resistivity. l is typically $\approx 100\mathring{A}$ for elemental metals like Al.

From Equation 3.22, we can define the effective dimension of the superconductor. For example, if we have a nanowire whose transverse dimensions (height and width) are less than $\xi_{GL,dirty}(T)$, then the nanowire behaves as a quasi-1D superconductor. In other words, $|\Phi|$ is constant across the wire's cross section. However, these nanowires are not electronically 1D since the linear dimensions of the cross section are much larger than the Fermi wavelength, $\lambda_F \approx 1\mathring{A}$.

Quasi-1D superconductors are interesting because they exhibit a unique dissipation mechanism when $T < T_c$. This mechanism, which involves so-called phase slip events, produces a finite voltage in the nanowire and thus a resistance below T_c. This process will be the focus of the next section. But prior to that, we will finish out this section by discussing the second GL equation, Equation 3.19.

In the case of a quasi-1D superconductor, we can compute the critical current density (J_c) via Equation 3.19. As stated in the previous paragraph, $|\Phi|$ is constant across the cross section and thus the order parameter takes the form $\Phi(x) = |\Phi|\exp(i\varphi(x))$. The idea will be to minimize Equation 3.13 to find an expression for $|\Phi|^2$ and then to plug this expression into Equation 3.19.

For a given supercurrent velocity, v_s, we compute $\frac{\partial(f_s)}{\partial|\Phi|} = 0$ and obtain

$$|\Phi|^2 = |\Phi_\infty|^2(1 - (\frac{m^* v_s^2}{2|\alpha(T)|})) \tag{3.23}$$

Plugging Equation 3.23 into Equation 3.19 we obtain an expression for J_s.

$$J_s = 2e|\Phi_\infty|^2(1 - (\frac{m^* v_s^2}{2|\alpha(T)|}))v_s \tag{3.24}$$

J_c occurs when J_s has a maximum in v_s or when $dJ_s/dv_s = 0$.

The functional form of J_c is thus

$$J_c(T) = 2e|\Phi_\infty|^2 \frac{2}{3}(\frac{2|\alpha|}{3m^*})^{1/2} \sim (1 - T/T_c)^{3/2} \tag{3.25}$$

Now that we know J_c, the next question to ask is what mechanism drives dissipation in a quasi-1D superconductor. Phase slip events create a finite voltage below T_c. However, prior to treating this phenomenon, I will discuss a key concept necessary to understand a phase slip event. This is the Josephson effect.

3.3 The Josephson Effect

It is necessary to briefly highlight the contributions of B.D. Josephson in order to understand dissipation in quasi-1D superconductors. Josephson was interested in the process of Cooper pairs tunneling from one superconductor to another through a thin insulating barrier (a Josephson junction). He made two seminal predictions regarding this process.[11, 73, 74]

The first prediction was that a dc supercurrent (I_s) can flow through the insulating barrier provided there is a difference in the GL phase ($\Delta\varphi$) across the junction.

$$I_s = I_c \sin(\Delta\varphi) \tag{3.26}$$

I_s reaches a maximum of I_c, the critical current of the junction. The second prediction was that a time varying GL phase difference across the junction produces a voltage across the junction and visa versa.

$$d(\Delta\varphi)/dt = 2eV/\hbar \tag{3.27}$$

If a Josephson junction is biased with a dc voltage, then Equations 3.26 and 3.27 combined predict an ac supercurent, with angular frequency ($\omega = 2eV/\hbar$), flowing across the junction. As noted in Tinkham, both Josephson relations are quite general and can be extended to any case where there are two superconductors coupled through a "weak link".[11] The "weak link" may be a normal metal region, narrow constriction, or insulating barrier. Equation 3.27 will be used in the following discussion of phase slip processes.

3.4 Phase Slips

Phase slip events occur when the amplitude of the order parameter is driven to zero at a point along a quasi-1D superconductor. Phase coherence is momentarily broken along the quasi-1D superconductor. We focus on a graphic representation of a phase slip event in Figure 3.6 for throughout this discussion.

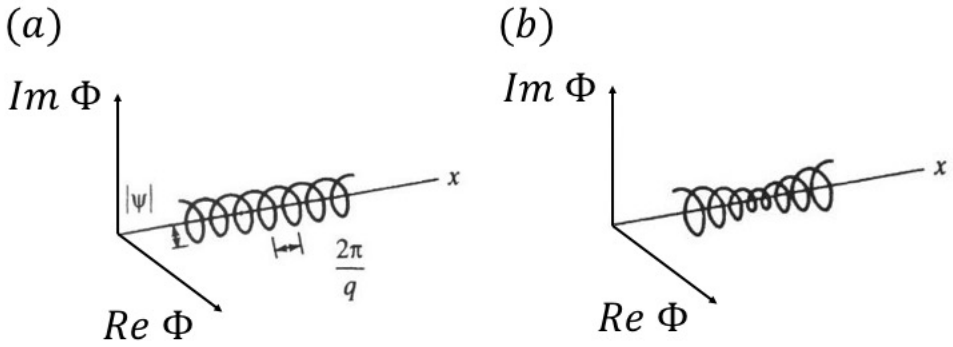

Figure 3.6: A phase slip process.[11] (a) An Argand diagram of the uniform order parameter solution to the 1D GL equations (Equation 3.26). (b) Non-uniform order parameter solution just prior to a phase slip event.

Figure 3.6 depicts solutions, in polar form, of the GL equations for a quasi-1D superconductor of length L, width w, and height h as discussed in the previous section. We first focus on Figure 3.6a which shows the equilibrium solutions of the GL equations for such a geometry. In a quasi-1D superconductor, the amplitude of the order parameter is constant across the wire's cross section in the (y, z) plane. In addition, the amplitude of the order parameter does not change as function of x along the wire's axial direction. However, the phase will, as seen in Figure 3.6a. The solutions of the GL equations are plane wave solutions and have the form

$$\Phi_q(x) = |\Phi(x)| \exp(iqx) = \sqrt{\alpha - q^2/\beta} \exp(iqx) \tag{3.28}$$

Here the wavenumber, q, is related to the total phase difference along the length of the wire ($\Delta\varphi$) by $\Delta\varphi = qL$. α and β are the phenomenological parameters of the GL

free energy. In polar form, Figure 3.6a, the solution is a helix along the x axis with a helix spacing of $2\pi/q$.

We now examine the non-equilibrium solutions of the GL equations as seen in Figure 3.6(b). We now apply a voltage across the ends of the wire. $\Delta\varphi$ is initially $\Delta\varphi = qL$. However, the presence of a voltage between the ends of the wire increases $\Delta\varphi$ as a function of time. We can see this from the second Josephson equation whereby $d(\Delta\varphi)/dt = 2eV/\hbar$.

Visually, we hold the helix in Figure 3.6a steady on the left and add additional loops to the helix from the right. As the helix tightens, J_s increases. Eventually, $J_s = J_c$ and the wire is driven completely normal below T_c. However, to prevent this, the order parameter undergoes a phase slip event. This process drives the amplitude of the order parameter to zero and eliminates a loop in the phase of the order parameter as an additional loop is added from the right. A phase slip will locally drive a portion of the wire the size of ξ_{GL} resistive and dissipate energy as heat.

Although the idea of a phase slip is due to William A. Little, the first theories developed to describe the resistive properties of phase slips are those of Langer-Ambegaokar and McCumber-Halperin (LAMH).[15, 16] The goal of LAMH was to develop a functional form of the resistance as a function of temperature ($R_{TAPS}(T)$) of a superconducting wire due to thermally activated phase slips (TAPS).

We begin by reviewing the basics of LAMH's theory, following Tinkham. Again, for non-uniform solutions of the GL equations, $|\Phi|$ is no longer assumed to be constant. We assume that $J_s(x)$ is constant along the length of the wire and ignore the normal current.

$$J_s(x) \sim |\Phi(x)|^2 v_s(x) \sim |\Phi(x)|^2 \frac{d\varphi}{dx} \sim I = constant \tag{3.29}$$

Now, we drive $|\Phi(x = x_0)| \to 0$ at some point x_0 along the wire. Since $J_s(x)$ is assumed to be constant then $d\varphi/dx$ becomes large. Therefore, $\Delta\varphi$ changes rapidly by $\pm 2\pi$. LAMH then said that to go from a configuration when the order parameter has n loops in the phase to $n \pm 1$ loop configuration, the order parameter must overcome, by thermal activation, a free energy barrier (ΔF_0). ΔF_0 is a saddle point in free energy space. In other words, $\Phi_q(x) \to \Phi_{q \pm 2\pi/L}(x)$ or the winding number of the order parameter changes when the phase jumps over the barrier.

Qualitative insight to this process can be seen by viewing the phase slip region as a Josephson junction.[17] The phase slip event is mapped to a mechanical analogy of the motion of a particle (red sphere) in a tilted-washboard potential as seen in Figure. 3.7.

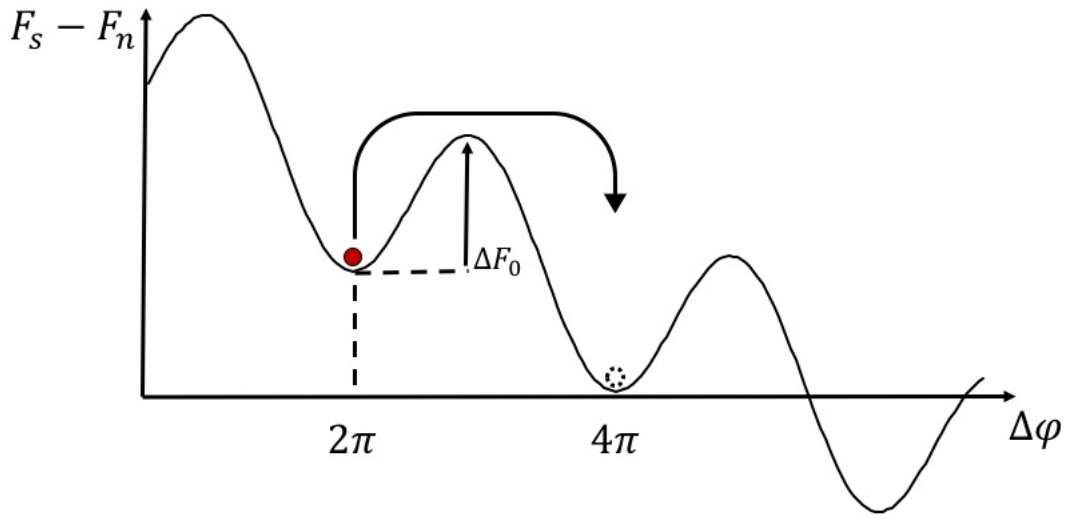

Figure 3.7: Tilted washboard model for a thermally activated phase slip event of $\Delta\varphi = +2\pi$. The particle (red sphere) undergoes a thermally activated jump over the energy barrier (ΔF_0) to a new local energy minimum (dashed sphere).

Given the constraint of Equation 3.29, ΔF_0 between the two solutions with different winding numbers is

$$\Delta F_0 = \frac{8\sqrt{2}}{3}\frac{H_c^2}{8\pi}A\xi \tag{3.30}$$

which represents the condensation energy of a portion of the wire (of length $\sim \xi$) driven normal. LAMH then included the presence of a current source in their calculation. The current source will select phase slip events of $\Delta\varphi = -2\pi$ to outnumber phase slips of $\Delta\varphi = 2\pi$ by a rate $2eV/h$. The work done by the current source ($\int IVdt$) is equal to the free energy difference between phase slips of $+2\pi$ and -2π. Thus,

$$\delta F = \delta(F_{\Delta\varphi=+2\pi} - F_{\Delta\varphi=-2\pi}) = \frac{h}{2e}I \tag{3.31}$$

The energy difference is related to the voltage developed in the nanowire by the second Josephson relation by

$$d(\Delta\varphi)/dt = 2eV/\hbar = \Omega(\exp(-\Delta F_0 - \delta F/2) - \exp(-\Delta F_0 + \delta F/2)) \tag{3.32}$$

where Ω is the attempt frequency of jumping out of the potential minimum.

Rearranging Equation 3.32 and using a trigometric identify, we find that the voltage developed in the nanowire during a TAPS is

$$V = \frac{\hbar\Omega}{e}\exp(-\Delta F_0/k_BT)sinh(\frac{hI}{4ek_BT}) \tag{3.33}$$

In the low current limit, $\sinh x \approx x$. Therefore, we can simplify Equation 3.33 and use Ohm's law to compute the resistance below T_c.

$$R_{TAPS}(T) = \frac{h}{4e^2}\frac{\hbar\Omega}{k_BT}\exp(-\Delta F_0/k_BT) \tag{3.34}$$

Thus we see resistance below T_c is a thermally activated process over ΔF_0. In addition, natural resistance scale for TAPS is $\frac{h}{4e^2}$ or the resistance quantum of a Cooper pair. To get the Ω, one must resort to time dependent GL theory. The functional form of $\Omega(T)$ is

$$\Omega(T) = \frac{L}{\xi}(\frac{\Delta F_0}{k_BT})^{1/2}\frac{1}{\tau_{GL}} \tag{3.35}$$

Here $\tau_{GL} = \frac{\hbar\pi}{8k_B(T_c-T)}$ is the GL relaxation time and is the dominate time scale. The ratio $\frac{L}{\xi}$ expresses the number of locations in the wire that a phase slip event can occur. The $(\frac{\Delta F_0}{k_BT})^{1/2}$ term varies slowly and is order 1 typically.

Thermally activated phase slips provide the most basic mechanism for a finite resistance below T_c. It should be pointed out that the phase can tunnel through the free energy barrier as well, a process known as macroscopic quantum tunneling.[17] Phase slips which occur by this process are known as quantum phase slips.[18]

3.5 Non-Equilibrium Superconductivity in Nanowires

An important aspect of the observed reentrant superconducting behavior is that it is found when QPs are driven out of thermal equilibrium.[35] In our case, they are

generated by phase slips at the center of the wire. The effect is typically observed when the L of the wire is less than $L_{QP} = \sqrt{D\tau_{qp}}$ which is the QP relaxation length (known historically in the literature as the charge imbalance length) and is mediated by Andreev reflection at the nanowire/lead interface.

I will start with discussing charge mode disequilibrium which typically occurs when charge is injected from a normal metal into a superconductor. We will follow the discussion in Tinkham.[11] Then, I will highlight how to compute τ_{QP} from the literature and discuss previously calculated forms for the magnetoresistance ($R(H)$) in out-of-equilibrum quasi-1D nanowires.[32] For the nanowires, $R(H)$ is due to quasiparticle relaxation and conversion to a supercurrent, at a normal-superconducting (N-S) interface. The N-S interface has a size L_{QP}.

First, out-of-equilibrium QPs cause the QP distribution function to be shifted from its equilibrium form by the amount

$$\delta f_k = f_k + f_0(E_k/k_BT) \tag{3.36}$$

Here f_k is the non-equilibrium quasiparticle distribution function and f_0 is the equilibrium quasiparticle distribution function. In charge mode disequilibrium, the net QP charge is given by

$$Q = \sum_k q_k \delta f_k = \sum_k \frac{\xi_k}{E_k} \delta f_k \tag{3.37}$$

The effective charge (q_k) of a QP as a function of energy, ξ_k, is shown in Figure 3.8.

Thus, as one should expect far above (below) the gap, the excitations are electron (hole)-like. Typically, the lifetime of the excitation is given by

$$\tau_{QP} = (4/\pi)(k_BT/\Delta)\tau_{in} \tag{3.38}$$

Here τ_{in} is the inelastic scattering time of an electron, due to the electron-phonon interaction, in the normal state at the Fermi surface. It is the time required for $\delta f_k \to 0$. Very close to T_c, Equation 3.38 is modified by having T replaced with T_c. If the wire is driven almost normal by a current sufficiently near I_c and T_c or by a magnetic field, Equation 3.38 must be modified. In general, τ_{QP} does not have a universal form.

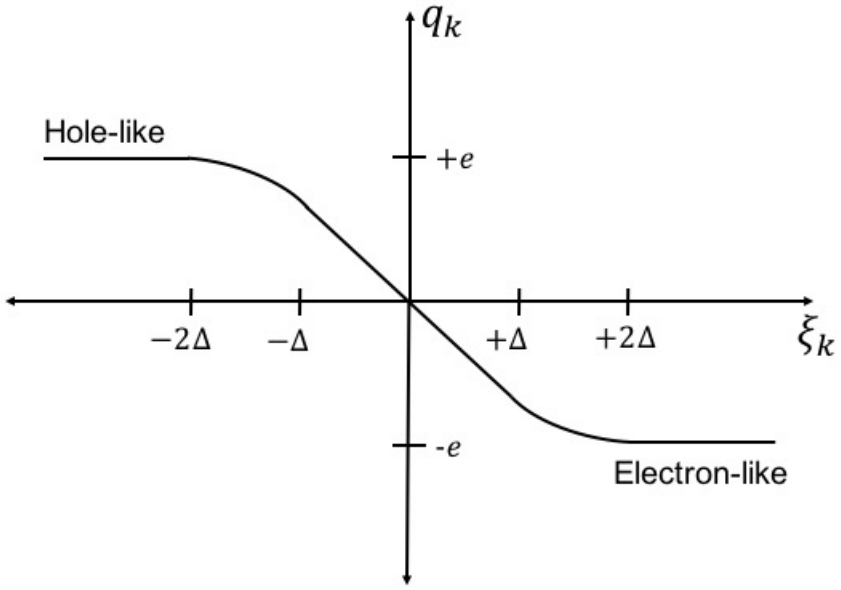

Figure 3.8: QP charge, q_k, as a function of energy, ξ_k. Drawing adapted from P. Santhanam.[19]

In the presence of time-dependent fluctuations in the amplitude and phase of the order parameter or magnetic fields, τ_{QP} becomes the geometric mean of τ_{in} with another dominant time scale. For instance, close to I_c, this other time scale is the Ginzburg-Landau relaxation time ($\tau_{GL} = \pi\hbar/8k_B(T - T_c)$). In a magnetic field, this other time scale is the pair breaking time ($1/\tau_{PB} = (1.76k_BT_c/\hbar)(H/H_{c,||})^2$) where H is the in-plane transverse magnetic field and $H_{c,||}$ is the transverse in-plane critical field.[11, 20, 21]

If the wire is in a condition in which $I \approx I_c$ and $T \approx T_c$, τ_{QP} takes the form[22]

$$\tau_{QP} = \frac{4k_BT_c}{\pi\Delta}(3\tau_{in}\tau_{GL})^{1/2} = 0.55(\frac{\hbar/\tau_{in}}{k_BT_c})^{1/2}\frac{T_c}{T_c - T}\tau_{in} \tag{3.39}$$

On the other hand, in the presence of a magnetic field, but not necessarily close to I_c or T_c[20, 21]

$$\tau_{QP} = \frac{4k_BT}{\pi\Delta}(\tau_{in}\tau_{PB}/2)^{1/2} \tag{3.40}$$

Equation 3.40 remains valid provided $\tau_{PB} < \tau_{in}$. The resistance due to non-equilibrium QPs, R_{QP}, can thus be computed from the form

$$R_{QP} = \frac{2\rho_N}{wd}(D\tau_{QP})^{1/2} \tag{3.41}$$

Here ρ_N is the normal state resistivity, w, d are the width and thickness of the wire, and D is the normal state electronic diffusion constant.[11, 20] The factor of 2 accounts for QP diffusion on either side of a phase slip region. Equations 3.38-3.41 where originally derived in the case of long (tens of μm in length) non-equilbrium superconducting tin/indium microbridges and whiskers, prior to the advent of nanofabrication.[11] In these papers, there was no focus on N-S interfaces or Andreev reflection of QPs. Because of this, we now focus on both topics to finish out this chapter.

We consider an idealized case of a N-S interface. Here we have an N layer sandwiched against an S layer. We inject current from N to S. There is no barrier between the N and S layers.

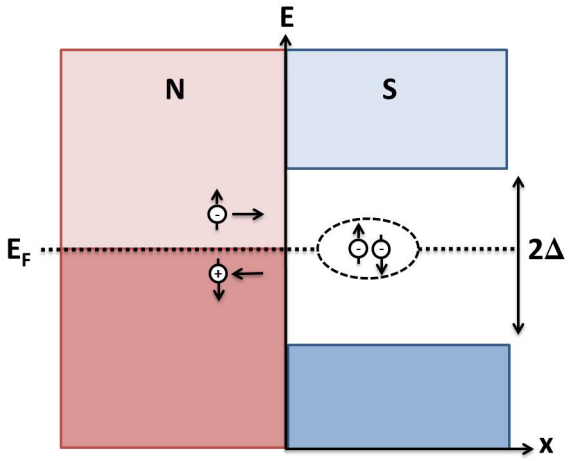

Figure 3.9: An Andreev reflection process. A spin up electron comes in from the normal metal layer on the left and is reflected at the superconducting interface as a spin down hole. In this process, a Cooper pair is transmitted into the superconductor.

Incident electrons ($E > \Delta$) become QPs with charge $Q = -e$ in the superconductor. On the other hand, if an incident electron with $E < \Delta$ reaches the superconductor, it cannot enter the superconductor as a QP because, there are no states available in

the gap. Instead, the incident electron is reflected back as a hole and a charge of $+2e$ is transfered into the superconductor as a Cooper pair. This is Andreev reflection or sometimes refered to as Andreev-St James reflection.[23, 67] Thus, the normal current is converted to a supercurrent at the N-S interface. This can also occur when a QP in a superconductor reaches an interface with another superconductor with a larger gap. For a very detailed explanation of electron transfer processes into a superconductor as a function of tunnel barrier strength (Z), one should look at the theory of Blonder, Tinkham, and Klapwijk.[11, 24]

Finally, we will highlight transport through superconductor-normal-superconductor (S-N-S) Josephson junctions which will be useful interpreting R(H) data later in this thesis. Here, QPs, in the metal layer, undergo Andreev reflections at each of the N-S interfaces. A supercurrent passes between the S layers and through the N layer as a QP current in the metal layer. A schematic of an S-N-S Josephson junction is seen in Figure 3.10.

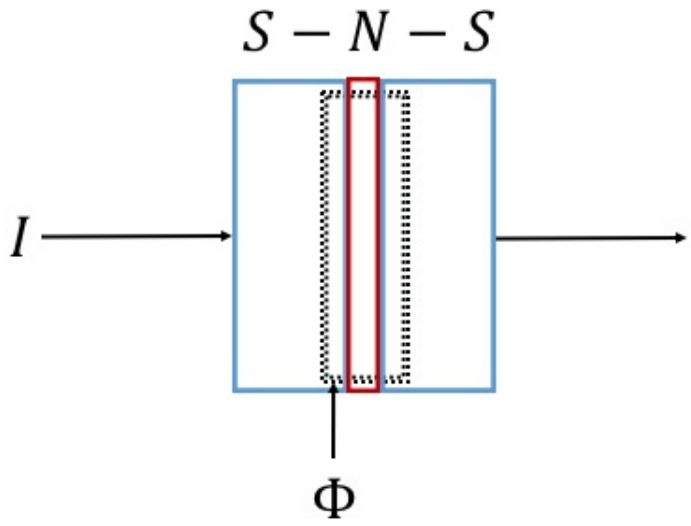

Figure 3.10: A S-N-S junction exposed to an external magnetic flux (dashed square) Φ out-of-the-page and biased with current I.[11]

The QPs live in sub-gap bound states, known as Andreev Bound States (ABS).[25]

The position of these energy levels, relative to the Fermi energy, depends on the gauge invariant phase difference (γ) between the superconducting layers.

$$E_{A\pm}^{(n)} = \frac{\hbar v_F}{2L}(2\pi(n+1/2) \pm \gamma) \tag{3.42}$$

v_F is the Fermi velocity in the N-layer, L is the length of the junction, n is an integer. $E_{A+}^{(n)}$ corresponds to the level populated by a spin up quasi-electron and $E_{A-}^{(n)}$ is populated by a quasi-hole. If there is an external flux threading through the junction $\gamma = \gamma_0 + 2\pi\frac{\Phi}{\Phi_0}$.[11] Therefore, by tuning the Φ one tunes the energy offset of $E_{A\pm}^{(n)}$.

Chapter 4

Background Experiments

In this chapter, I will first discuss experiments involving arrays of quantum dots, in three different model systems, that model transport through the array in terms of Middleton and Wingreen's (MW) theory. After that, I will focus on experiments which first examined TAPS in superconducting nanowires and more recent experiments on magnetic field induced reentrant superconductivity in nanowires. These will provide background for the experimental work done for this thesis.

4.1 Collective Charge Transport in Arrays of Quantum Dots

Following MW's paper, only a handful of groups focused on transport in QD arrays. I will move chronologically through the experimental literature starting with wet etched semiconductor arrays, then discussing a normal metal tunnel junction array. Finally, I will examine a third model system consisting of Au nanocrystal monolayers.

The first experimental paper on collective transport was on a wet etched GaAs QD array by Durouz *et al.*[26] They found not only an $I - V$ characteristic with a scaling exponent of 1.5 but also switching behavior and hystersis in the array. The switching behavior and hystersis parallels the physics of the depinning of charge density waves.[52] The QD array was formed on a 2DEG via a GaAs/$Al_{0.34}Ga_{0.66}$As heterostructure with an electron mobility of $200,000\,cm^2/V-s$ and $n_{2D} = 3.5 \times 10^{11} cm^{-2}$ at $T = 4.2K$. The structure was a 200×200 array with a single QD control device situated above

the array as seen in Figure 4.1b. They did not fabricate a 1D array. The authors used electron beam lithography and wet etching through the 2DEG to define the array. The entire array was situated above a back gate which not only controlled n_{2D} but also the inter dot coupling. An SEM micrograph of the device is seen in Figure 4.1a.

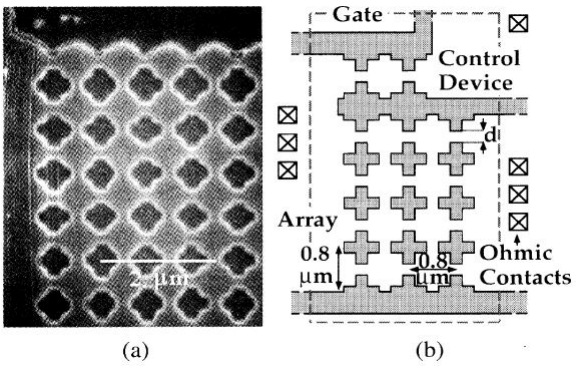

Figure 4.1: SEM micrograph (a) and cartoon of the array device (b).[26]

The dc $I_{ds} - V_{arr}$ characteristics were measured in a dilution refrigerator with a base temperature of 20mK. V_{arr} is the average V_{sd} applied to the array. Figure 4.2 shows the V_g dependence of the $I_{ds} - V_{arr}$ characteristic of the array at $T = 20mK$.

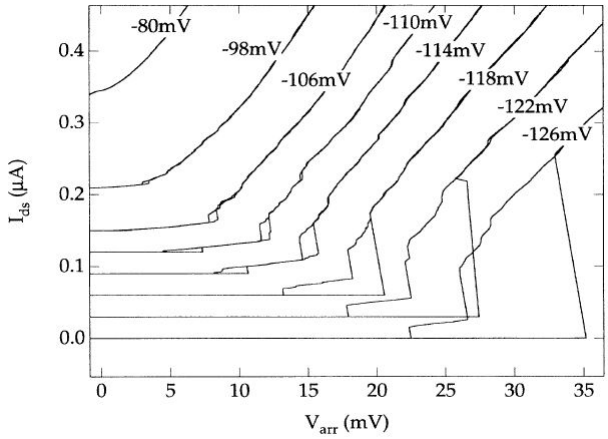

Figure 4.2: $I_{ds} - V_{arr}$ characteristic at $T = 20mK$ at different V_g.[26]

As V_g became more negative, hysteresis loops appeared which coalesced between $V_g = -114mV$ and $V_g = -118mV$. The hysteresis loops were counterclockwise in V_{arr}.

In other words, the positive voltage sweep switched to the conducting state at a larger bias than when it switched to the zero current state.

Sudden switching events, or spikes in the magnitude of I_{ds}, occured multiple times in the $I_{ds} - V_{arr}$ sweep. For instance, for $V_g = -118mV$ on the downward sweep, there were 3 sudden drops in the $I_{ds} - V_{arr}$ characteristic. Furthermore, the authors found that the width of the hysteresis loop increased by applying a more negative V_g. Figure 4.3 shows the temperature dependence of the $I_{ds} - V_{arr}$ characteristic at a constant $V_g = -115mV$.

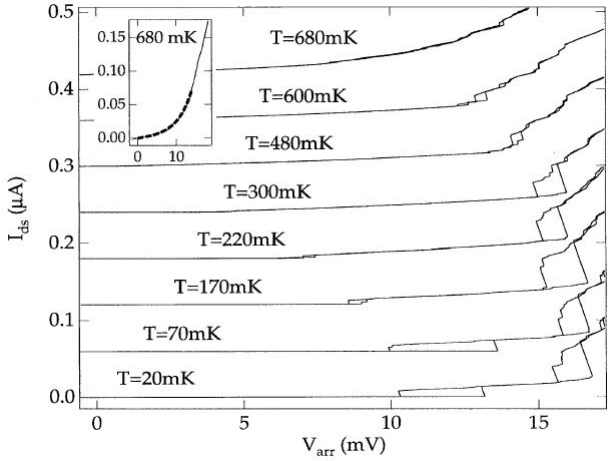

Figure 4.3: Temperature dependence of the $I_{ds} - V_{arr}$ characteristic with $V_g = -115mV$. Inset: $I_{sd}(V_{arr})$ at $T = 680mK$ fit to an activated form. Hysteresis loops are visible below $T = 680mK$.[26]

As a function of increasing temperature the width of the hysteresis loops and switching voltage decreased. At $T = 4.2K$, the hysteresis disappeared for all V_g and for all samples measured. Around $T = 680mK$, the $I_{ds} - V_{arr}$ obeyed an activated form near zero bias as seen in the inset. The functional form, from a two parameter fit of the data, is $I_{ds}(V_{arr}) = 3.4nA \times \sinh(0.27mV^{-1} \times V_{arr})$. The authors did not give a physical explanation for this functional form of the $I_{ds} - V_{arr}$ characteristic at higher temperatures.

Finally, the authors fit their non-hysteretic $I_{ds} - V_{arr}$ characteristics to MW's theory at seen in Figure 4.4. The scaling exponent for $V_g = -148mV$ was $\zeta = 1.47$. For

$-160mV \leq V_g \leq -145mV$, $1.4 < \zeta < 1.7$ was found. Furthermore, the threshold voltage V_T was found to decrease with less negative V_g.

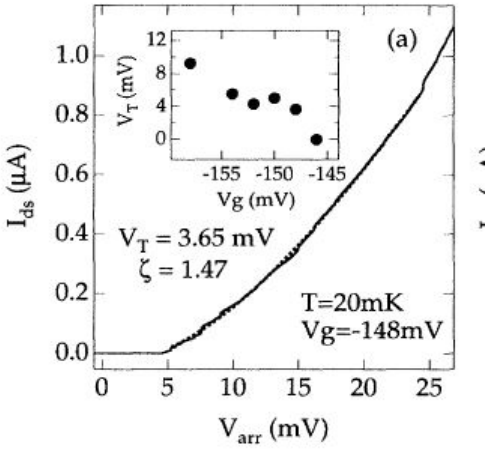

Figure 4.4: Fit to MW theory.[26]

The next experimental confirmation of MW theory was done by measuring the $I_{sd} - V_{sd}$ characteristics of 1D and 2D arrays of normal metal islands separated by tunnel junctions.[40] The normal metal islands were composed of $Al/Al_2O_3/Al$ tunnel junctions fabricated by electron beam lithography on a Si substrate. The arrays were cooled down below the superconducting transition temperature of Al and driven normal by applying a 0.5T perpendicular magnetic field.

The $I_{sd} - V_{sd}$ characteristics were measured in a four terminal configuration in a dilution refrigerator at $T = 30mK$. The 1D array was composed of 440 islands, and the 2D array was composed of 38 islands. Both the 1D and 2D junctions were in the short screening length limit ($\lambda \approx 0.6$). This was computed from a measurement of C and C_G for the 1D and 2D arrays. Figure 4.5 a,b shows the $I_{sd} - V_{sd}$ characteristic for a 1D array (a) and a 2D array (b).

For both 1D and 2D arrays, a threshold voltage (V_T) and a depinning $I_{sd} - V_{sd}$ characteristic (Equation 2.14) were observed. At high V_{sd}, the $I_{sd} - V_{sd}$ characteristic was linear for both types of arrays. Interestingly, V_T was found to vary as a function of time, on a scale of hours. The authors attributed this to mobile impurities in the substrate. The time averaged value for V_T was $9.4 \pm 0.3mV$ and $230 \pm 20\mu V$ for 1D and

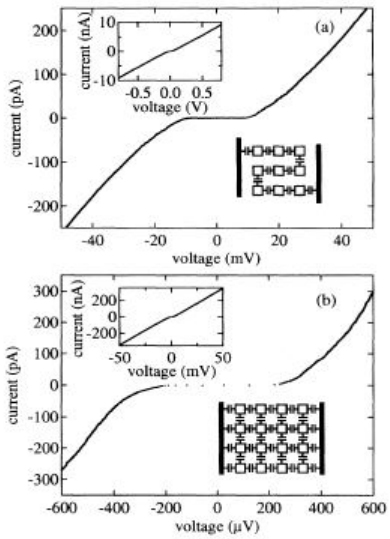

Figure 4.5: $I_{sd} - V_{sd}$ characteristic of a 1D (a) and 2D (b) array.[40]

2D arrays respectively. In comparison to MW's theory, the measured V_T was smaller than the calculated V_T by a factor of 1.5 (1D) and 2.5 (2D).

The authors stated that the cause of this discrepency, at least in 2D, was due to the disorder realization in the actual samples. As opposed to the stochastic disorder assumed in the MW model, a more slowly varying electrostatic potential in the 2D array makes it easier for electrons to pass around peaks in the electrostatic potential landscape. This doesn't happen in 1D arrays.

In addition, the authors fit their data to $I_{sd} \sim (V_{sd}/V_T - 1)^{\zeta}$, Equation 2.14. Figure 4.6 shows a log-log plot $I_{sd} - V_{sd}$ characteristics for 1D and 2D array fit by the theory.

The fits for both arrays were done so as to maximize the value of the exponent in the power law over the largest current range. The range was 2.5 and 4 orders of current, corresponding to $0.1 \leq (V_{sd}/V_T - 1) \leq 8$, for 1D and 2D arrays respectively. The extracted value of ζ was $\zeta_{1D} = 1.36 \pm 0.1$ and $\zeta_{2D} = 1.8 \pm 0.16$. The authors did not discuss the discrepency between their measured values and the values computed by MW nor did they carry out a systematic analysis of the temperature dependence of the $I_{sd} - V_{sd}$ characteristic and V_T. They stated that at $T = 60mK$ the shape of $I_{sd} - V_{sd}$ characteristic and the value of V_T for both types of arrays remained unchanged.

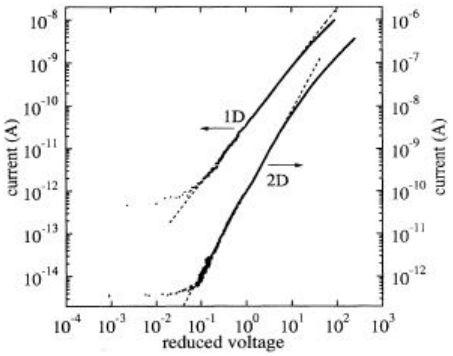

Figure 4.6: Scaled $I_{sd}-V_{sd}$ characteristic. The reduced voltage is equal to V_{sd}/V_T-1.[40]

The final model system I will discuss is that of Au nanocrystal monolayers as studied by Parthasarathy *et al.*.[28, 29] The purpose of these experiments was to investigate the role of structural disorder and network topology on transport through 2D arrays. We begin by discussing nanocrystal array fabrication and then their measurement and resultant data.

The Au nanocrystal monolayer arrays were deposited onto a Si wafer coated with 100nm of amorphous Si_3N_4. The typical radii of the Au nanoparticles were measured to be between 2 to 3 nm via transmission electron microscopy (TEM). The Au nanoparticles were surface terminated with dodecanethiol ligands due to the process technique. The array was placed on top of a region of the wafer ($70\,\mu m$ by $70\,\mu m$) where the Si, but not the Si_3N_4, was etched away. The Si_3N_4 window was used to characterize the array by TEM. A cartoon of the device, the interparticle geometry and the TEM images of different nanoparticle arrays are shown in Figure 4.7.

Depending on the concentration of nanoparticles in solution and solvent concentration, the authors fabricated arrays with either short range structural order (SRSO) or long range structural order (LRSO). Typically, nanoparticles produced without excess dodecanethiol in solution produced arrays with SRSO and large voids between the ordered areas as seen in Figure 4.7a. On the other hand, nanoparticles produced with excess dodecanethiol in solution produced arrays with LRSO seen in Figure 4.7 c,d. The typical size of arrays ($N \times M$) measured were $N = 20$ to 30 nanoparticles long by $M = 270$ nanoparticles wide. 20nm thick Cr electrodes were patterned by electron beam lithography to contact the array.

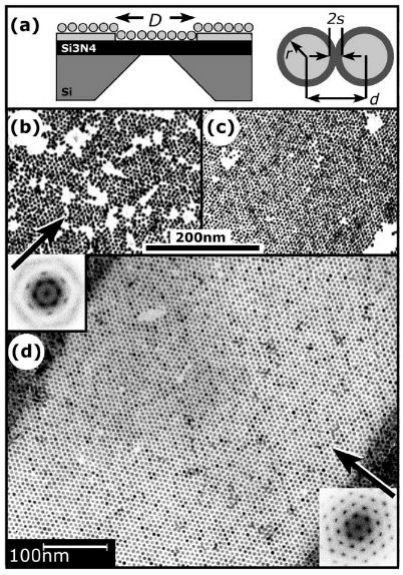

Figure 4.7: Cartoon of device and nanoparticle (a) and TEM images (b) of a SRSO array, (c),(d) of a LRSO array.[28]

As opposed to the two previous experiments, the Au nanocrystal array was not back gated and thus C_G did not play a role in determining the screening length, λ. Instead, the two dominant capacitance scales were due to the self-capacitance of the nanoparticle (C_0) and the interparticle capacitance (C_{12}). C_0 was caused by random charged impurities, quenched disorder, in the substrate, inducing electrons on a nearby nanocrystal, while C_{12} was due to the inter nanoparticle geometry. From TEM measurements of the particle and interparticle geometry and by using the dielectric constant of dodecanethiol (≈ 2), C_0 and C_{12} were determined, $C_0 \approx 0.5aF$ while $C_{12} \approx 0.25aF$. The Coulomb Blockade conditions were satisfied as well, for all measured temperatures.

Measurements of the $I_{sd} - V_{sd}$ characteristic were done in a ^4He cooled cryostat using external Keithley electrometers and voltmeters. Fourteen arrays were measured in total, half with LRSO and the other half with SRSO. Figure 4.8 is an $I_{sd} - V_{sd}$ characteristic for one of these devices at $T = 12K$ and $T = 77K$, although it was not specified whether or not it was an array with LRSO and SRSO.

As seen in Figure 4.8, the $I_{sd} - V_{sd}$ characteristic depended weakly on temperature, both close to and way from V_T. Figure 4.9 shows the scaled forms of the $I_{sd} - V_{sd}$

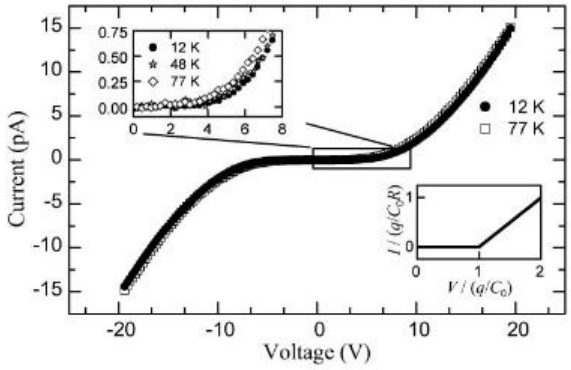

Figure 4.8: Temperature dependence of the $I_{sd} - V_{sd}$ characteristic.[29]

characteristic for LRSO arrays (a) and for SRSO arrays and (b). Figure 4.9c is a plot of the measured for V_T both both types of arrays with the straight line being MW's theoretical form for V_T.

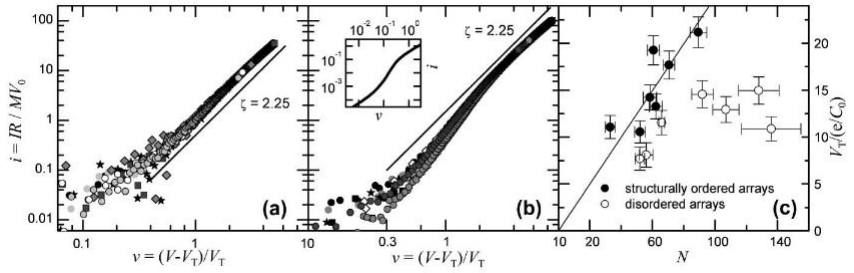

Figure 4.9: Scaling results for LRSO array (left), SRSO array (center), V_T for both type of arrays.[28]

In Figure 4.9, V_0 and M were the offset voltage due to the nanoparticle's self-capacitance and the width of the array respectively. Furthermore, the values for the interparticle tunneling resistance, R, were adjusted to scale all the data. $R = 50T\Omega$ for SRSO arrays and $R = 300T\Omega$ for LRSO arrays. The difference in the value of R results from the change in the tunneling distance ($2s$), since $R \sim \exp(s)$, due to the lack or excess of dodecanethiol. $s = 0.84 \pm 0.1nm$ for SRSO and $s = 1.2 \pm 0.1nm$ for LRSO arrays.

In LRSO arrays, $\zeta = 2.25 \pm 0.1$ for all seven arrays. However, in the case of SRSO

arrays, ζ was not necessarily constant over the full range ν. The authors explained the transport in the SRSO array in terms of the topology of the nanoparticle network. If there are many large voids in the nanoparticle array, local regions of structural order were separated from one another by bottlenecks. One-dimensional bottlenecks connect different 2D array regions. Conduction through the array is impeded by many parallel 1D paths each with a different V_T. Therefore, when V_{sd} is slightly above the smallest V_T, a single path carries the current and $I_{sd} \sim (V_{sd}/V_T - 1)$. As V_{sd} increases above the other larger V_T for different paths, conduction through the array is essentially 2D and thus $I_{sd} \sim (V_{sd}/V_T - 1)^{\approx 2}$.

A final comment on this experiment is geared towards the values of V_T. As seen in the far right hand side of Figure 4.9, V_T, normalized in terms of nanoparticle's self charging energy, increases with N. The constant of proportionality (α) is equal to 0.25 ± 0.02. For 2D square arrays the computed MW result is $\alpha = 0.338$ in the limit of $C_{12}/C_0 \to 0$. The authors state that this difference is because LRSO arrays are hexagonal arrays instead of idealized square arrays. $C_{12}/C_0 \approx 0.4$ and thus α was suppressed. On the other hand, V_T for SRSO arrays varied between arrays since N was not well defined.

In summary, I have presented three different experiments on model systems to test MW's theory. Each experiment provided evidence for a dynamical phase transition in quantum dot array transport by observing a V_T and critical phenomenon like power law $I_{ds} - V_{sd}$ characteristic. However, each experiment measured scaling exponents for both 1D and 2D arrays different from those predicted by MW. The discrepency suggests that either additional simulations on 2D arrays larger than 400×400 should be carried out, or MW's theory is incomplete.

4.2 Thermally Activated Phase Slips and Magnetic Field Tuned Reenterant Superconductivity in Nanowires

In this section, I discuss the original experiments whose goal was to investigate the origin of dissipation in quasi-1D superconducting nanowires. Experimentalists verified LAMH's theory and showed that TAPS were indeed the source of dissipation in the fluctuation regime $T < T_c$. Due to advances in electrochemical and lithography process

techniques, the effect known as the anti-proximity effect, or magnetic field induced reentrance to superconductivity was not observed until recently.

We begin with the experiments by Lukens *et al.*[30] These experiments were done on tin ($T_c = 3.7K$) whiskers whose cross sectional areas were smaller than $\xi_{GL}(T = 0)$. Although not mentioned in the original paper, the lengths of the whiskers were a fraction of a millimeter long, as mentioned by Tinkham.[11] The tin whiskers were fabricated by mechanically pulling tin plating from commercially available tin cans. The $I - V$ characteristics and $R(T)$ were measured in a ^4He cooled cryostat with an external Keithley DC current source and nanovoltmeter. Figure 4.10 is an $I - V$ characteristic of one of these devices at a constant temperature below T_c.

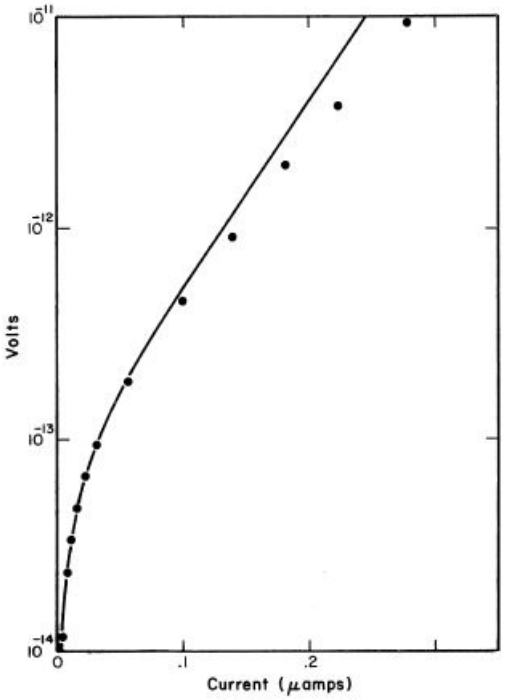

Figure 4.10: $I - V$ characteristic from Lukens *et al.*[30]

The solid line in Figure 4.10 is fit by Equation 3.31 at constant temperature. At low currents, Equation 3.31 fit the data is well while at higher currents there is a departure. The authors stated that the departure from the simple $sinh(x)$ form was due to the lack of inclusion of higher order, current dependent prefactor terms in Equation 3.31.

Furthermore, Lukens *et al.* measured the $R(T)$, in the low current limit, below T_c and fit it by Equation 3.32.

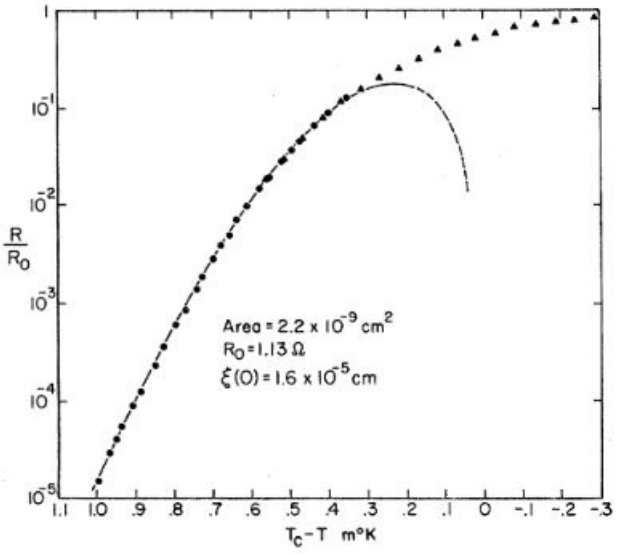

Figure 4.11: $R(T)$ of Lukens *et al.*[30]

The follow up experiment to Lukens' work was an experiment done by Newbower *et al.*[31] As opposed to the low current limit as done by Lukens *et al.*, Newbower *et al.* measured the $R(T)$ of tin whiskers in the high current limit of Equation 3.31. This limit occurs when $I > I_0 = 4ek_BT/h$. Unlike Lukens *et al.*, Newbower *et al.* included a parallel channel for normal electrons in their $R(T)$ fit, as seen in Figure 4.12.

The fit works over nearly six orders of magnitude in R/R_N within $3mK$ of T_c. The deviations from the fit at the very low resistance portion ($R/R_N \sim 10^{-6}$) of the plot were believed to be caused by the contacts to the tin whiskers.

Historically, research interest in TAPS experiments tapered off after these publications. The biggest constraint in the 1970s was the lack of an "easy" method to produce high quality quasi-1D nanowires. However, beginning in the 1980s, electron beam lithography and process techniques advanced to a level whereby it became much more feasible to produce narrow quasi-1D superconducting wires from a material of choice. Thus, it was not until 1989 that any experiment showed the novel effect of negative magnetoresistance ($R(H)$) in a quasi-1D superconducting nanowire. This was the precourser to

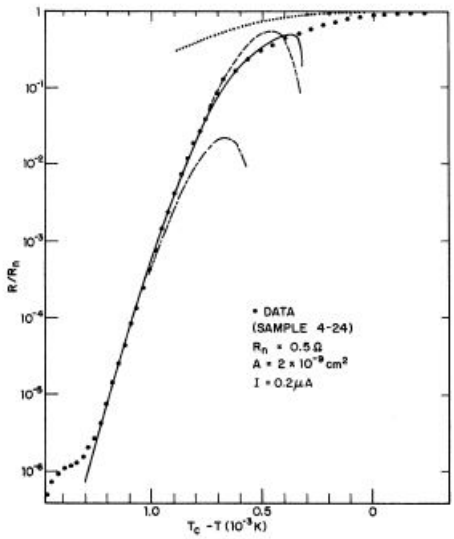

Figure 4.12: $R(T)$ of Newbower *et al.*[31]

the measurements of the magnetic field tuned reentrant behavior measurements of the last decade.

This work was done Santhanam *et al.*[32] Santhanam *et al.* set out to examine the Little-Parks effect in loops made of quasi-1D superconducting nanowires. What they found was a negative $R(H)$ well below T_c. This negative $R(H)$ was also observed in single nanowires.

The authors prepared quasi-1D superconducting aluminum nanowires in the geometry shown in Figure 4.13. The narrow quasi-1D part of the device in Figure 4.13 had a width $w = 41nm$ and a length, $l = 3.35\mu m$ while the dimensions of the larger electrodes were $w = 0.48nm, l = 2.6\mu m$. The aluminum film thickness was $t = 35nm$. The resistance of the devices were measured in a 4-terminal geometry with a lock-in amplifier. From Figure 4.13, $T_c = 1.51K$ and $R_N \approx 200\Omega$ with the wire exhibiting a sharp superconducting transition.

In Figure 4.14, the $R(H)$ of the device, in a perpendicular H-field, at a low temperature and bias current ($T = 1.29K$ and $I_{rms} = 10nA$) showed a positive MR expected with the leads being driven normal at $H \approx 130Oe$ and the wire at $H = 750Oe$. In this case there was no negative $R(H)$.

However, when the wire was sufficiently driven out-of-equilibrium near T_c at $T =$

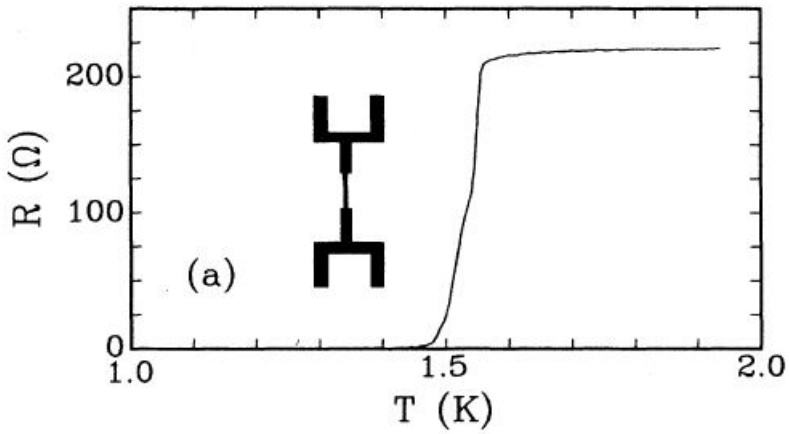

Figure 4.13: $R(T)$ of a nanowire of Santhanam *et al.*'s data with the nanowire device geometry in black.[32]

$1.48K$ and $I_{rms} = 2\mu A$, the $R(H)$ showed a suppression, a negative $R(H)$ for $H < 20Oe$, as seen in the inset of Figure 4.14. This was interpreted in terms of a N-S interface between the nearly normal wire and the superconducting leads.

Microscopically, the negative $R(H)$ was attributed to the H-field dependence of the quasiparticle relaxation length,L_{QP}, in the wire. The resistance of the interface between the out-of-equilibrium wire and the superconducting leads depends on L_{QP} via

$$R_{QP(Q^*)} = \frac{2R_\square}{w}(1 - \frac{\pi\Delta(T)}{4k_BT})L_{QP} \tag{4.1}$$

where $R_\square$ is the normal state sheet resistance of the film, w is the wire width, and $\Delta(T)$ is half the BCS gap energy.

The authors computed L_{QP} which takes the form valid for $\Delta(T)/k_BT < 1$.

$$\frac{1}{L_{QP}} \simeq (\frac{\pi\Delta(T)}{4k_BT})^{1/2}\frac{1}{l_{in}(T)}(1 + \frac{l_{in}^2(T)}{\xi^2(T)}(\frac{1}{3}(\frac{I}{I_c(T)})^2 + (\frac{H}{H_{c,||}})^2))^{1/4} \tag{4.2}$$

where $l_{in}(T)$ is the normal state electronic inelastic scattering length, $\xi(T)$ is the dirty limit GL coherence length, I is the current, $I_c(T)$ is the critical current, H is the magnetic field and $H_{c,||}$ is the transverse critical field of the wire.

The rather complicated form of L_{QP} made fitting to the measured $R(H)$ difficult, and thus the authors made only qualitative comparisons between the calculated curves,

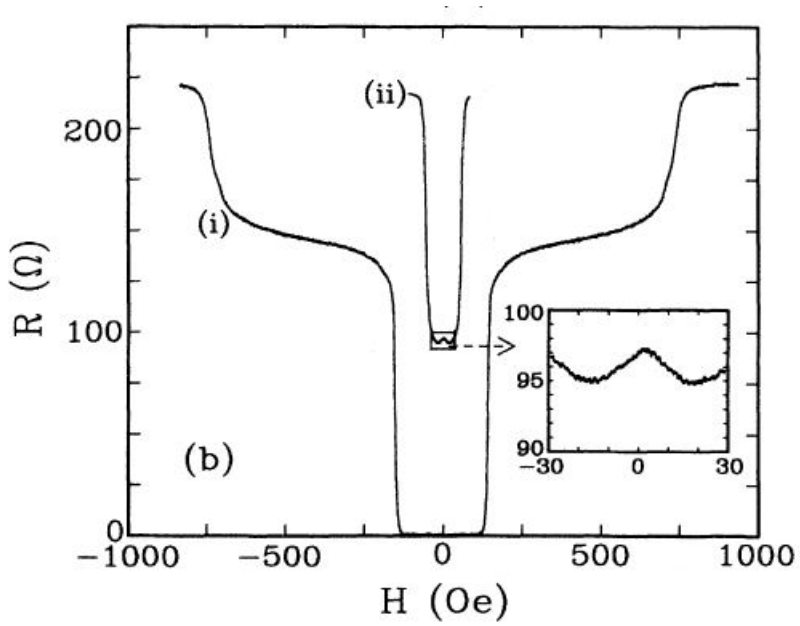

Figure 4.14: $R(H)$ of the device at two different temperatures (i)$T = 1.29K$, (ii)$T = 1.48K$. The inset is the region of negative magnetoresistance.[32]

presented in Figure 4.15, and the measured $R(H)$ curves.

Moving ahead 15 years, research interest in superconducting nanowires sprung up again because of applications. Superconducting nanowires serve as the basic interconnects of superconducting qubits. This set the stage for 2005 when zinc nanowires, prepared via electrochemical means, were found to develop superconducting order upon the application of a weak magnetic field, an effect called the anti-proximity effect.[33]

The experimentalists sought to verify the following claim: if a quasi-1D superconductor is coupled to bulk leads, leads with a higher T_c, should not superconductivity in the nanowire be more robust due to the proximity effect? Our intuition for bulk superconductivity would say yes. However, what was found was that when the bulk superconducting electrodes were driven normal by a perpendicular H-field, the nanowires reentered the superconducting state.

The zinc nanowires were fabricated by a template assembly electrodeposition technique. Wires were grown in a porous membrane template, composed of polycarbonate and anodic aluminum oxide, via an electrochemical technique. The widths and lengths

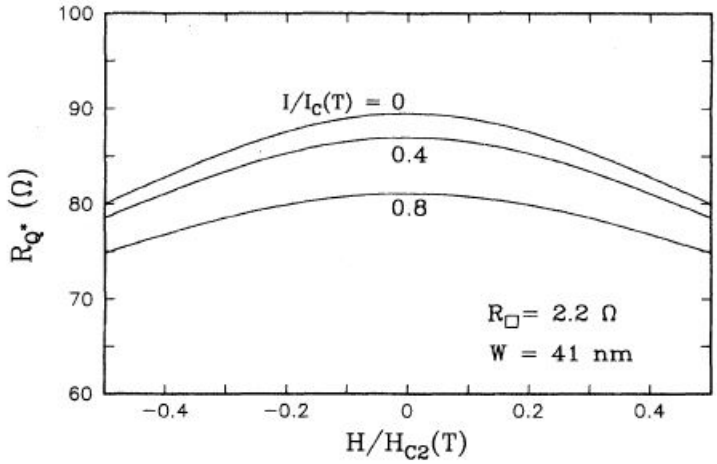

Figure 4.15: Calculated $R_{Q^*}(H)$ curves (Equations 4.1-4.2) for $I/I_c(T) = 0, 0.4, 0.8$.[32]

of the nanowires could be controlled by varying the pore size of the membrane and the length of the membrane respectively. Tian *et al.* produced wires of width 40 and 70 nm and length $2\mu m \leq L \leq 35\mu m$ Figure 4.15 is a transmission electron microscope (TEM) micrograph of a set of nanowires.

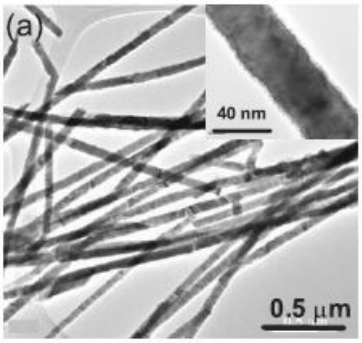

Figure 4.16: TEM micrograph of the nanowires.[33]

The 2-terminal resistance and $I - V$ characteristic were measured by mechanically squeezing tin or indium bulk leads onto the ends of the membrane. $R(H, T)$ and the $I-V$ characteristic were measured in a Quantum Design Physical Properties Measurement System (PPMS) with a ^3He refrigerator insert. Figure 4.17 is a cartoon of the devices

accompanied by two $R(T)$ plots for wires of $w = 40nm$ and $w = 70nm$. Since $\xi_{GL}(T = 0) \approx 155nm$, the zinc wires were in the quasi-1D superconducting limit.

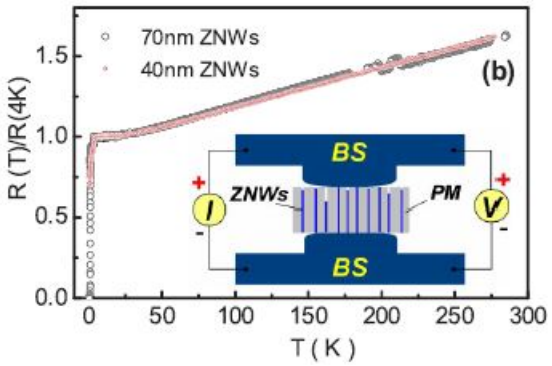

Figure 4.17: $R(T)$ and cartoon of the devices.[33]

Figure 4.18 is a set of $R(T)$ and $I - V$ characteristic for several zinc nanowires ($w = 40nm$) contacted with indium bulk electrodes. The length of each wire was noted in the $R(T)$ plot.

We first consider Sample Z3 in the top $R(T)$ plot and $I - V$ characteristic in Figure 4.18. As the temperature decreased, the first resistance drop occured at $T = 3.4K$ at the T_c of In. A broad superconducting transition of the zinc nanowires occured around $T = 1K$, but the wire remained resistive down to base temperature of $T = 470mK$. Upon applying a magnetic field $H = 0.3kOe$, the superconducting transition became less broad and the resistance decreased by nearly 75% at lowest temperatures. However, the wire remained resistive and did not fully reenter the superconducting state. Increasing the H-field drove the nanowires resistive until superconductivity was destroyed at $H = 2.1kOe$. As seen in the inset, the $I - V$ characteristic at $T = 470mK$ was Ohmic when $H = 0Oe$. Increasing $H = 0.3kOe$ suppressed the normal current and thus part of the current was carried by the supercurrent until $I \approx 1.25\mu A$.

Decreasing the wire length enhanced the anti-proximity effect, as seen in Sample Z4 in the middle plot of Figure 4.18. Unlike the $L = 6\mu m$ wire, $R(T)$ did not have a superconducting transition near $T = 1K$. Instead, $R(T)$ decreased continuously down to the lowest temperatures. But, turning on a field of $3kOe$ caused the wires to develop superconducting order as $R(T)$ developed a superconducting dip near $T = 1K$. Like

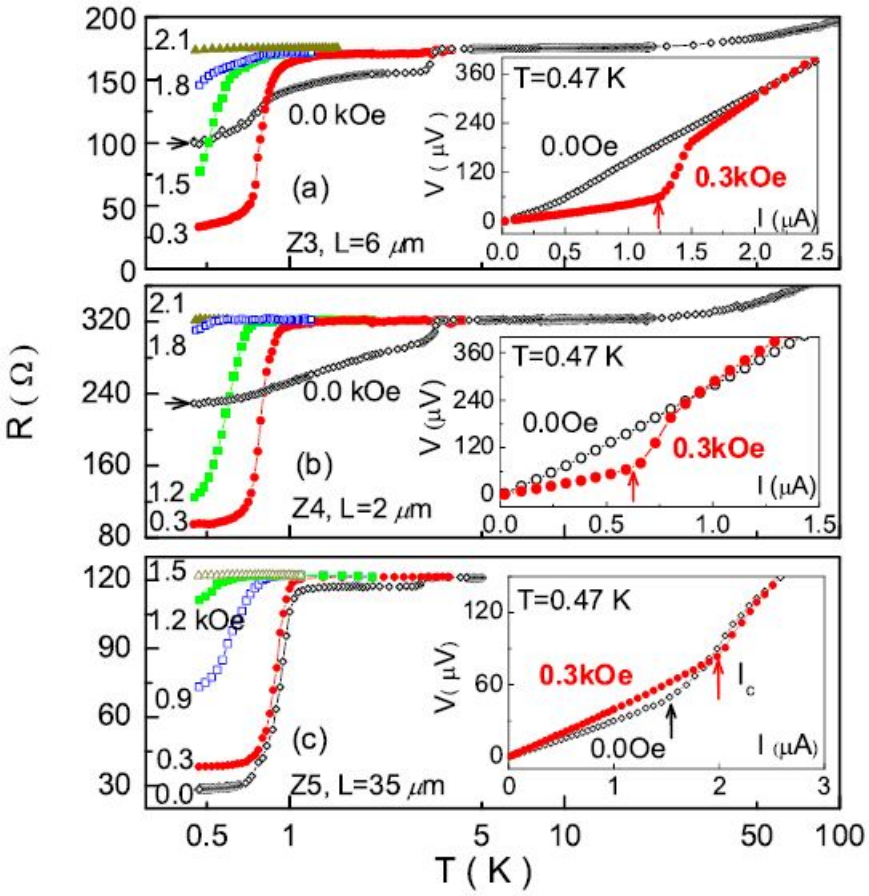

Figure 4.18: $R(T)$ data for three devices.[33]

the $L = 6\mu m$ wire, applying $H = 2.1kOe$ destroyed superconductivity in the leads and the wire. In addition, the anti-proximity effect was seen in $R(H)$ in Figure 4.19. For $T < 750mK$, there is a resistive plateau at low H-fields which disappeared at $H = 0.270kOe$ suggestive of incipent superconducting order in the nanowire.

The anti-proximity effect disappeared in the $R(T)$ for $L = 35\mu m$, Sample Z5, as seen in the bottom most plot in Figure 4.19. The authors noted that I_c was enhanced as seen in the $I - V$ characteristic at $T = 470mK$. At the time, there was no known complete explanation of the effect.

The enhancement and suppression of the anti-proximity effect with the wire length

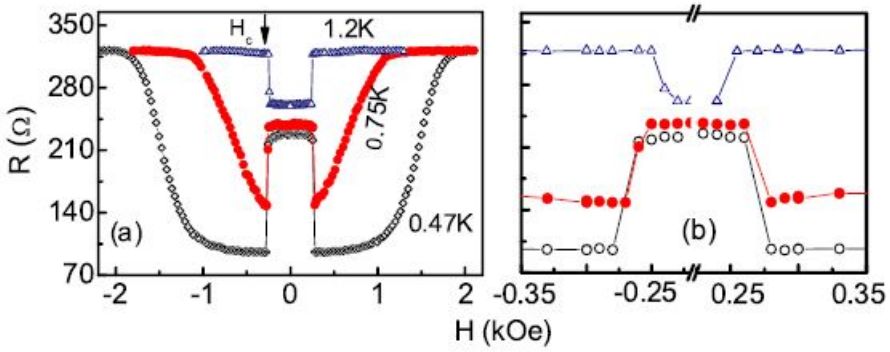

Figure 4.19: $R(H)$ data for one of these devices.[33]

L was suggestive of the interplay of two length scales associated with superconductivity. As we will see in the next set of experiments, the anti-proximity effect and magnetic field re-entrant superconductivity occur when $\xi_{GL} < L < L_{QP}$.

Following this work, Chen *et al.* set out to study the phenomenon in zinc nanowires but using electron beam lithography techniques and lift-off to fabricate the devices. Chen *et al.* patterned a single nanowire, connected to thin film I and V probe leads seen in Fig. 4.20.[34, 35]

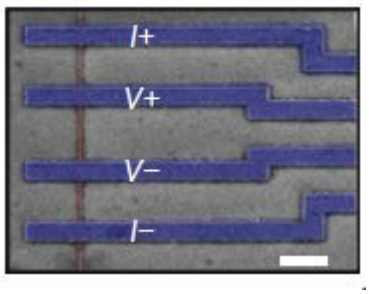

Figure 4.20: A SEM micrograph with false color plot.[35]

The devices had transparent interfaces between the nanowire and leads in a 4-terminal geometry. Chen *et al.* measured the nanowires in a Quantum Design PPMS with a ^3He refrigerator insert and in an Oxford Kelvinox 400 dilution refrigerator. They found that when the nanowires were driven out-of-equilibrium, QPs formed a novel non-equilibrium distribution function caused by Andreev reflections of QPs at the

nanowire-lead interface. This created a dissipative state, seen in the $I-V$ characteristic as a constant voltage plateau, to coexist with the superconducting state. This voltage plateau was suppressed in the presence of a weak H-field which caused the wire to reenter the superconducting state when driven resistive below T_c.

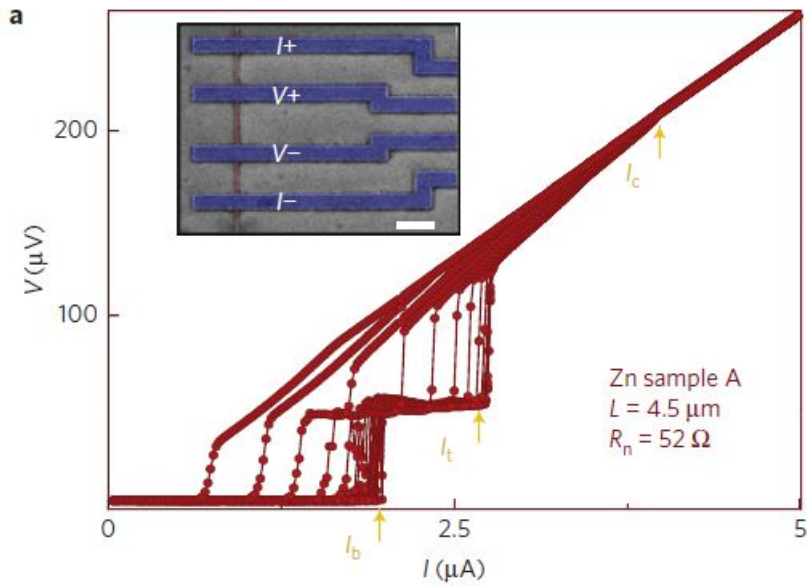

Figure 4.21: Temperature dependence of the $I-V$ characteristic. From left to right in the figure, the temperature varies from $T = 750mK \rightarrow T = 50mK$ for each $I-V$ characteristic trace.[35]

Figure 4.21 shows the temperature dependence of the $I-V$ characteristic for one of these wires. The transverse dimensions of the wire are $w = 100nm$ and $h = 65nm$; $T_c = 760mK$. Around and below 650mk, the voltage plateau (V_0) appears which nearly constant between currents $I_b < I < I_t$. For zinc, this plateau occurs at $V_0/\Delta_0 = 0.43 \pm 0.05$, where $\Delta_0 = 3.528 k_B T_c$ is the zero temperature BCS energy gap value, for all samples. Upon increasing the current to I_c the wire is driven completely normal for all measured temperatures.

It is also helpful to visualize the superconducting properties of this nanowire in temperature-current phase space as seen in Figure 4.22.

Again, the voltage plateau appeared when $T \leq 650mK$. Furthermore, qualitatively

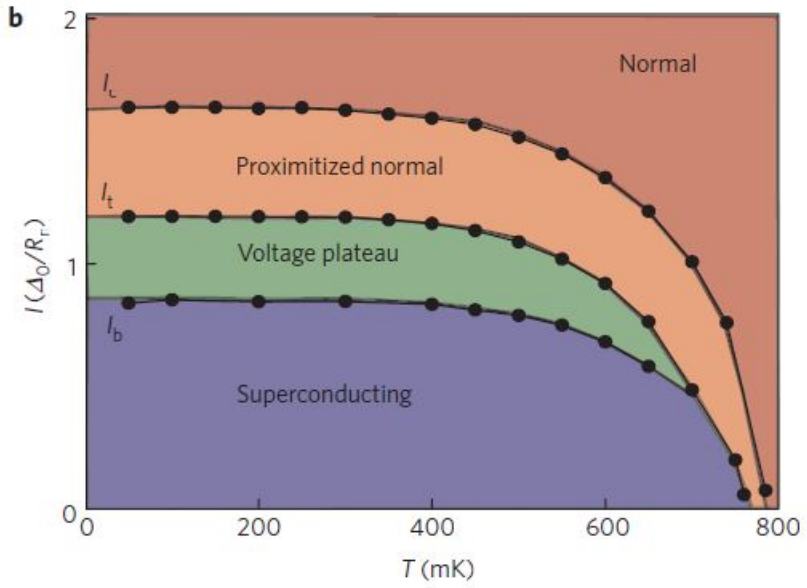

Figure 4.22: Temperature-current phase space diagram.[35]

speaking, the temperature dependence of both I_b, I_c looked like that of a superconducting order parameter. In Figure 4.23, weak, perpendicular to the plane, H-fields suppressed V_0 and caused it to collapse.

The voltage plateau was completely suppressed at a $H = 19Oe$. Thus, if one applied a current $I_b < I < I_t$ to drive the wire out-of-equilibrium and got "stuck" on the V_0 part of the $I - V$ characteristic a H-field caused the dissipative current to return to a supercurrent. Figure 4.24 is the magnetic field-current phase space diagram of a device.

Another remarkable feature of V_0 was its inherent stochastic bistability. By biasing the nanowire between $I_b < I < I_t$ and sampling the voltage plateau as a function of time, the plateau switched between the voltage plateau state, V_0, and the superconducting state. This is shown in Figure 4.25, for $I = 1.95\mu A$ at $T = 50mK$ with a measurement rate of $3Hz$ and $H = 0Oe$.

Chen *et al.* then quantified this bistability by measuring the mean time the nanowire remained in either V_0 or the superconducting state (τ_{vp}, τ_{sc}) respectively. As a function of current bias, τ_{vp} increased nearly two orders of magnitude with increasing bias current. On the other hand, τ_{sc} decreased an order of magnitude as a function of current as seen

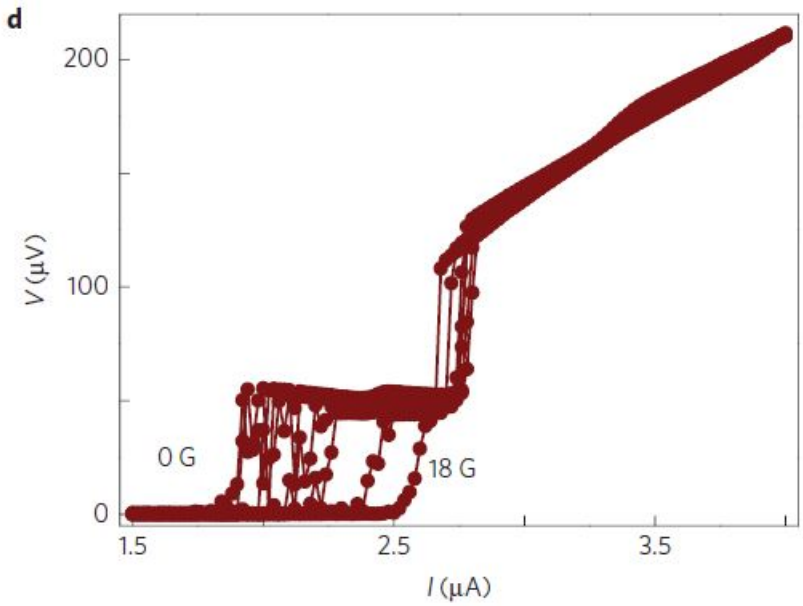

Figure 4.23: Magnetic field dependence at $T = 50mK$.[35]

in Figure 4.26.

As a function of H-field, for $I = 1.95\mu A$ at $T = 50mK$, τ_{vp} was suppressed while τ_{sc} increased an order of magnitude. The most important aspect of the work of Chen *et al.* was the microscopic description of the V_0 state.

To begin with, for this effect to be observed, one needs a nanowire of length L to be within the following limits, $\xi_{GL} < L < L_{QP}$. In their case, $\xi_{GL}(T = 0) \approx 250nm$ and $L_{QP} \approx 10\mu m$. All of the wires measured had $1.5\mu m < L < 6\mu m$. Thus, non-equilibrium QPs, generated by phase slips at the center of the wire, diffuse over the length of the wire prior to relaxing back into the superconducting state.

When a QP reaches the nanowire-equilibrium electrode interface, it undergoes Andreev reflections, denoted by the spin up electron-like QP. This process creates a Cooper pair in the right lead and reflects a spin up hole-like quasiparticle. The hole-like quasiparticle then propagates to the left lead, combines with a Cooper pair from the left lead, and produces an additional normal current flowing back to the right lead.

The multiple Andreev reflections create a novel non-equilibrium distribution function for quasiparticles. This suppresses the gap ($\Delta(x)$) in the nanowire from the equilibrium

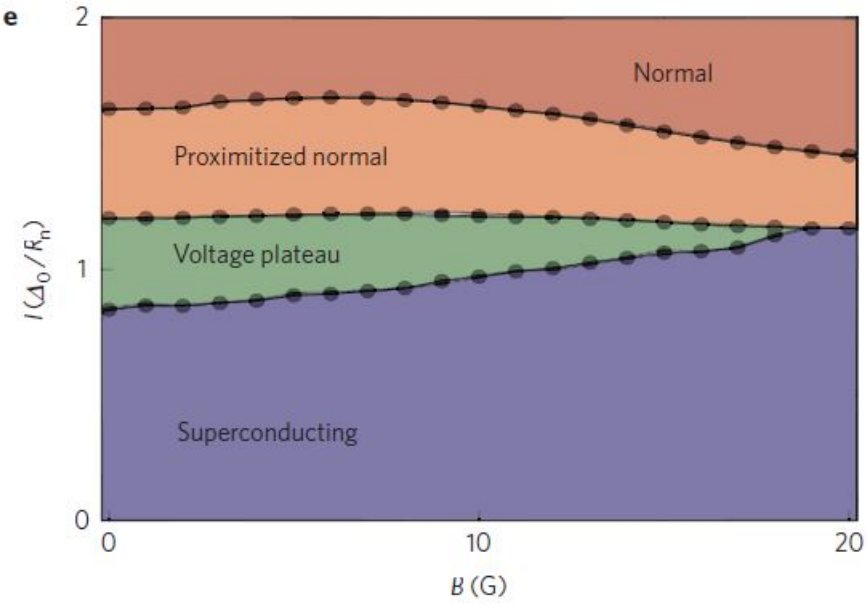

Figure 4.24: Magnetic field-current phase space diagram.[35]

value in the leads (Δ_0) due to the self-consistency relation. However, at the phase slip location, the portion of the wire develops a voltage (V). Thus, the equilibrium value of the chemical potential (μ) exhibits a discontinuity ($\mu = eV$) at the phase slip location. For a train of phase slips to occur, and thus create the dissipative state, the applied voltage must satisfy $eV_0 \approx 2\Delta$ as seen in Figure 4.28. This is more or less a hand waving argument for the phenomenon. A more rigorous theory is as follows.

The theory of the voltage plateau state begins with the parameterization of the energy and position dependent distribution function of QPs, $F(\epsilon, x) = 1 - 2n(\epsilon, x)$. Where $n(\epsilon, x)$ is the QP occupation number and ϵ is the energy of the excitation. Provided inelastic scattering events are suppressed and $\Delta(x)$ coincides with the local superconducting gap, we can assume that the odd and even parts of $F(\epsilon, x)$ satisfy a continuity equation known as the Usadel equation.

For non-equilibrium superconducting systems, according to Tinkham, $F(\epsilon, x)$ can be decomposed into two orthogonal components, the longitudinal and transverse distribution functions ($F_{L/T}(\epsilon, x)$). These are the odd and even parts of $F(\epsilon, x)$ and thus $F_{L/T}(\epsilon, x) = F(\epsilon+\mu_{1,2}, x) \mp F(-\epsilon+\mu_{1,2}, x)$ where $\mu_{1,2} = \pm eV/2$ is the chemical potential

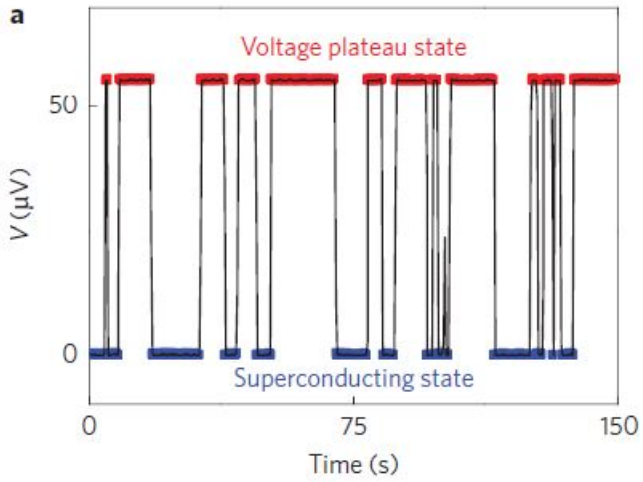

Figure 4.25: Bistability of the voltage plateau.[35]

in the left (1) and right (2) leads.

The Usadel equation then takes the form

$$\partial_t F_{L/T} + \partial_x (D_{L/T} \partial_x F_{L/T}) = 0 \tag{4.3}$$

The odd and even parts of the diffusion constant $D_{L/T}$ take on the values $D_L = D$, where D is the normal state electronic diffusion constant, and $D_L = D\epsilon^2/(\epsilon^2 - \Delta^2(x))$. The next step is to define the points where the QPs Andreev reflect. These points are defined as $x_{1,2}(\epsilon)$. In addition, $x_{1,2}(\epsilon) = \mp x(\mp\epsilon \mp V/2)$ due to parity and electron-hole symmetry. The steady state solution to Equation 4.3 for $\partial_t F_{L/T} = 0$ is

$$F(\epsilon, x) = F_L(\epsilon) + J_T(\epsilon)x \tag{4.4}$$

where, by electron-hole symmetry, $F_L(\epsilon) = -F_L(-\epsilon)$ and $J_T(\epsilon) = J_T(-\epsilon)$. $J_{L/T}$ are energy (L) and charge (T) currents. In the steady state, the currents and distribution functions are related by $\partial_x F(\epsilon, x) = J_{L,T}(\epsilon)$.

Furthermore, at the two interfaces between the nanowire and leads, the distribution function satisfies the following boundary conditions

$$F(\epsilon, x_{1,2}) = -F(-\epsilon \pm V, x_{1,2}) = 0 \tag{4.5}$$

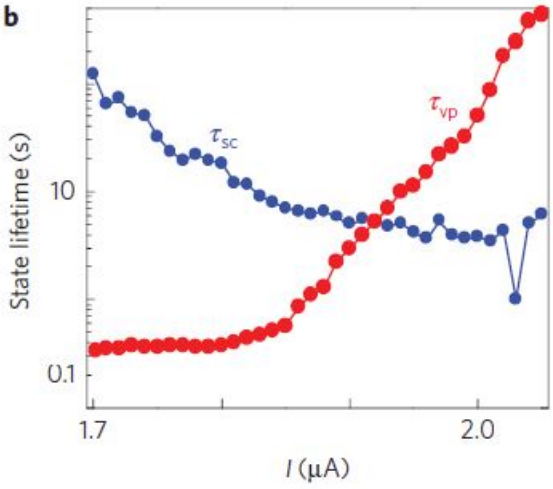

Figure 4.26: Current dependence of τ_{vp}, τ_{sc}.[35]

$$\partial_x F(\epsilon, x_{1,2}) = \partial_x F(-\epsilon \pm V, x_{1,2}) = 0 \tag{4.6}$$

If Equation 4.4 satisfies Equations 4.5-4.6, we find that

$$F_L(\epsilon + V/2) - J_T(\epsilon + V/2)x(\epsilon) = F_L(\epsilon - V/2) + J_T(\epsilon - V/2)x(\epsilon) \tag{4.7}$$

$$J_T(\epsilon + V/2) = J_T(\epsilon - V/2) \tag{4.8}$$

provided we shift the energy by $V/2$. In addition, provided $J_T(\epsilon) = J_T$ is constant, Equations 4.4 and 4.6 lead to

$$J_T = \frac{V}{2x(\epsilon)} \partial_\epsilon F_L(\epsilon) \tag{4.9}$$

Equation 4.3 takes the form

$$\partial_t F_L(\epsilon, t) = \partial_\epsilon (D(\epsilon) \partial_\epsilon F_L(\epsilon, t)) + I_{in}(F_L) \tag{4.10}$$

where $D(\epsilon) = DV^2/L^2(\epsilon)$, $L(\epsilon) = 2x(\epsilon)$ and I_{in} is the elastic relaxation term.

$$I_{in} = \frac{1}{\tau_{in}} (\tanh(\epsilon/2T) - F_L(\epsilon, t)) \tag{4.11}$$

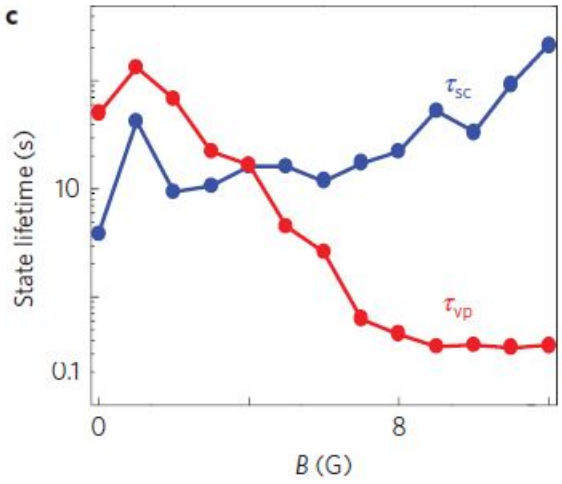

Figure 4.27: Magnetic field dependence of τ_{vp}, τ_{sc}.[35]

where τ_{in} is the inelastic scattering time.

The next part of the derivation will examine $\Delta(x)$ and $F_L(\epsilon)$. $F_L(\epsilon, x)$ satisfies the self consistancy equation below

$$\int_{\Delta(x)}^{\omega_D} d\epsilon \frac{F_L(\epsilon, x)}{\sqrt{\epsilon^2 - \Delta^2(x)}} = \int_{\Delta_0}^{\omega_D} d\epsilon \frac{\tanh(\epsilon/2T)}{\sqrt{\epsilon^2 - \Delta_0^2}} \tag{4.12}$$

In the case of a finite V_0, $\Delta(x)$ is locally suppressed from its equilibrium value Δ_0, $0 < \Delta < \Delta_0$. In order to allow for phase slips to produce QPs in the nanowire, $V \approx 2\Delta$. Here Δ is suppressed over a distance of ξ_{GL} in the center of the nanowire. This train of phase slips creates QPs at a frequency $f_{PS} \sim \Delta/4\hbar$. Thus, $F_L(|\epsilon| < \Delta) = 0$. The expression for the $F_L(\epsilon)$ is

$$F_L(\epsilon) = 0 \; for \, 0 < \epsilon < \Delta \tag{4.13}$$

$$F_L(\epsilon) = \frac{\epsilon - \Delta}{\Delta_{lead} - \Delta} \; for \, \Delta < \epsilon < \Delta_{lead} \tag{4.14}$$

$$F_L(\epsilon) = 1 \; for \, \Delta_{lead} < \epsilon \tag{4.15}$$

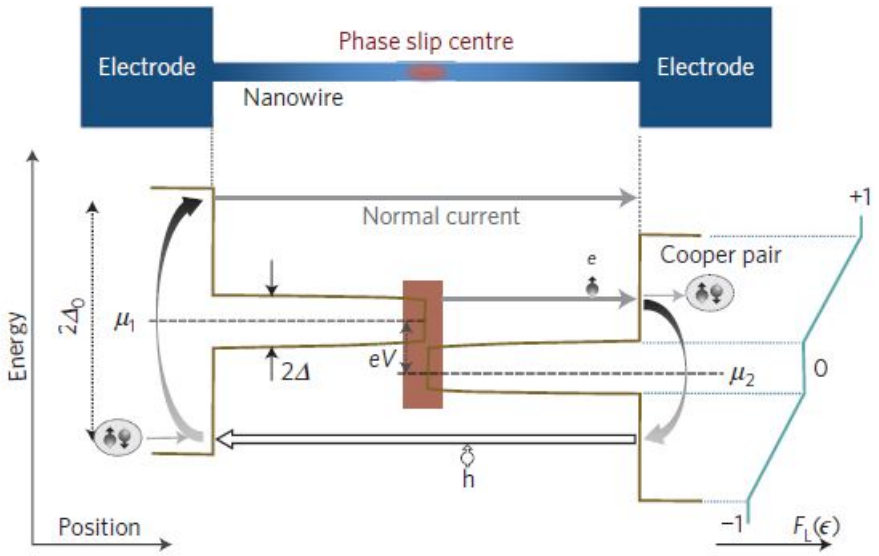

Figure 4.28: Order parameter as a function of position along the axis of the device.[35]

where Δ_{lead} is the finite temperature, equilibrium value for the lead order parameter. $\Delta_{lead} = \Delta_0$ if there is no magnetic field and $T = 0$. The next step is to take the three forms of F_L above and drop them into Equation 4.12. By evaluating this integral, one comes up with two solutions for Δ. One solution is when superconductivity exists without phase slips and the other solution is one with V_0.

More formally, following again Chen *et al.*, the self-consistant value for Δ is obtained from solutions of the following transcendental equation

$$\sqrt{1-\delta^2} - \ln(1+\sqrt{1-\delta^2}) + (1-\delta)\ln(\Delta_0/\Delta_{lead}) = \delta \ln(1/\delta) \tag{4.16}$$

where $\delta = \Delta/\Delta_{lead}$. For simplicity, if we assume that $\Delta_{lead} = \Delta_0$, $\delta = 1$ or $\delta = 0.17$ values correspond to a nanowire being superconducting with no phase slips and the V_0 state, respectively.

The values for the current limits I_b and I_t can also be computed using this theory. It turns out when the wire enters the voltage plateau state, part of the current $I_b = 0.64(V_0/R_n)$, must be suppled by a current source (I). Up to I_b, $I_s = I - I_b$, or, in other words, the rest of the applied current is carried by the supercurrent. If the current

source supplies $I_t = 0.72\Delta_0/eR_n$, $\Delta \to 0$ throughout the wire. At this point, the $I_s \to 0$ and the current is carried as a normal current.

Furthermore, the temperature scale for observing the effect is set by the value of the equilibrium order parameter, Δ_0. Equation 4.16 admits superconducting solutions with the V_0 state provided $\Delta_{lead} \geq 0.78\Delta_0$. Therefore, the effect will not be observable until $T \approx 0.78T_c$. The reason why there is a discrepency between this estimate ($T = 590mK$ for the sample above) and the observed value $T = 650mK$ for the disappearence of the effect is due to quasiparticle relaxation. Finally, the presence of a H-field suppresses the order parameter in the leads from its equilibrium value.

Now we have the background information for experimental transport in arrays of quantum dots and the experimental and theoretical backpinning for the magnetic field tuned reenterant superconductivity. I will discuss experimental techniques and the apparatus in the next chapter.

Chapter 5

Experimental Technique and Apparatus

In this chapter I will discuss the tools needed to study transport in ionic liquid gated and superconducting nanostructures. I hope provide concensus recipes of how to fabricate and to measure these devices. I will include necessary tips and pointers which were either passed down from previous graduate students or discovered by trial and error. Keep in mind that these are recipes which may or may not work for a different process or with different equipment.

5.1 Electron Beam Lithography

Electron beam lithography (EBL) is a highly non-trivial technique and requires years of work to master. We start with outlining the process flow for EBL, and then we will provide detailed recipes for patterning and processing. Many of these details are also available online.[36]

EBL is a lithography technique which uses a beam of high energy electrons ($100keV$) to draw patterns in a resist (an electron sensitive polymer) on top of a substrate, usually a Si wafer. One needs EBL to make devices with dimensions smaller than $100nm$ as opposed to photolithography, because EBL's resolution is not limited by diffraction at wavelengths associated with visible light.

For positive tone resists like Poly(methyl methacrylate) (PMMA), the electron beam

breaks bonds between cross-linked molecular chains, a process called chain scission. Post exposure, these lower molecular weight regions are highly soluble in a developer solution.

Developing away those regions defines the stencil mask for the device geometry. After depositing the metal of choice, the mask is dissolved and lifted off in a solvent. Figure 5.1 is a cartoon of an EBL process flow.

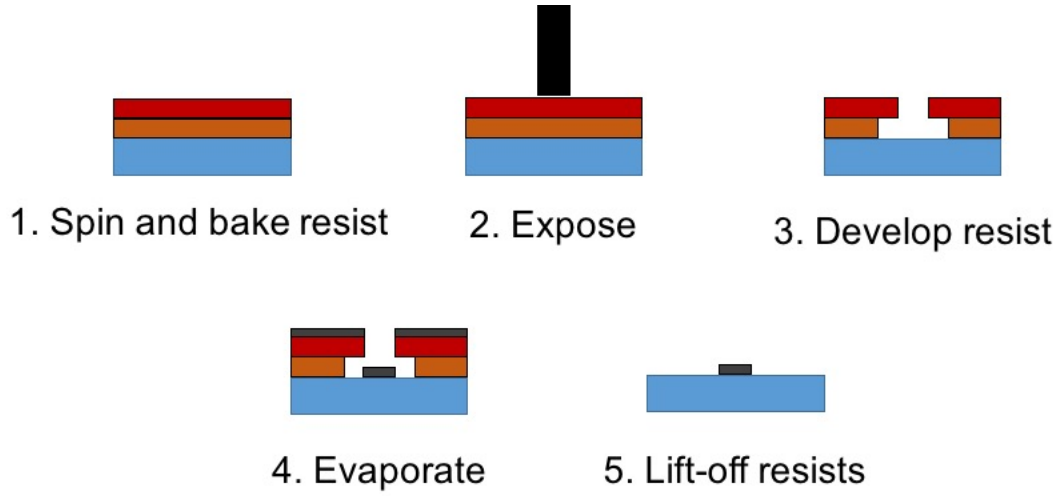

Figure 5.1: Cartoon of the electron beam lithography (EBL) process using a bilayer resist recipe. Red: PMMA resist, Orange: PMGI resist, Blue: Si wafer, Black: Electron beam, and Gray: Al thin film.

Typically, one should carry out a bilayer resist recipe with an imaging layer (PMMA) and an electron beam insensitive undercut layer made of a different polymer, such as Polymethylglutarimide (PMGI). This allows one to avoid fencing, or metal sticking to the side walls the resist.

The first step is to design a pattern employing computer aided design (CAD) software, either AutoCAD or LayoutEditor. The devices in this thesis were designed in LayoutEditor because it was free and readily available on the Minnesota Nanofabrication Center EBPG server.

Next, you need to fracture your Graphic Database System II (GDS II) file in LayoutBEAMER. In this step, one needs to correct for the proximity effect exposure caused by scattered electrons. As the beam of electrons travels through the resist and substrate, it undergos forward scattering events (due to the electron-electron interaction with atoms

in the resist and substrate) and backscattering events (due to electron-ion core interaction with atoms in the resist and substrate).[36, 37] Forward scattering causes the incident electron beam to be scattered by a small angle, while backscattering results in large angle scattering events.

The collective effects of forward and backscattering events cause regions of the resist to be inadvertantly exposed. If one wants to make sub-100nm dimensional structures with pitch less than 100nm, this is an issue. However, the built in algorithm provided by LayoutBEAMER corrects for this. It models the energy deposited into the resist by the electron beam at each pixel as the sum of two Gaussian point spread functions. One Gaussian distribution for forward scattered electrons and one Gaussian distribution for backscattered electrons.

In LayoutBEAMER, one should add a step to eliminate overlapping polygons in the GDSII file and set the resolution and beam step size to $1nm$ and $10nm$. These are typical parameters used for the EBPG 5000+ electron beam lithography system. This gives a pixel size of $10nm$.

The next step is to examine the fractured pattern in CVIEW and then move these files over to another software program, CJOB. In CJOB, one builds and exports the exposure file read in and executed by the EBPG5000+ system. Other than linking together your process flow, you need to determine two critical parameters for your process here. These parameters are the beam current and the dose. They are related by the following equation

$$Dose(\mu C/cm^2) = \frac{I_{beam}(\mu A) \times t_{dwell}(s)}{x_{step}^2(cm^2)} \tag{5.1}$$

where $t_{dwell} = 1/f_{DAC}$, digital-to-analog converter (DAC), and is the amount of time the beam "sits" at a given pixel. $f_{DAC} < 50Mhz$ is the frequency of the digital-to-analog converter for the electron beam. x_{step} is the beam step size.

Determining these parameters requires careful thought and is process dependent. Depending on the geometry of one's device, for argument's sake a $w = 100nm$, $L = 1.5\mu m$ nanowire, pixels need to overlap ($x_{step} = 10nm \sim 0.5\, spotsize$) and linewidth fidelity needs to be maintained ($w > 4-5 pixels$). For fabricating aluminum nanowires, a $I_{beam} = 10nA$, which has a typical step size of $20nm$, and a dose of $1000\mu C/cm^2$ works well. This dose and step size is above the shot-noise variations in the beam current.

This ensures repeatability during different exposures.

Experimentally, one relies on a dose test array to see which parameters work best for a specific geometry. Figures 5.2 and 5.3 are two atomic force microscope (AFM) images of PMMA trenches in a dose array configuration on a TiO_2 terminated $SrTiO_3$ substrate and a dose array of aluminum nanowires on a Si substrate.

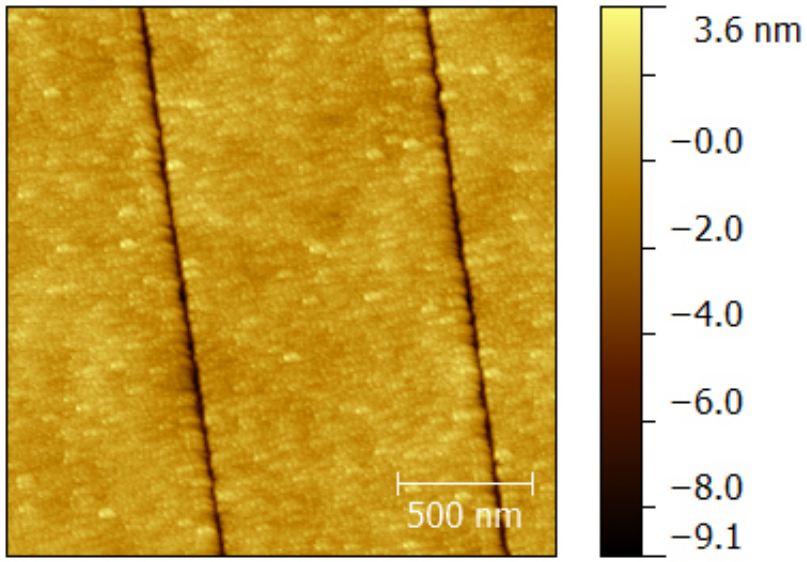

Figure 5.2: An atomic force microscope (AFM) image $SrTiO_3$ dose array of $20nm$ wide trenches formed in PMMA.

Further tuning of a recipe requires the painstaking task of varying one parameter in the whole process and seeing if it gets you what you want.

5.2 Process Recipes

There are some general things to keep in mind while fabricating these devices. For one thing, one should always use dedicated glassware. In addition, one must always have dedicated beakers for each solvent and developer solution. While this may appear paranoid, it will help avoid comprimising process by cross contamination and save time by being organized.

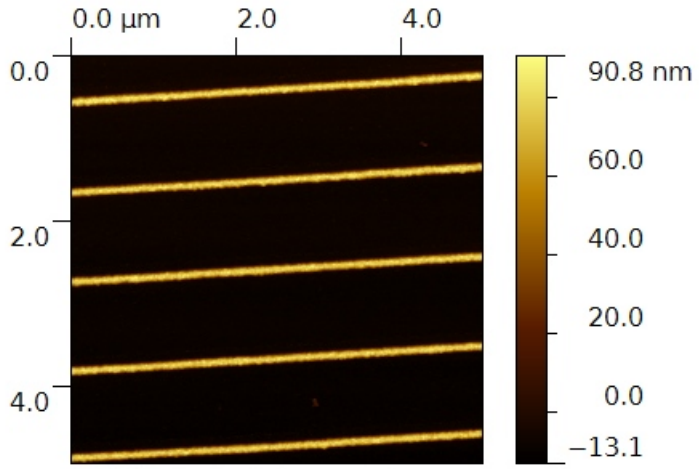

Figure 5.3: An AFM image of 100nm wide and 95nm thick Al nanowires in a dose array configuration.

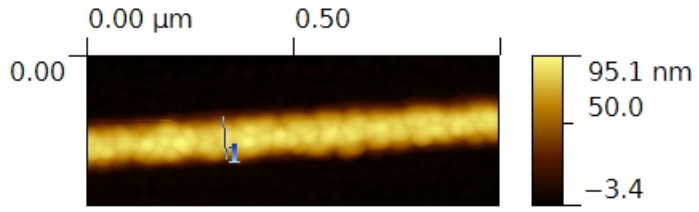

Figure 5.4: Close up image of one of the Al nanowires in Figure 5.3.

When dealing with resists, one should use your own dedicated resist dilutions, make sure to blow off pipettes with compressed N_2 gas prior to use, and use dedicated glassware when diluting stock resist.

With this in mind, the following is the general recipe for patterning contacts and a narrow channel on $SrTiO_3$. Prior to doing any EBL on a $SrTiO_3$ substrate, one has to start with a TiO_2 terminated surface of a $SrTiO_3$ substrate. This is the main method for forming atomically flat surfaces on $SrTiO_3$ substrates. The general idea is that Buffered Oxide Etch (BOE), an aqueous solution of 10 parts 40 percent NH_4: 1 part 49 percent HF, etches the basic SrO portion of $SrTiO_3$'s unit cell. Soaking for

an extended period of time in DI H_2O prior to the BOE dip assists etching this layer by forming additional basic $Sr(OH)_2$ complexes at the $SrTiO_3$ surface.[39]

The annealing step causes atoms to diffuse, and upon cooling relax back to the ground state surface configuration. This ground state surface configuration is the step and terrace structure. Each step is a unit cell high, $0.4nm$, and the terrace width is related to the initial crystal grower's miscut by $\theta_{miscut} = step\ height\ /\ terrace\ width.$ Figure 5.5 shows the step and terrace structure.

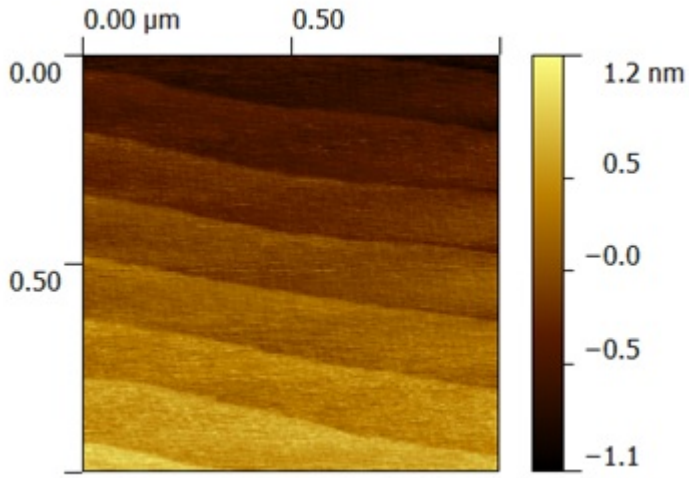

Figure 5.5: AFM image of a TiO_2 terminated (100) $SrTiO_3$ substrate.

Table 5.1 outlines the detailed steps that are required to achieve the step and terrace structure shown in Figure 5.5.

The most important part of this process is to be careful while handling BOE. Next one needs to pattern source, drain, and gate electrodes onto the $SrTiO_3$ substrate. Table 5.2 summarizes the detailed steps required for this.

Steps 4 and 5 are necessary for EBL patterning of $SrTiO_3$ substrates. Otherwise, charge will build up on the surface of the substrate and inadvertently deflect the beam if this is not done. Thus, using a water soluble conducting polymer, aquaSave, available from Mitsubishi Rayon or a water soluble homebrewed dielectric polymer (PSS polymer and TritonX 100 surfactant solution), also known as "Fake" E-Spacer in the MNC, plus Au on top of the resist is necessary.

1	Obtain pristine (100) $SrTiO_3$ substrates (Princeton Sci. Corp. or MTI).
2	Load substrates into Teflon holder.
3	Soak substrates in acetone, methanol, isopropanol for 2 minutes each.
4	Blow dry substrates with compressed N_2.
5	Sonicate (Bay 2 sonicator built into wet bench) substrates for 20 minutes in DI water at 50W sonication power.
6	Soak substrates in (10:1) Buffered Oxide Etch (BOE) for 20 seconds - pour BOE into a Nalgene polypropylene container. Don't be a yutz and pour BOE into a glass beaker!
7	Dip substrates in DI water baths (3 different baths in succession).
8	Rinse holder and substrates with DI water gun. Blow dry with N_2.
9	Flow O_2 gas (medical grade, 300 cc/min) and turn on O_3 generator, set to 3 ticks CCW.
10	Purge lines and glass tube for 10 minutes at room temperature. Always neutralize O_3 output in tap water.
11	Load substrates, face down, into ceramic boat.
12	Load boat into glass tube and into tube furnace.
13	Flow O_2 gas (300 cc/min) and turn on O_3 generator, set to 3 ticks CCW.
14	Anneal substrates for 60 minutes at $950°C$.
15	Allow furnace to cool to room temperature. Continue to flow O_2/O_3 to assist cooling, typically 6 hours does the trick.
16	AFM substrates and look for step and terrace structure.
17	Repeat process if it did not work the first time.

Table 5.1: Process recipe for obtaining the step and terrace structure on $SrTiO_3$'s surface.

The process outlined in Table 5.2 is an unaligned exposure. Therefore, during the substrate leveling procedure prior to loading and exposing one's substrate (Step 9), the center of the exposure field, whose (x, y) coordinates are referenced from the Faraday cup on the substrate holder, is at the center of the $SrTiO_3$ substrate.

Since the thickness of the PMMA layer is $> 1\mu m$, one might also need to repeat steps 11 and 12 but developing for additional 1 minute intervals in MIBK:IPA 1:3. After this, one needs to ion mill and evaporate the contacts and alignment marks following the recipe in Table 5.3.

Ion milling with Ar^+ is necessary to create a region of oxygen vacancies (regions of metallic n-type $SrTiO_3$) so as to facilitate Ohmic contact to the $SrTiO_3$ substrate

1	Clean TiO_2 terminated (100) $SrTiO_3$ substrate in acetone, methanol, isopropanol for 2 minutes each.
2	Dehydrate bake for 5 minutes at $180°C$.
3	Spin coat PMMA A9, 4000 rpm for 45 seconds.
4	Bake for 20 minutes at $180°C$.
5	Spin coat aquaSAVE or "Fake" E-Spacer, 3000 rpm, 45 seconds.
6	If using aquaSAVE, bake for 5 minutes at $90°C$ then jump to step 9.
7	If using "Fake" E-Spacer, bake for 3 minutes at $90°C$.
8	Sputter 2-3nm (15 second sputter time) of Au in Cressington sputter coater.
9	Expose: 800 $\mu C/cm^2$, $I_{beam} = 25nA$.
10	Remove aquaSAVE or E-Spacer/Au stack in DI water for 1.5 minutes.
11	Develop for 3 minutes in MIBK:IPA 1:3.
12	Soak for 1 minute in isopropanol to stop development. Blow dry substrate with N_2.

Table 5.2: Process recipe for patterning source, drain, and gate electrodes on a TiO_2 terminated (100) $SrTiO_3$ substrate.

from the Ti/Au stack.[40] I prefered using electron beam evaporation for the electrodes because the omnidirectional beam made lift-off much easier with a single layer of resist.

The final step is to pattern the narrow channel between source and drain electrodes following the recipe in Table 5.4. This step must pattern openings in the resist for the electrodes for indium dotting needed to make electrical contact to the structure. The side gate was a $500\mu m \times 500\mu m$ situated $\sim 10\mu m$ away from the nanowire. In addition, this step is an aligned write. I used three alignment marks ($20\mu m \times 20\mu m$ Ti/Au squares) at the corners of a $500\mu m \times 500\mu m$ square centered at the nanowire. After this the final product will look like the structure shown in Figure 5.6.

The last step prior to cooling down the device is to indium dot the electrodes to a Quantum Design PPMS puck and to place a $1\mu L$ droplet of the ionic liquid, DEME-TFSI, so as to cover the gate electrode and the narrow channel.

Next, I will outline the EBL recipe for making superconducting aluminum nanowires as seen in Table 5.5. First, the photolithography step to deposit Ti/Au contacts and alignment marks are fabricated from a recipe described elsewhere.[71] The substrates used were commercially available p-type Si wafers coated with $\sim 100nm$ of SiO_2. This

1	Argon ion mill with a kinetic energy of 300V for 20 minutes (fast etch recipe). Etch depth =70 nm.
2	Deposite Ti/Au for the electrodes in the CHA electron beam evaporator. Rate (for both): $2\mathring{A}/s$ Thickness: Ti: 35nm/Au: 135 nm.
3	Lift-off resist in acetone. Clean patterned substrate with methanol and isopropanol. Blow dry with N_2.

Table 5.3: Process recipe for argon ion milling, electrode and alignment mark fabrication.

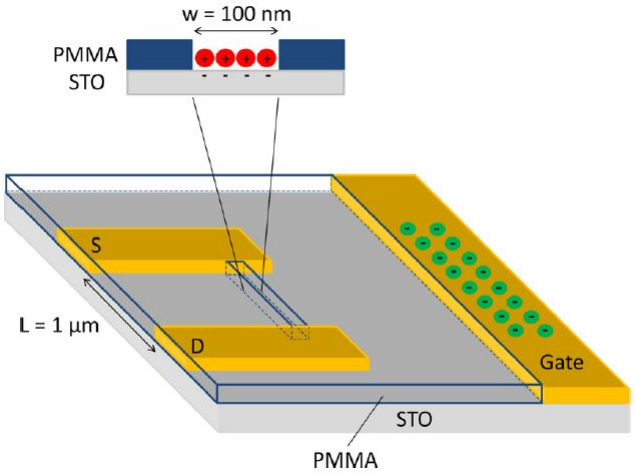

Figure 5.6: STO device.

EBL recipe was a bilayer resist recipe which is PMMA/PMGI.

The PMGI layer can be finicky. At times, the PMGI bake will not go well and there will be splotches and inconsistent height variations in the resist everywhere for whatever reason. The easy solution is to remove the PMGI layer in an N-Methyl-2-pyrrolidone (NMP) soak for 30 minutes at room temperate and repeat steps 1-5. In addition, there were times where I undercut an additional 10-20 seconds after step 14. These are process variations and are expected.

After patterning, I would then transfer my substrates to our custom, dedicated aluminum evaporator. Before giving you the recipe, I will discuss the schematics and other important details for running this system. Figure 5.7 is a picture of the homebuilt

1	Clean patterned substrate in acetone, methanol, isopropanol (AMI) for 2 minutes each.
2	Dehydrate bake for 5 minutes at $180°C$.
3	Spin coat PMMA A4, 4000 rpm for 45 seconds.
4	Bake for 20 minutes at $180°C$.
5	Spin coat "Fake" E-Spacer, 3000 rpm for 45 seconds.
6	Baked for 1 minute at $90°C$.
7	Sputter 2-3nm (15 second sputter time) of Au in Cressington sputter coater.
8	Expose: 800 $\mu C/cm^2$, $I_{beam} = 10nA$.
9	Remove "Fake" E-Spacer/Au stack in DI water for 1 minute.
10	Develop for 1 minute in MIBK:IPA 1:3.
11	Soak for 1 minute in isopropanol to stop development. Blow dry with N_2.

Table 5.4: Process recipe for patterning the narrow channel between source and drain electrodes.

evaporator.

The Al evaporator is divided into two separate vacuum chambers, the main chamber and the load lock via a gate valve. A turbo pump backed with a rotary vane pump pumps each chamber. The base pressure in the main chamber, while the effusion cell idled, is read with an ion gauge and is about $1 \times 10^{-8} Torr$.

The evaporation source is a Veeco cold-lip effusion cell with a 40 cubic centimeter double wall pyrolytic boron nitride crucible. The effusion cell is located at the bottom of the main chamber. The effusion cell is surrounded by a water cooled shroud. A Micristar PID controller maintains the temperature.

The effusion cell was kept at $T = 700°C$, and under high vacuum while not in use. The reason for this is to prevent Al from freezing ($T_{melt} = 660°C$), and possibly cracking the crucible, and destroying an expensive effusion cell. The source material is a collection of 99.999% Al pellets available from Kurt J. Lesker. The evaporation rates are measured with an Inficon quartz crystal microbalance calibrated with the appropriate tooling factor.

The load lock is where the liquid N_2 cooled feedthrough and sample holder are located. All Al films measured were quench deposited. The sample holder block is

1	Clean substrate in acetone, methanol, isopropanol for 3 minutes each.
2	Dehydrate bake for 5 minutes at $180°C$.
3	Spin coat PMGI SF9, 4000 rpm for 60 seconds.
4	Bake for 10 minutes at $265°C$.
5	Check PMGI bake under microscope.
6	Spin coat PMMA C2, 4000 rpm for 60 seconds.
7	Bake for 5 minutes at $180°C$ in the IR heater.
8	Expose: 1000 $\mu C/cm^2$, $I_{beam} = 10nA$.
9	Develop PMMA: 1 minute in MIBK:IPA (1:3).
10	Soak for 1 minute in isopropanol to stop development. Blow dry with N_2.
11	Examine imaging layer under microscope.
12	Develop PMGI: 1 minute in CD-26:DI water (3:2).
13	Soak for 1 minute in DI water to stop development. Blow dry with N_2.
14	Examine undercut layer under microscope.

Table 5.5: Process recipe for fabricating aluminum nanowires.

an oxygen free high thermal conductivity copper cylinder, 2 inches in diameter and 1 inch long, with stainless steel liquid N_2 supply lines soldered into the top. Samples remained fastened in the grooves and clipped to the copper block with screws. The interface between the sample holder and copper block is coated with Apiezon N grease to ensure good thermal contact between the components. The sample holder is 24 inches above the lip of the effusion cell and thus well within the Knudsen limit during evaporations when $p_{main\ chamber} \sim 1 \times 10^{-7}\, Torr$. The recipe for loading the evaporator and evaporating Al is in Table 5.6.

The second to last step in making these nanowires prior to measuring them is the lift-off step. One should do lift-off in NMP heated on a wetbench hotplate to $160°C$ for 30 minutes to an hour. While doing this make sure to put a lid on top of the beaker to collect the flammable NMP vapors. One of the completed devices is seen in the SEM micrograph Figure 5.8.

The last step is to mount the device on a Quantum Designs ^3He puck with GE varnish and wirebond to the puck. While wirebonding, one should make sure all the pads on the puck are at the same electrical potential as the wirebonder. This helps prevent

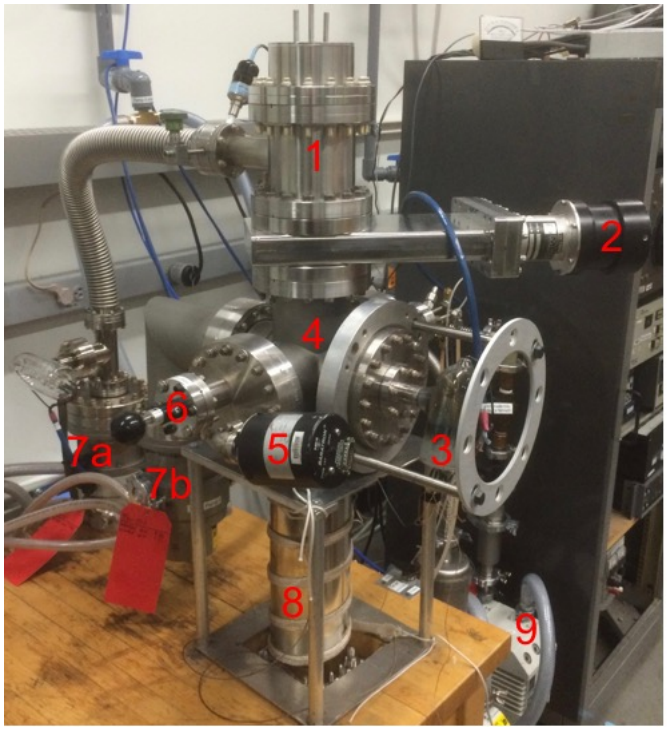

1	Load lock
2	Gate valve
3	Ion gauge – main chamber
4	Main chamber
5	Capacitance manometer
6	Shutter
7a,b	Turbo pump – load lock, main chamber
8	Effusion cell embedded in shroud
9	Rotary vane pump

Figure 5.7: A picture and diagram of the aluminum evaporator.

nanowires from being damaged from sudden discharges. In the next section, I will focus on the measurement apparatus and gating procedure for ionic liquid experiments.

5.3 Experimental Methods: Cryostat, Measurement Electronics, and the Ionic Liquid Gating Procedure

In this section, I will discuss the cryostat used for all of the measurements, a Quantum Design Physical Property Measurement System (PPMS) with ^3He refrigerator insert, the measurement electronics, and the electric double layer transistor.

The Quantum Design PPMS is a ^4He cooled cryostat equipped with a 9T superconducting magnet composed of NbTi wires coated with copper. The system maintains temperature control by pumping on a bath of ^4He and uses the enthalpy of the expanding gas in the cooling annulus to cool the sample space. The sample is thermally linked to the walls of the sample space via ^4He exchange gas. Figure 5.9 is a detailed

1	Vent load lock (LL) making sure to bleed N_2 gas ($< 3psi$) into load lock.
2	Unbolt CF flange and affix samples to holder.
3	Replace copper gasket and seal load lock with star pattern.
4	Purge and seal 3 times by backfilling LL with N_2 gas and roughing out with the rotary vane pump.
5	When $P < 100$ mTorr, turn on turbo pump and pump overnight.
6	After pumping overnight, $P_{LL} \sim 10^{-7} Torr$. Begin ramp up effusion cell at $1°C/min$.
7	Affix rubber liquid N_2 transfer lines to the feedthrough, pipe output liquid N_2 to a styrofoam container.
8	Once $T_{cell} = 830°C$ begin flowing liquid N_2.
9	When $T_{cell} = 855°C$, wait for 5 minutes then measure rate with QCM. $\bar{R} \sim 2\mathring{A}/s$, $P_{mainchamber} \sim 3 \times 10^{-7}$ Torr.
10	Slowly open the gate valve between chambers, equilibrate for 5 min.
11	Open shutter and evaporate! Monitor $\bar{R}$ while doing this.
12	When done, close shutter, QCM shutter, and gate valve.
13	Cease liquid N_2 cooling.
14	Ramp effusion cell back to $700°C$ at $1°C/min$.
15	Allow for feedthrough to warm back up to room temperature naturally (half a day at most). Do not warm with the heat gun, as heat treatement will soldered joints.
16	Vent with N_2 gas.

Table 5.6: Procedure for using our dedicated evaporator.

schematic of the PPMS insert. It is shielded from room temperature by various layers starting with a liquid N_2 jacket, superinsulation, and a liquid ^4He jacket. One can maintain a constant temperature between $T = 1.8K$ and $T = 350K$ with cooling and warming rates between $0.5K/min$ and $20K/min$. The PPMS controls temperature to better than $3mK$. When using the superconducting magnet, it is always a good idea to ramp up the field to 9T and oscillate the magnet down to zero field prior to measurements. This helps avoid trapped flux which will produce a small and constant magnetic field offset from the nominal field reading. The other trick to avoid spurious offsets is to perform measurements (say $R(H)$) at positive and negative magnetic field values. By examining the symmetry of $R(H)$ about the R axis, one can determine the constant offset. Figure 5.9 is a schematic of the PPMS.

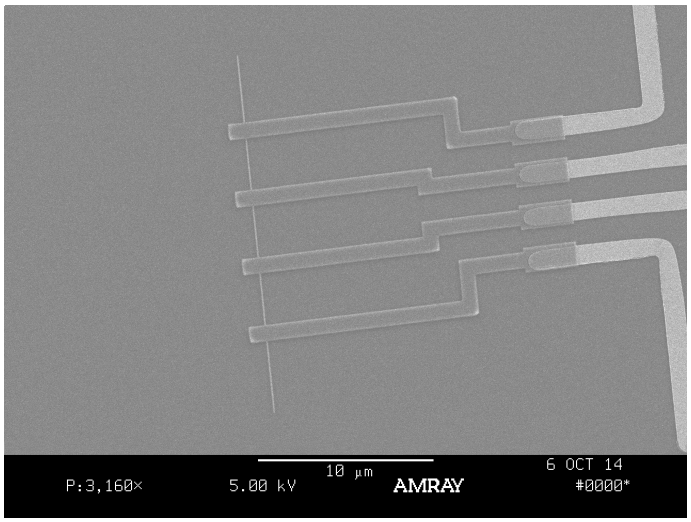

Figure 5.8: An Al nanowire device.

Other than making sure that the PPMS puck is inserted correctly, PPMS operation is very straightforward. The PPMS is controlled by a dedicated computer, the Model 6000, which is in turn controlled by a PC using Quantum Design's proprietary software, MultiVu. Data aquisition was done using Field Sweep.vi, a LabView based program written in house by Chad Geppart.

For the superconducting nanowire project, the temperature range of the PPMS could be extended using a ^3He refrigerator insert. This system has a typical base temperature of $450mK$ in circulation mode. In one shot mode, one could get below $T = 400mK$ for about half an hour. The insert works by flowing ^3He gas through a narrow impedance from a condenser to a pot which cools, by the Joule-Thompson effect, as it passes through the impedance. A turbo pump backed by a diaphragm pump lowers the temperature of the liquid further by pumping on the pot. The pot is thermally linked to a sample puck. The temperature at the sample holder is measured by a calibrated resistance thermometer. Figure 5.10 is a schematic of the ^3He refrigerator. The electrical leads (12 total) down to the sample are twisted pairs to avoid inductive pickup. At most, one can measure two nanowires since 4 of the electrical leads were for a dedicated resistance thermometer. Thus, measurement throughput is the main drawback of this system.

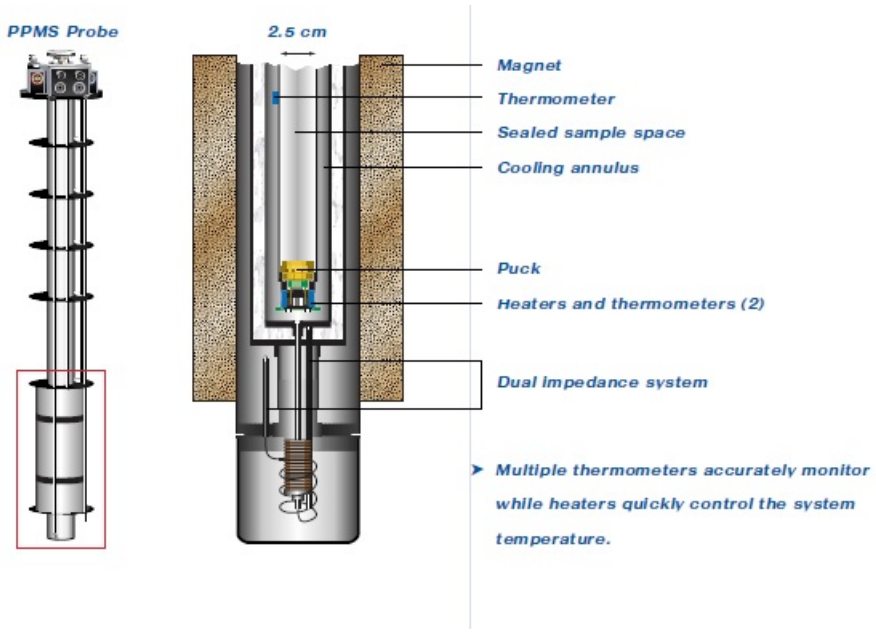

Figure 5.9: The PPMS insert schematic from the Quantum Design brochure.[72]

Prior to cooldown, one needs to clean and reapply Apiezon N grease to the contact fingers and perform a cryoclean of the ^3He gas. The Apiezon N grease is needed to maintain a good thermal link between the probe and the cooling annulus. The probe condenser needs to be at $2K$ since ^3He condenses at a temperature, $T = 3.19K$, and a pressure, $p = 1atm$. Furthermore, cryocleaning with liquid N_2 removes impurities which solidify at $T = 77K$, such as H_2O, N_2, Xe, and CO_2. If one does not do this every time, one may waste an entire day warming back up to cryoclean when the impedance clogs shortly after reaching base temperature.

All measurements were done with external Keithley instrumentation. For the ionic liquid experiment, I used a Keithley Model 487 dc voltage source/picoammeter to measure the $I-V$ characteristics and a Keithley 6517A electrometer to apply the gate voltage and to measure the leakage current. For the superconducting nanowire experiment, I used a Keithley 6220 dc current source and Keithley 2182 nanovoltmeter to measure the resistance of my nanowires. I measured $R(T)$ and $R(H)$ by sourcing $\pm I$ and measuring the voltage drop due to I. Then, I calculated $R = \Delta V/\Delta I = (V_+ - V_-)/(I_+ - I_-)$. Typically, with the background noise levels, one could read resistance values at best

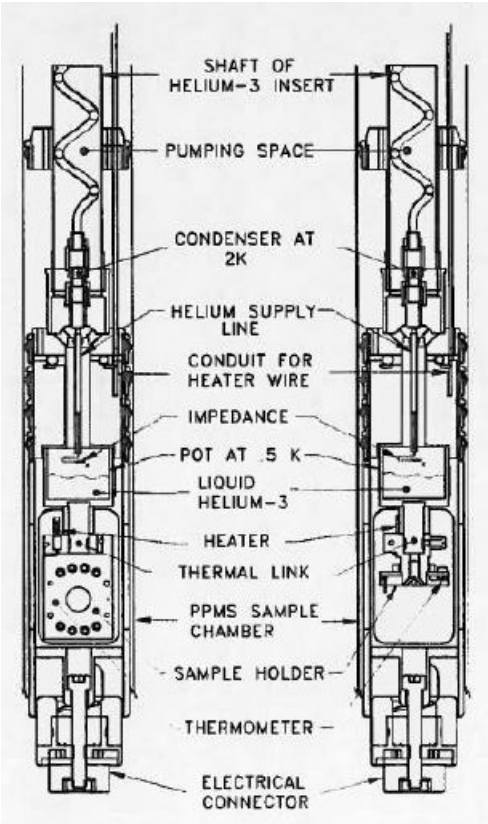

Figure 5.10: A schematic of the ^3He refrigerator insert from the PPMS manual.[72]

down to 0.015Ω.

Lines from the instruments were fed via BNC and Triax cables into a breakout box and electrical switch (Keithley 7001) before going to the sample in the PPMS. This was crucial for the superconducting nanowire project, as I mentioned in the wirebonding step, the nanowires are easily damaged by sudden electrical discharges. Therefore, it was necessary to use the "make before break" methodology while switching between different nanowire contacts. Furthermore, prior to cool down, the Keithley 2182 nanovoltmeter was used to check that the nanowires were continious and not destroyed. The 2182 nanovoltmeter uses a small but finite sensing current to measure voltages, and thus if the voltmeter is reading a small, but finite voltage at room temperature the nanowire is intact.

We now focus on the techniques and procedures using ionic liquid (IL) in gating

experiments. To begin with, an IL is a binary molten salt that is a liquid at room temperature with a nearly zero vapor pressure. Essentially, the Coulomb attraction energy between cation and anions is much less than the thermal energy of ions and thus the salt is prevented from solidifying at room temperature. A common example of an IL is molten table salt, NaCl. When heated up to $T_{melt} = 800°C$, NaCl dissociates into a liquid composed of free Na cations and Cl anions.

The ionic liquid that we used was DEME-TFSI. Its cations and anions are large organic molecules with single $\pm e$ charges located on nitrogen ions as seen in Figure 5.11.

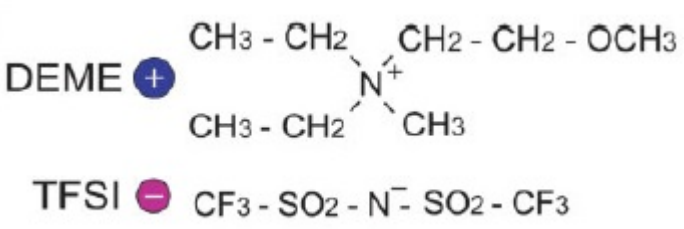

Figure 5.11: Molecular diagrams of DEME-TFSI.[41]

DEME carries the positive charge and TFSI carries the negative charge. Besides being used to manipulate the surface carrier concentration of materials, the more practical use for ILs is in energy storage. For reasons outlined below, ILs form nanoscale capacitors which can store much more charge, at comparable voltages, than traditional capacitors.

The tool used to induce carriers in $SrTiO_3$ is the electric double layer transistor (EDLT). It is a field effect transistor in which the solid gate dielectric has been replaced with an IL. The induced sheet carrier density, n_{2D}, at the surface of a material is related to the applied gate voltage, V_g, and gate capacitance per area, C_g, by

$$n_{2D} = C_g V_g \tag{5.2}$$

Field effect action works by bending electron energy bands above and below the material's Fermi energy, accumulating or depleting carriers depending on the polarity of V_g. This is seen in Figure 5.12 for a traditional metal-oxide-p-type semiconductor field effect transistor (FET).

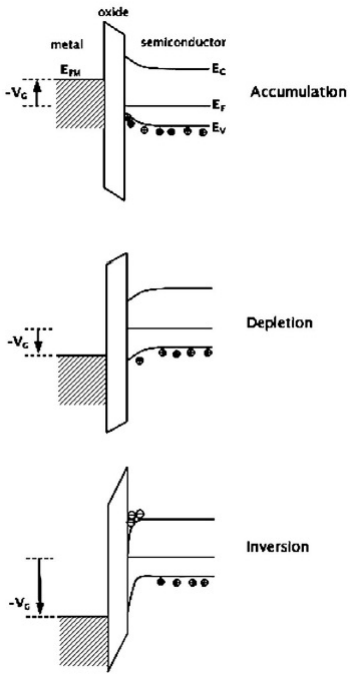

Figure 5.12: Field effect transistor action of a metal-oxide-p-type semiconductor device.[42]

The IL and induced image charge in $SrTiO_3$ form an electric double layer, essentially a nanometer thick parallel plate capacitor. The electric double layer thickness is an order of magnitude smaller than the gate insulator thickness of a solid state FET whose dielectric material is SiO_2. With SiO_2, one is limited by SiO_2's dielectric constant ($\epsilon = 3.9$), dielectric breakdown ($E_b = 10MV/cm$) and significant leakage currents when SiO_2 thickness is $\sim 100\mathring{A}$.[42] This limits the $n_{2D} \sim 10^{11}cm^{-2}$ using SiO_2. But using an IL, the sheet carrier density one can achieve $n_{2D} \sim 10^{14}cm^{-2}$ since $C_g \sim 10\mu F/cm^2$ at $V_g \sim 2V$ at low temperatures.[41] Thus, one can explore more of a material's phase diagram using an EDLT. The other advantage of using an IL is that the leakage currents, below the IL's glass transition temperature $T_{glass} = 190K$, are zero.[41] To use an IL properly, one needs to understand its phase diagram as seen in Figure 5.13.

When applying V_g, one needs to be in the region of the phase diagram such that ions are mobile, but electrochemistry is suppressed. For DEME-TFSI, this region is the

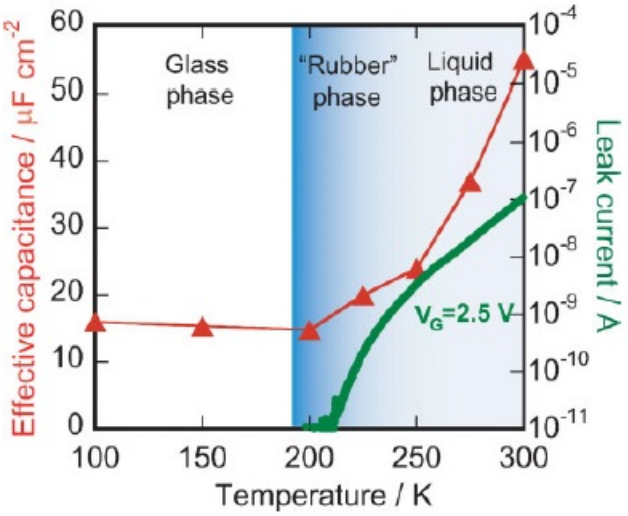

Figure 5.13: High temperature phase diagram of DEME-TFSI.[41]

high temperature part of the "rubber" state. Thus, by applying V_g in the sweet spot region between $230K$ and $240K$, one minimizes electrochemistry while accumulating carriers in the device. In the following measurements, V_g was changed at $240K$ in $0.2V$ increments. At room temperature, DEME-TFSI's electrochemical window is between $V_g = \pm 3V$.

Keeping V_g in this range also suppresses electrochemistry at lower temperatures.[41] Below $T = 220K$, the leakage currents go to zero as seen in Figure 5.13 for $V_g = +2.5V$. In addition, prior cooling down to base temperature and before warming to change V_g, we found it necessary to equilibrate right below T_{glass} at $T = 180K$ and change the warming rate from $1K/min$ to $5K/min$ below and above $T = 180K$ respectively. This helped alleviate electrochemical and mechanical degradation of the PMMA layer.

Chapter 6

Experimental Results and Discussion

In this chapter, I will describe the results of both the ionic liquid gating experiment of $SrTiO_3$ nanowires and of the reentrant superconductivity experiment. The published versions are found in Applied Physics Letters and Physical Review B, respectively.[79, 80]

6.1 Ionic Liquid Gating of $SrTiO_3$ Nanowires: Results

Collective transport through quenched disorder appears as a dynamical phase transition in various physical systems. Sliding charge density waves, fluid flow in porous media, vortex lattices in type-II superconductors, and arrays of quantum dots, all exhibit this behavior.[43, 44, 45, 7] The essential ingredients include an elastic medium subject to a driving force, which in the presence of quenched disorder is pinned into place. Upon increasing the driving force to a critical threshold value, the elastic medium is depinned and propagates. This dynamical phase transition between a static, pinned state and a moving state exhibits scaling behavior of observable quantities such as the $I - V$ characteristic.

The original goal of this experiment was to induce a low carrier density metallic state in $SrTiO_3$ by electrostatic gating using an ionic liquid (IL), so that the Fermi wavelength, λ_F, of the electrons in the transverse directions would be larger that the width of the

channel and thickness of the electric double layer. In other words, the electrons in the nanowire region would be confined by the electrostatic potential in the transverse directions and thus would be effectively a one-dimensional metal. By examining the $I-V$ characteristics, we could in principle determine whether the nanowire channel of IL gated $SrTiO_3$ exhibited features usually attributed to Tomonaga-Luttinger liquid (TLL) behavior.[75, 76] TLL behavior leads to power law $I-V$ characteristics and differential conductances vs. temperature and voltage and is seen in a host of metallic one-dimensional systems.[46, 47, 48, 49, 50] Although we have not observed power law $I-V$ characteristics indicative of TLL behavior, we have observed $I-V$ characteristics indicating a dynamical phase transition created by inhomogeneous IL gating at low gate voltages (V_G) and diffusive quasi-1D transport at high V_G. Understanding inhomogeneous IL gating is relevant for interpreting IL gating experiments of both nanostructures and 2D structures in the low carrier density regime.[51]

As a reminder, the device structure and geometry used in this experiment is seen below in Figure. 6.1.

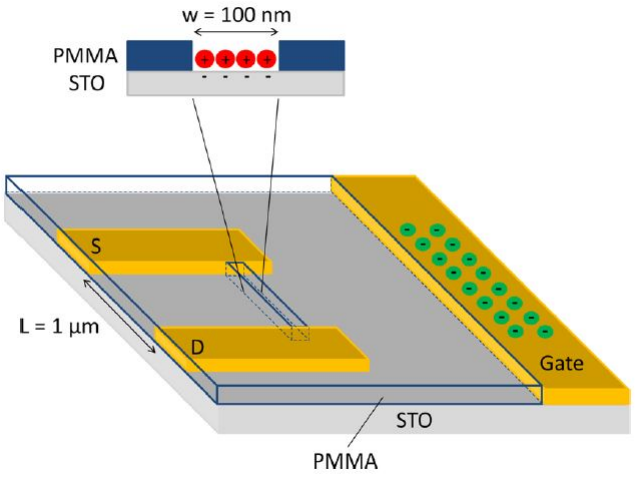

Figure 6.1: STO device.

By following the experimental prescription in the previous chapter, we observed the following temperature dependence of the $I-V$ characteristic as seen below in Figure 6.2.

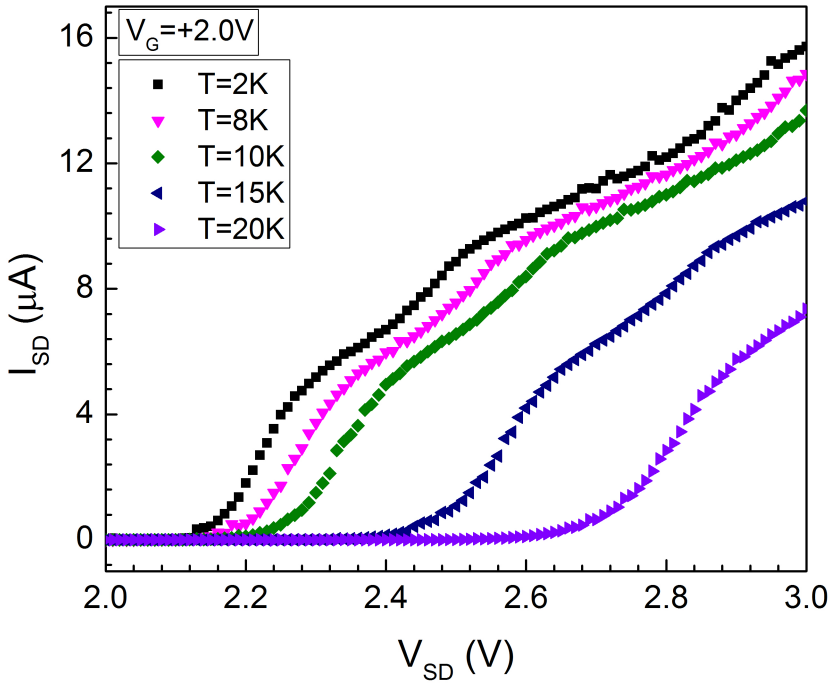

Figure 6.2: Temperature dependence of the $I-V$ characteristic of a $SrTiO_3$ channel with oscillations above V_T. The gate voltage $V_G = +2.0V$.

These $I-V$ characteristics had a striking similarity to Coulomb oscillations as discussed in Chapter 2.1. However, the threshold voltage, V_T, was too large for the gated channel to be behaving as a single quantum dot in the Coulomb Blockade regime. Thus, due to the large V_T, we initially believed that the observed $I-V$ characteristic was due to the depinning of a charge density wave (CDW) formed in the narrow channel.[52] However, CDW formation requires the perfect nesting of the Fermi surface at $q = 2k_F$ which does not occur in Si or STO.[52] It is interesting to note that the earliest Coulomb Blockade measurements on narrow Si inversion layers were explained in terms of CDW/Wigner crystal formation.[53]

Figure 6.2 shows for $V_G = +2.0V$ the $I-V$ characteristic measured at increasing temperatures. A positive $V_G = +2.0V$ in an EDLT induces electrons in the $SrTiO_3$. The V_{SD} step size is $10mV$. As one can see, there is a threshold voltage, V_T observed in each

sweep such that $I_{SD} = 0$ for $V_{SD} \leq V_T$ and $I_{SD} > 0$ for $V_{SD} > V_T$. The temperature dependence of V_T is shown in Figure 6.3 and 6.4. Between $2K \leq T \leq 10K$, V_T is nearly constant. However, upon increasing the temperature V_T also increases.

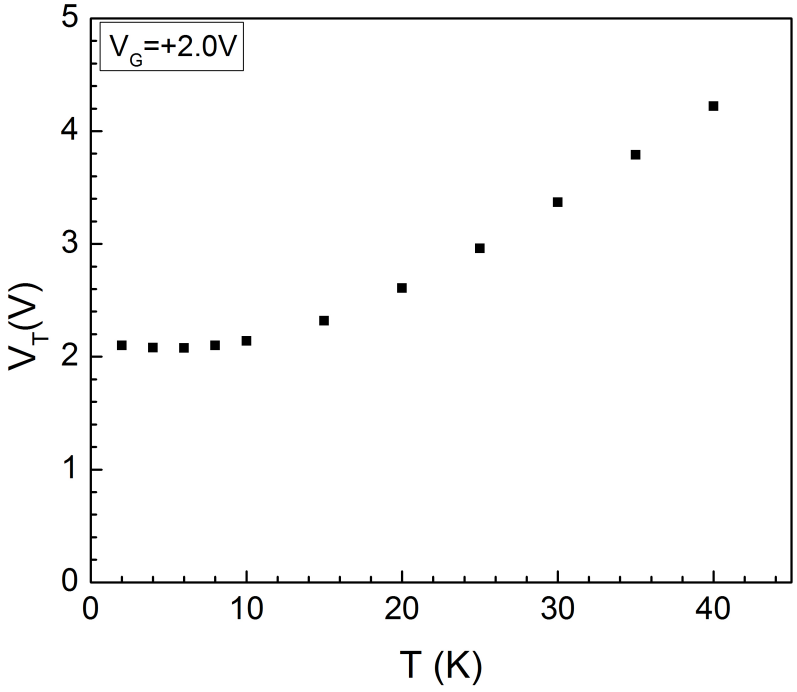

Figure 6.3: Temperature dependence of V_T at $V_G = +2.0V$.

For $V_{SD} > V_T$, I_{SD} increases as a power law. For $+1.8V \leq V_G \leq +2.6V$, similiar behavior in the $I - V$ characteristic occurs with $V_T \geq 1V$ and I_{SD} oscillations occur at higher V_{SD}.

Upon increasing V_G to $V_G = +2.8V$, V_T shrinks by an order of magnitude as seen in Figure 6.4. The temperature dependence of V_T follows the same behavior as seen for lower values of V_G. As seen in Figure 6.5, oscillations in I_{SD} disappear for all temperatures and the $I - V$ characteristic is linear above V_T.

For $V_G < +2.8V$, the $I - V$ characteristic follows the form given by Middleton and Wingreen (MW) which is

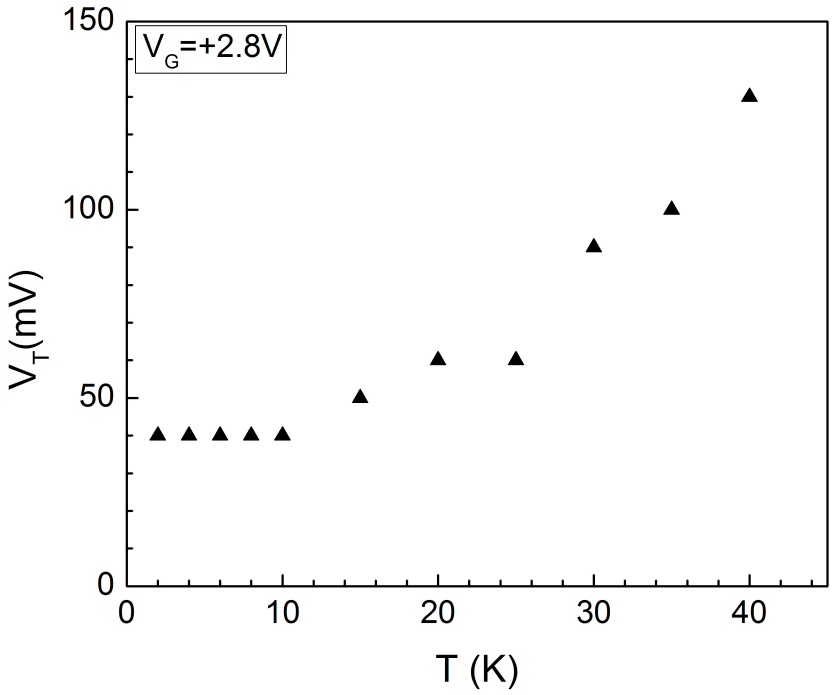

Figure 6.4: Temperature dependence of V_T at $V_G = +2.8V$.

$$I_{sd} \sim (V_{sd}/V_T - 1)^{\zeta} \tag{6.1}$$

Here ζ is the scaling exponent which, analytically, is either $\zeta = 1$ or $\zeta = 5/3$ depending on the dimensionality of the QD array. Charge transport appears to occur by electrons tunneling through an array of quantum dots. For $V_G = +2.8V$, the conductance obeys Landauer's formula for multichannel transport which is

$$G = \frac{e^2}{\pi\hbar} \sum_{ij} T_{ij} \tag{6.2}$$

Here T_{ij} is the transmission coefficient from channel i to channel j. This is demonstrated in Figure 6.6.

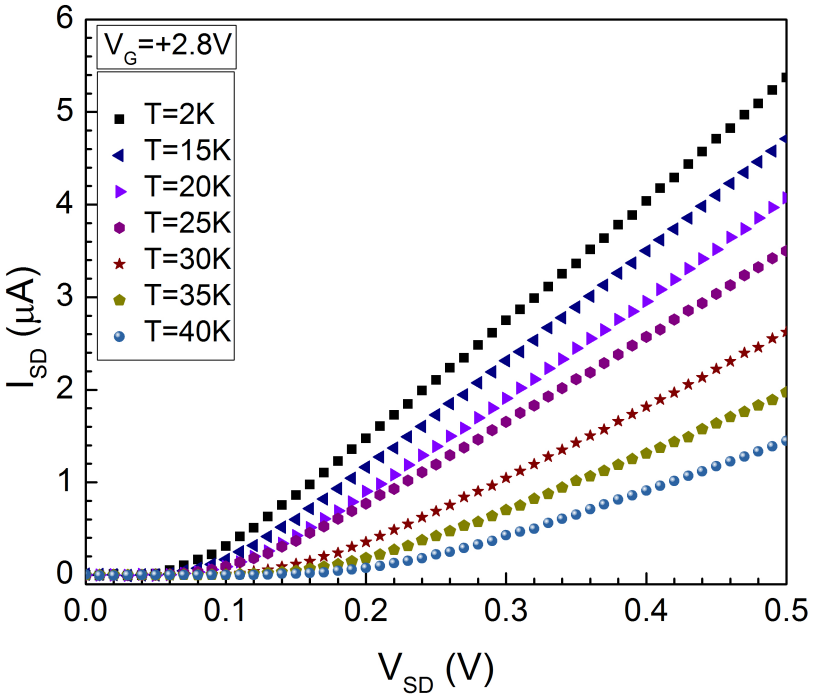

Figure 6.5: Temperature dependence of the $I-V$ at $V_G = +2.8V$.

6.2 Ionic Liquid Gating of $SrTiO_3$ Nanowires: Discussion

The results of a scaling analysis, the values of the extracted exponents, as a function of temperature are seen in Figure 6.7 for $V_G = +2.0V$ and $V_G = +2.2V$.

For each fit, we defined V_T when $I_{SD} < 5nA$ and $dI_{SD}/dV_{SD} > 0$ above this value. We extracted ζ from a linear fit of the log-log plotted $I-V$ in a regime where $10^{-3} \leq (V_{sd}/V_T - 1) \leq 10^{-2}$. ζ increases from 1 at $T = 25K$ to either the 2D numerical (2) or analytical value (5/3) for ζ at lowest temperatures.

In Figure 6.7, at $T = 25K$, $\zeta_{+2.0V} = 1.06 \pm 0.09$ and $\zeta_{+2.2V} = 0.96 \pm 0.07$ suggesting that the tunneling path is along a 1D array for both V_G. Upon decreasing to $T = 2K$, we measured $\zeta_{+2.0V} = 1.60 \pm 0.15$ and $\zeta_{+2.2V} = 2.13 \pm 0.10$. These values are in close agreement with theoretical and numerical values for 2D arrays mentioned before.[7] This suggests that the gated region behaves as an array which exhibits a dimensional

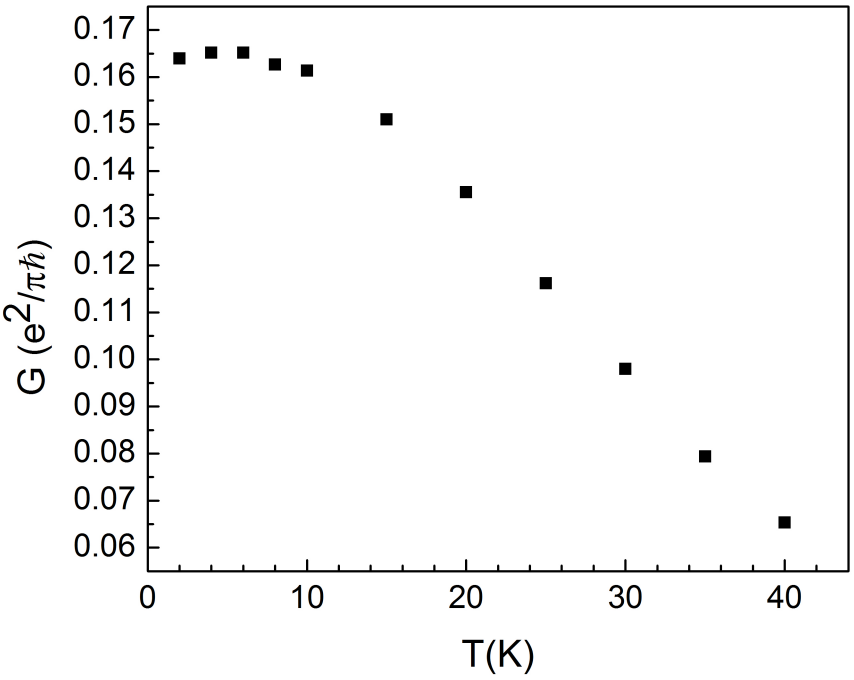

Figure 6.6: Conductance as a function of temperature for $V_G = +2.8V$.

crossover from 1D behavior to 2D behavior at low temperatures.

The physical mechanism for this temperature driven 1D to 2D transition is unclear. Previous studies on metal nanoparticles suggest that structural disorder and large voids in an array network topology can drive a transition between measured ζ values.[28, 29] Arrays with large voids can have 1D bottlenecks linking neighboring 2D array regions with V_T distributed over a range. At low $(V_{sd}/V_T - 1)$, $\zeta = 1$ but when all the 1D bottlenecks are filled ζ can approach a 2D value. However, this bottleneck transition is tuned by $(V_{sd}/V_T - 1)$ and not by the temperature.

The tentative argument for observing quantum dot array-like behavior and quasi-1D nanowire transport is as follows. To begin, the accumulation layer thickness d must be of the order of $1nm \leq d \leq 10nm$.[64] At low $V_G < +2.8V$, the IL induces electrons inhomogenously throughout the narrow channel. We treat each accumulated region underneath a DEME cation as a normal metal island with islands separated from one

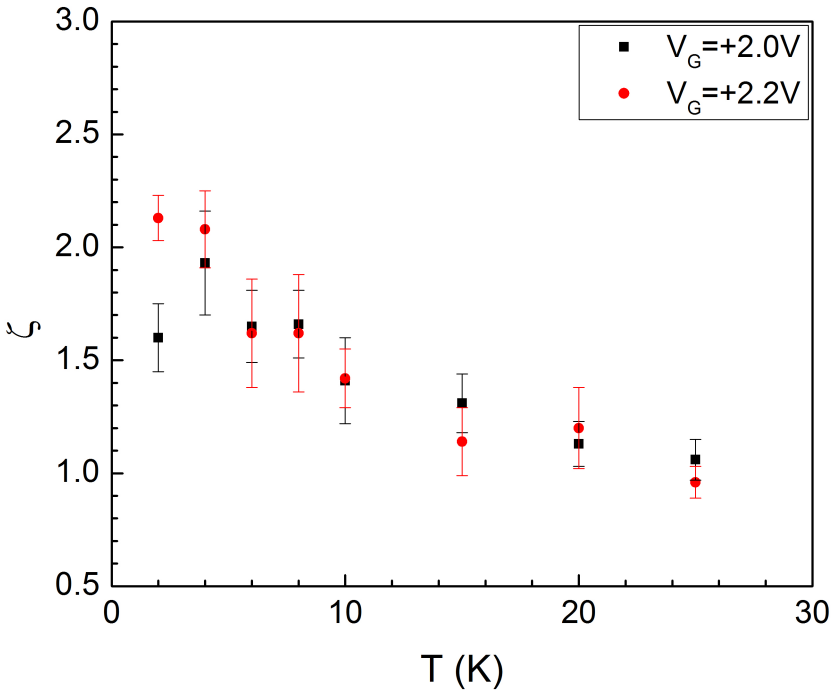

Figure 6.7: Temperature dependence of ζ.

another by insulating $SrTiO_3$. Although the exact size of the quantum dot is not known, we estimate that the size of the quantum dot (R) to be of the order of the diameter of the DEME cation ($D \sim 1nm$).

For this to be valid, the Coulomb Blockade conditions must be satisfied at the lowest temperatures. If a single quantum dot in the array is the size of $R = 1nm$ and with a dielectric constant of $\epsilon \sim 10^3$, the charging energy of the dot (E_C) will be $E_C \sim 20K$ assuming a spherical geometry with $C = 4\pi\epsilon_0\epsilon R$. The dielectric constant of $SrTiO_3$ is highly temperature and electric field dependent. The presence of large electric fields due to both the DEME cations ($\sim 1MV/cm$) and the dc biases ($\sim 10kV/cm$) of the IV characteristic sweeps will reduce the low temperature value of the dielectric constant by an order of magnitude from $\epsilon_{E\geq 0} \sim 10^4$ to $\epsilon_{E\gg 0} \sim 10^3$ or more, depending on the sample.[54, 55] Although, recent work examining hopping conduction in IL gated p-type Silicon shows that the decay length of localized hole wavefunctions is $a = 8.3nm$.[51] In

addition, $R_T = dV/dI$ at $T = 2K$ above V_T which increases with increasing temperature. This indicates that the tunneling resistance requirement is also satisfied at lowest temperatures.

Tuning the Fermi wavelength, λ_F, by changing V_G brings about a transition between regimes. We assume that as we increment from a low V_G regime to a high V_G regime, we push the narrow channel into the metallic regime. This typically occurs when $n_{2D} \sim 10^{13} cm^{-2}$, which is of the order of magnitude to induce metallic behavior in IL gated STO.[77, 78] Provided $n_{2D} \sim 10^{12} cm^{-2}$ at low V_G, $R < \lambda_F \simeq 25nm$. When $V_G = +2.8V$, a sufficient number of carriers populate the narrow channel to form nearly homogeneous metallic paths between the source and drain electrodes. Now $n_{2D} \sim 10^{13} cm^{-2}$ at high V_G, $\lambda_F \simeq 8nm$ in which $\lambda_F \sim R < L$. Here the device is in the quasi-1D regime where multiple conducting channels populate the patterned narrow channel.

Integrated leakage currents as a function of time, computed while changing V_G at $T = 240K$, did not provide a reliable estimate on the accumulated charge. Since the $I - V$ characteristic clearly does not exhibit Ohmic behavior as seen in Fig. 6.2, we are in a regime where inhomogeneous IL gating dominates. Furthermore, previous studies on larger IL gated STO devices showed that at low V_G, the $I-V$ characteristic exhibited a voltage threshold with power law conduction above V_T.[78]

As seen in Figure 6.3 and 6.4, the temperature dependence of V_T appears to be related to the inverse of the temperature dependent dielectric constant of $SrTiO_3$. The bulk dielectric constant of $SrTiO_3$ decreases as a power law below 120K as[55]

$$\epsilon(T) \sim (T - T_C)^{-(1.4 \pm 0.2)} \tag{6.3}$$

with $T_C < 10K$.

We measured a fractional power law in the temperature dependence of V_T for $10K < T < 40K$ with the exponents equaling $T^{0.62 \pm 0.04}$, $T^{0.96 \pm 0.16}$ at $V_G = +2.0V$ and $+2.8V$ respectively. Assuming the threshold electric field is simply scaled by $1/\epsilon(T)$, deviations between the bulk value exponent and our measured values could be caused by the microscopic variation of the electric field strength of the DEME cations and source-drain bias throughout the channel. Below $T = 10K$, V_T varies slowly down to $T = 2K$ at each V_G as does the dielectric constant of $SrTiO_3$.

Furthermore, following from the MW result for the long screening length V_T, we can estimate V_T from theory. The functional form for V_T in this case is

$$V_T = \frac{Ne}{C} \tag{6.4}$$

Here N is the number of quantum dots in the array, e the electron charge, and C the self-capacitance of the quantum dot. If we take the linear size of the array to be $N = 1000$ at $T = 2K$, or equivalently the shortest path of quantum dots of size $R = 1nm$ between the source and drain electrodes, we find that $V_T \simeq 1.6V$ which is nearly the measured V_T in the low temperature regime of Figure 6.3.

MW's result for V_T also scales with the inverse of STOs dielectric constant which can qualitatively account for the temperature dependence in Figure 6.3. The assumptions of the order of magnitude of N, R, and C are consistent within the MW framework. A large screening length may induce hysteretic behavior in the array. Although hysteresis was not apparent in our measurements, it can be realized at lower temperatures for a 2D array.[26]

As we increase V_G, as seen in Figure 6.5, to $+2.8V$, the narrow channel acts as a quasi-1D wire. It is likely that at $V_G = +2.8V$ we enter a diffusive transport regime. In addition, incoherent diffusive transport over phase coherent transport is supported by previous measurements of the temperature dependence of the phase coherence length (L_φ) in nanoscale Hall bars of IL gated STO.[56] $L_\varphi = 300nm$ at lowest temperatures and found to decrease linearly with increasing temperature.[56] The conductance (G) of the narrow channel follows Landauer's formula for multichannel transport, Equation 6.2.

Figure 6.6 shows $G(T)$ in units of $e^2/\pi\hbar$ above V_T. $G(T)$ decreases nearly 40 percent from $T = 2K$ to $T = 40K$. Furthermore, $\sum_{ij} |t_{ij}|^2 < 1$ at all temperatures measured, which is also indicative of the sample length being larger than the elastic mean free path indicative of diffusive transport.

In summary, we have measured the $I-V$ characteristics of IL gated STO nanowires as a function of temperature and V_G. Our measurements provide evidence of collective charge transport through the nanowire as exhibited in the critical behavior of the $I-V$ characteristic at low V_G and diffusive quasi-1D transport at high V_G. The tunability between these two unique transport regimes with an IL presents additional progress in

understanding mesoscopic effects in IL gated STO nanostructures.

6.3 Magnetic Field Tuned Reentrant Superconductivity in Aluminum Nanowires: Results

In the present work, we have reported the results of investigations of the out-of-equilibrium behavior of planar nanowires subjected to in-plane H-fields. The in-plane case is different from that of the perpendicular-to-the plane case because of the substantial in-plane enhancement of the critical field of the leads ($H_{c,Leads,||} \approx 450Oe$) relative to the bulk critical field, $H_{c,B,Al} \approx 105Oe$. [11] We found that for in-plane longitudinal H-fields, nanowires respond in a manner similar to previous measurements with perpendicular-to-the-plane H-fields.[34, 35] However for in-plane transverse H-fields, nanowires exhibit unexpectedly abrupt re-entrance to the superconducting state at H-field values corresponding to a single flux quantum for a short wire and fractional flux quantum for a longer wire. We define the flux quantum over an area determined by the product of the distance between the voltage probes and the nanowire thickness. This striking result cannot be explained by the picture proposed for perpendicular-to-the-plane H-field re-entrance.

We first discuss the experiments on samples A and B, which were subjected to in-plane longitudinal H-fields. In Figure 6.8, we show the H-field dependence of $I - V$ characteristic for sample A.

Sample	$L(\mu m)$	$w(nm)$	$t(nm)$	$T_c(K)$	$\xi_{GL}(nm)$	H-dir.
A	2	130	90	1.25	128	Lng.
B	3	130	90	1.23	134	Lng.
C	1.47	105	95	1.22	183	Trn.
D	2.43	105	95	1.23	210	Trn.

Table 6.1: Sample parameters and H-direction. Lng. refers to an in-plane magnetic field, longitudinally along the wire axis. Trn. refers to an in-plane magnetic field, transverse to the wire axis.

For $H \leq 450Oe$, we enhanced superconductivity in the nanowire by applying a H-field after having driven it resistive with current. Currents which would drive the

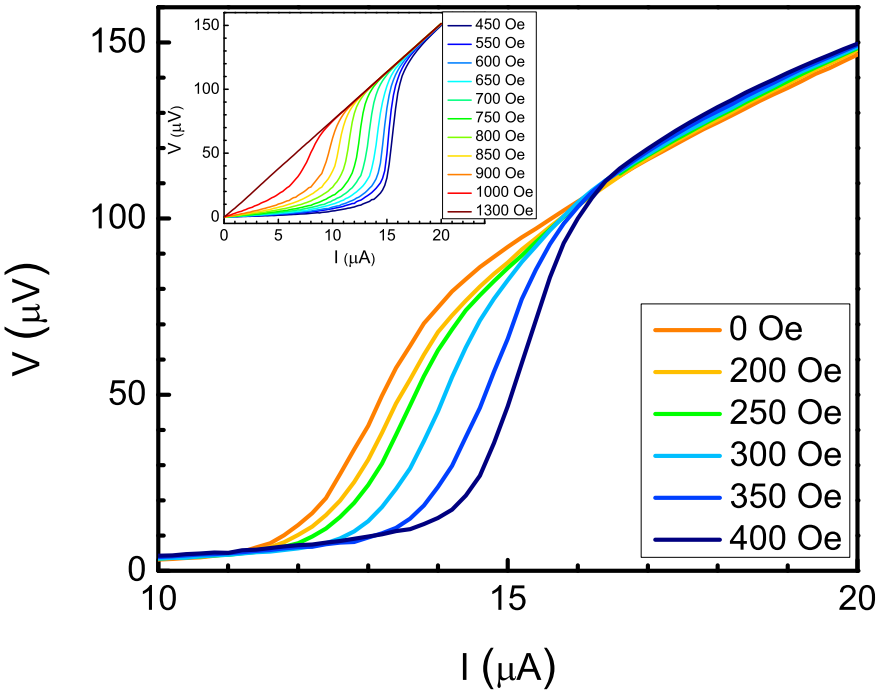

Figure 6.8: $I-V$ characteristic of sample A at $T = 460mK$. The current step size was $200nA$. The H-field was applied in-plane and longitudinally along the nanowire axis. Inset: High H-field regime.

wire into a nonzero voltage state at $H = 0Oe$ produce a near zero voltage drop along the wire. The voltage level prior to the $I-V$ characteristics intersecting at different H-fields is $V_{0,Al} = 93\mu V$. As seen in the inset of Figure 6.8, in the high field regime for $H > 450Oe$, we suppressed superconductivity with higher fields. We drove the nanowire normal for all currents at $H = 1300Oe$.

For the same device, we observed reentrant behavior in $R(H,T)$. As seen in Figure 6.9, which is a plot of $R(T)$ at the different H-fields, we initially drove the nanowire resistive for $H = 0Oe$ using $I = 13\mu A$ at all T. Upon increasing the magnetic field to $H = 400Oe$, the initially broad $R(H = 0Oe, T)$ sharpened and the value of the resistance at the lowest temperatures was $< 1\Omega$. The small nonzero resistance was likely due to residual inelastic scattering of quasiparticles. Furthermore, as seen in the inset of Figure

6.9, larger H-fields completely suppressed superconductivity in the nanowire.

As we increased L, we reduced the reentrant behavior. Longer length nanowires can be in a regime where $L \geq L_{QP}$ and a significant fraction of quasiparticles relax prior to reaching the nanowire/lead interfaces. We believe this to be illustrated by sample B, as shown in Figure 6.10.

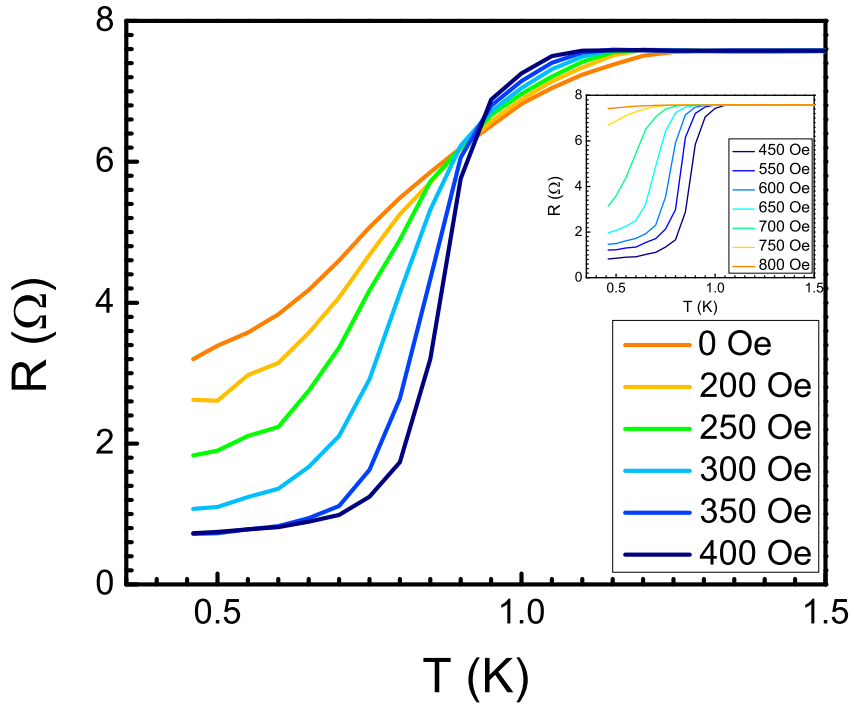

Figure 6.9: $R(T)$ of sample A at different H-fields with $I = 13\mu A$. The H-field was applied in-plane and longitudinally along the nanowire axis. Inset: High H-field regime.

In Figure 6.10, the $I - V$ characteristic of sample B exhibited a reentrant regime between $H = 0Oe$ and $H = 450Oe$. The voltage plateau region occured at $91\mu V$ prior to the $H = 0Oe$ and $H = 450Oe$ $I - V$'s intersecting. Furthermore, as seen in the inset of Figure 6.10, the $R(T)$ of Sample B did not exhibit as pronounced an enhancement of superconductivity as compared to Sample A. We believe this to be a consequence of $L \geq L_{QP}$.

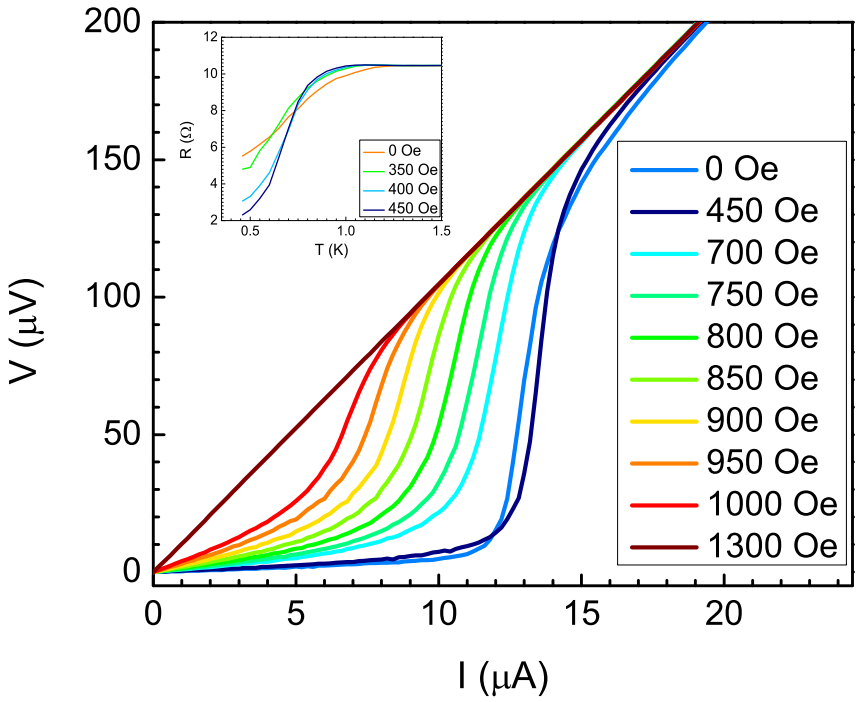

Figure 6.10: $I-V$ characteristic of sample B at $T = 460mK$. The current step size was $200nA$. The H-field was applied in-plane and longitudinally along with nanowire axis. Inset: $R(T)$ in the reentrant regime with $I = 13\mu A$.

We now turn our attention to experiments with H-fields oriented in-plane and transverse to the nanowire axis as measured for samples C and D. In this case, we found novel behavior in both nanowires' response to H-fields. This is most easily seen in the plot of $R(H, T = 450mK)$.

As seen in Figure 6.11, sample C's $R(H, T = 450mK)$ exhibited a flat plateau at low current values. Upon increasing the current, a peak in $R(H)$ near $H = 0Oe$ emerged out of the plateau. Empirically, the $R(H)$ peak could be fit well by a Lorentzian function, Equation 6.5, as seen in Figure 6.12(a).

$$R(H) = R_{offset} + \frac{R_{peak}}{4(H - H_0)^2 + \gamma^2} \tag{6.5}$$

R_{offset} is the resistance offset of the peak, R_{peak} is the value of the peak height, H_0

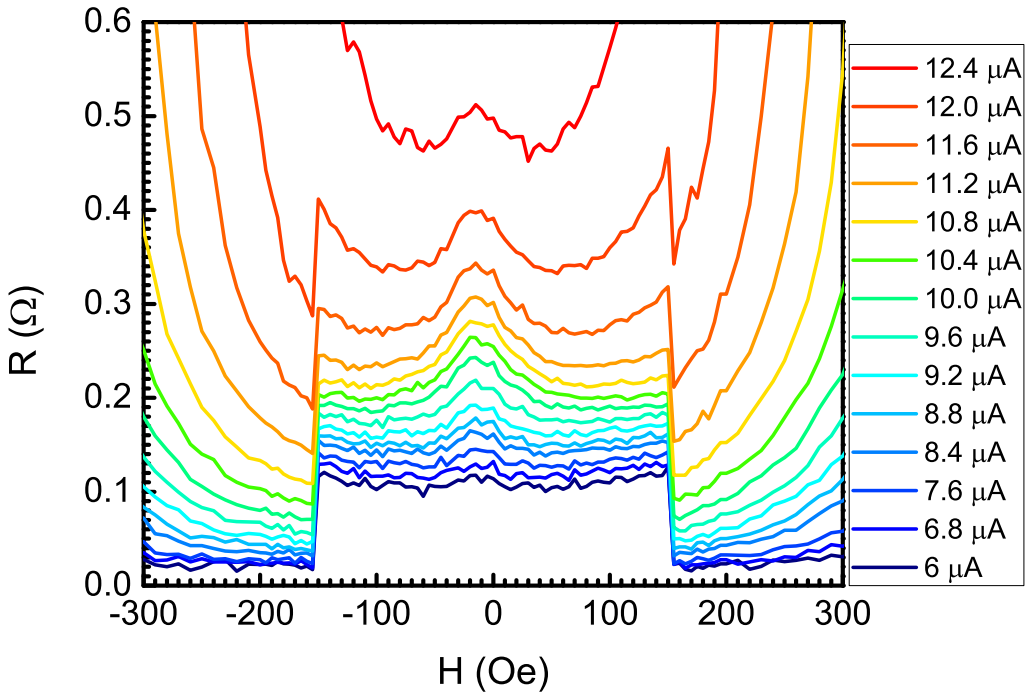

Figure 6.11: $R(H, T = 450mK)$ of sample C. Each color trace corresponds to a different applied current. The H-field was applied in-plane and transverse to the nanowire axis.

is an offset H field and γ is the full width at half maximum (FWHM). The $R(H)$ peak height and the full width at half maximum extracted from the fitting initially grew in height and width as a function of current as seen in Figures 6.12(b) and 6.12(c). Then they both exhibited a maximum as a function of current. The maximum voltage level of the peak occured at $V_{peakmax} \sim 0.33 k_B T_C = 3.5\mu V$ when $I = 11.2\mu A$. This is an order of magnitude less than $V_{0,Al} = 91\mu V$ for Sample C. Above $I = 12.4\mu A$, we drove the nanowire normal and the peak disappeared.

The striking result for this nanowire was that it also exhibited an abrupt reentrance into the superconducting state. This sharp reentrance occured when the H-field applied to the wire corresponded to a single flux quantum. Again, we define the flux quantum over an area determined by the product of the distance between the voltage probes and the nanowire thickness. In other words, $R(H = \pm 155Oe, T = 450mK) = 0\Omega$ occured when $\frac{\Phi}{\Phi_0} = \frac{H \times tL}{\Phi_0} = 1.05$ and is thus within 5% of a single flux quantum ($\Phi_0 = \frac{hc}{2e}$). This

is different from the result of measurements in an in-plane longitudinal H-field where the re-entrant behavior was gradual over an extended H-field regime.

Sample D was longer than sample C. As seen in Figure 6.13, there was a shift in the values of the H-fields at which both the $R(H)$ peak and the abrupt re-entrance were found. The $R(H)$ peak did not emerge out of the plateau. Instead, we observed peak signatures on the left hand side of $R(H)$ and on the negative side of the $R(H)$ plateau for $I \geq 9.2\mu A$. The reentrance occured at $H \pm 38Oe$ corresponding to $\frac{\Phi}{\Phi_0} = 0.42$ or within 5% of $\frac{\Phi}{\Phi_0} = \frac{2}{5}$.

6.4 Magnetic Field Tuned Reentrant Superconductivity in Aluminum Nanowires: Discussion

In both the in-plane longitudinal and transverse H-field, we completely suppressed superconductivity in the nanowire at larger H-fields as compared to the bulk H_C. In samples A and B at $T = 460mK$, the in-plane longitudinal critical field of the nanowire ($H_{C,NW,Lng.}$) is $H_{C,NW,Lng.} = 1300Oe$. On the other hand, the in-plane transverse critical field of the nanowire ($H_{C,NW,Trn.}$) which is $H_{C,NW,Trn.} = 800Oe$ in samples C and D at $T = 450mK$. The difference between the two configurations is $H_{C,NW,Lng.} \sim \frac{\Phi_0}{wt}$ while $H_{C,NW,Trn.} \sim \frac{\Phi_0}{\xi_{GL}t}$.[11]

We now discuss several possible mechanisms for the observed $R(H)$ peak and abrupt reentrance of samples C and D. We first consider the $R(H)$ peak. It is well known that in electronic systems of reduced dimensionality weak localization of electrons leads to a small, typically less than 1%, negative change in $R(H)$.[63] The percentage change in $R(H, T = 450mK)$ with $I = 8.4\mu A$, is roughly 12% from peak to plateau. As we increase the current, the percentage change increases. Thus, even when the peak is measurable, the change in $R(H)$ at constant current does not agree with the quasiparticle weak localization picture, which would predict a much smaller effect.

Previously, a similar $R(H)$ peak was reported in out-of-equilibrium superconducting Al nanowires.[32] The authors developed a model for the observed $R(H)$ peak near T_c by accounting for the H-field dependence of L_{QP}. In their case, they qualitatively compared their observed $R(H)$ peak with a non-Lorentzian peak function and suppressed the peak by increasing the current. In our case, we observed a Lorentzian form for $R(H)$ in Figure

6.12(a) and a more complicated current dependence as seen Figure 6.12(b) and 6.12(c).

In general, the normal metal-superconducting boundary resistance due charge conversion of a quasiparticle current to a supercurrent, I_S, depends on the quasiparticle lifetime, τ_{QP}. τ_{QP} depends upon the pair-breaking time (τ_{pb}) and the inelastic electron-phonon relaxation time (τ_E) at the Fermi surface.[20] In out-of-equilibrium superconductors, the H-field dependence of τ_{pb} is given by

$$1/\tau_{pb} = (1.76 k_B T_c/\hbar)(H/H_{c,NW,Trn.})^2 \tag{6.6}$$

Here $H_{c,NW,Trn.}(T = 0)$ is the zero temperature in-plane transverse critical field of the nanowire.[20] The presence of an H-field will reduce L_{QP}. Computing $\tau_{QP}(I, H)$ depends on the details of the microscopic model and experiment.[21, 20, 32] There is no universal form for τ_{QP}.

At large out-of-equilibrium values of current, the $(H - H_0)^2$ dependence of $R(H)$ is due to the H-field dependence of $1/\tau_{pb}$. H_0 is a phenomenological offset field. The peak height and full width at half maximum of $R(H)$ could be related to τ_E. In a short wire ($L < L_{QP}$), such as sample C, quasiparticles don't relax within its length. In a longer wire $L > L_{QP}$, such as sample D, quasiparticles do relax. Using an expression for $\tau_{QP}(T)$ valid near the critical current I_c for $H = 0Oe$

$$\tau_{QP} = 0.55(\frac{\hbar/\tau_{in}}{k_B T_c})^{1/2} \frac{T_c}{T_c - T} \tau_{in} \tag{6.7}$$

suggests that $L_{QP} \approx 1.7\mu m$ at $T = 450mK$ for both samples.[22] In addition, I_c may be enhanced in a H-field leading to a negative $R(H)$.[57] However, the main caveat is that both approaches compute $L_{QP}(T)$ and $I_c(H, T)$ using time-dependent Ginzburg-Landau theory, which is strictly valid only near T_c. Thus it is fair to state that we have no definitive explanation for the $R(H)$ peak.

We now turn to the matter of the abrupt in-plane transverse H-field re-entrance phenomenon. At this writing we have no detailed model to explain the data, only suggestions as to what might be involved. The apparent quantized reentrance behavior could be a signature of the phase sensitive nature of quasiparticles in Andreev bound states (ABS).[23, 25] The lead/nanowire/lead system could effectively be a long superconductor-normal metal-superconductor (S-N-S) Josephson junction when

the nanowire is out-of-equilibrium and resistive and the leads are superconducting. Then I_S would be carried between the two superconducting leads and through the nanowire by quasiparticles undergoing Andreev reflections at the nanowire/lead interfaces. The ABS energies, relative to E_F, for a S-N-S junction are given by

$$E_{A\pm}^{(n)} = \frac{\hbar v_F}{2L}(2\pi(n+1/2) \pm \gamma) \tag{6.8}$$

where v_F is the Fermi velocity, L is the length of the junction, n is an integer, and γ is the gauge invariant phase difference across the junction. [25] We can change the value of $E_{A\pm}^{(n)}$ by applying a H-field in the plane of the junction via $\gamma = \gamma_0 + 2\pi\frac{\Phi}{\Phi_0}$. [11] Pursuing the analogy between the lead/nanowire/lead system and a S-N-S junction, the flux dependence of γ could change the value of $E_{A\pm}^{(n)}$. A energy level shift like this may be the source of the relationship between the H-field at re-entrance and the flux quantum.

Alternatively, the abrupt reentrance in sample A could be due to a single vortex entering the nanowire and producing currents which go in the opposite direction to screening currents. This process would be similiar to the Little-Parks effect in superconducting loops where $T_C(H)$ is periodically enhanced when integer values of $\frac{\Phi}{\Phi_0}$ thread through the loop.[58] The Little-Parks effect also manifests itself as minima in $R(H)$ when $\frac{\Phi}{\Phi_0}$ is an integer for $T \lesssim T_c(H=0)$. However, in the nanowire, only a single vortex penetrates the nanowire and enhances T_c. Since ΔF_0 is of the form

$$\Delta F_0 = \frac{8\sqrt{2}}{3}\frac{H_c^2}{8\pi}A\xi \sim (1 - T/T_c)^{3/2} \tag{6.9}$$

When T_c increases, the energy barrier for thermally activated phase slips increases and thus the resistance drops.[11]

Furthermore, low H-field reentrance has been seen in mesoscopic superconducting Al loops.[59, 60] For H-fields such that $\frac{\Phi}{\Phi_0} < 2$, additional minima and maxima in $R(H)$ appeared and were termed anomalous Little-Parks oscillations or M-like anomalies.[59, 60] The authors found that the width of the M-shaped anomaly corresponded to a H-field value where $\frac{\Phi}{\Phi_0} = 1$ threaded through the area of the lines defining the loop.[60] Whether the reentrance mechanism in Samples C and D is related to this is not known at the time.

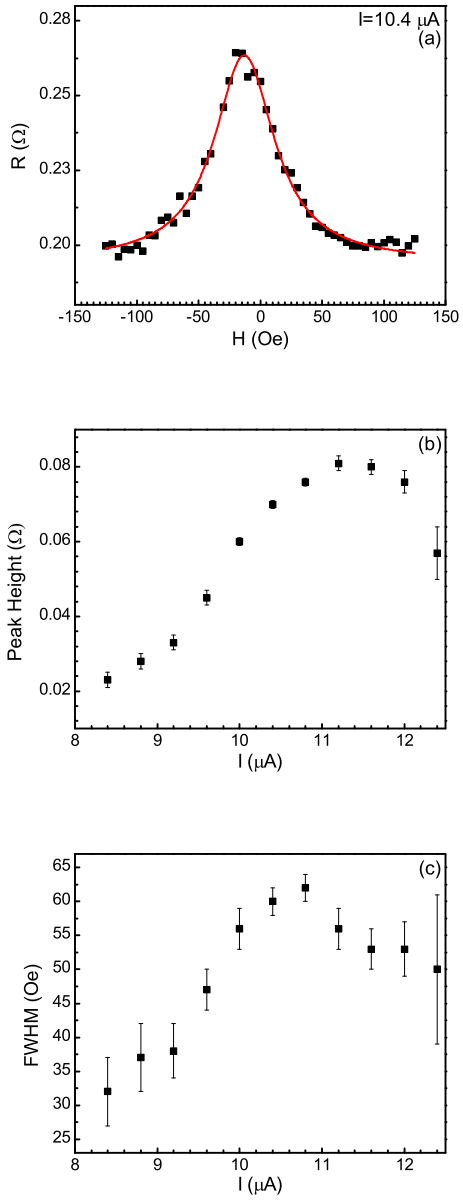

Figure 6.12: (a) Lorentzian fit of $R(H)$ for $I = 10.4\mu A$, (b) peak height and (c) full width at half maximum from the $R(H)$ fitting of sample C.

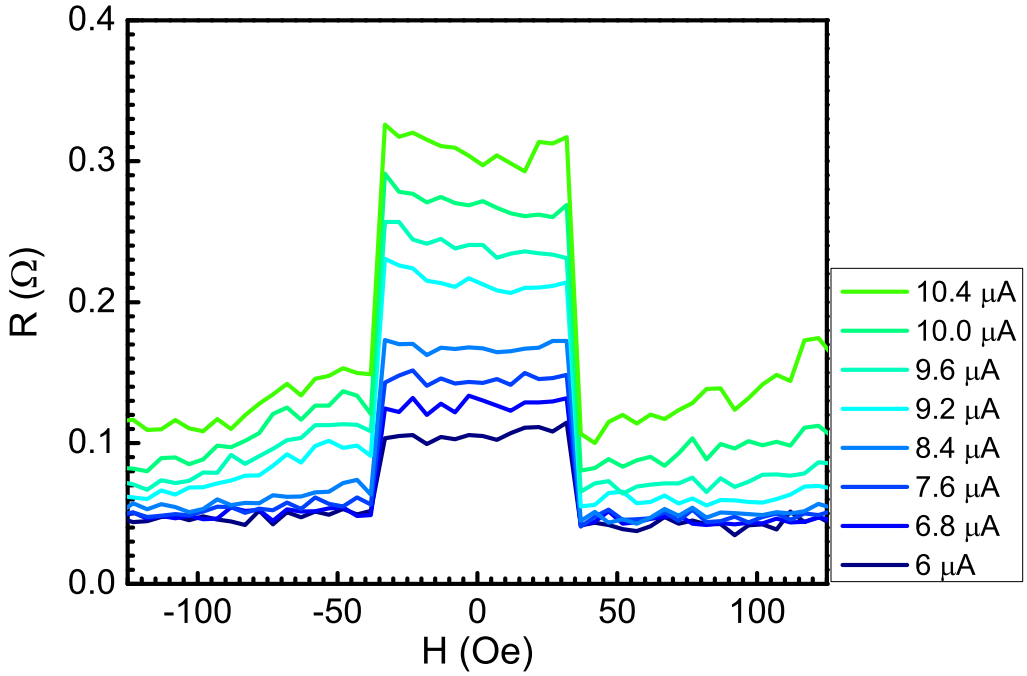

Figure 6.13: $R(H, T = 450mK)$ of sample D. Each color trace corresponds to a different applied current. The H-field was applied in-plane and transverse to the nanowire axis.

Chapter 7

Conclusion

In summary, we have measured the $I-V$ characteristics of IL gated $SrTiO_3$ nanowires as a function of temperature and V_G. Our measurements provide evidence of collective charge transport through the nanowire as exhibited in the dynamical critical behavior of the $I-V$ characteristic at low V_G and diffusive quasi-1D transport at high V_G. The tunability between these two unique transport regimes with an IL presents additional progress in understanding mesoscopic effects in IL gated $SrTiO_3$ nanostructures.

Future work in IL gating experiments on $SrTiO_3$ would be to replicate the classic experiments of the mesoscopic physics community.[1] For instance, if one could gate a nanoscale ring of undoped $SrTiO_3$ with an IL, one could examine Aharonov-Bohm oscillations in the magnetoresistance in the normal state and Little-Parks oscillations in the superconducting state.

In addition, we have observed magnetic field reentrant superconductivity in Al nanowires in an in-plane H-field orientation both longitudinal and transverse to the nanowire axis. Nanowires in an in-plane longitudinally oriented H-field exhibit behavior like that previously seen in Zn nanowires. The most striking feature of the behavior of nanowires in an in-plane transverse field is the abrupt reentrance to the superconducting state. It may be a consequence of the phase sensitive nature of Andreev bound states found in the system of the nanowire and superconducting leads or an interplay between vortex and screening currents in the nanowire. This study provides a further challenge to the theory of H-field tuned reentrant superconducivity in nanowires.

Future work investigating and controlling quasiparticle populations in superconducting nanowires using microwaves would ellucidate the mechanism for the abrupt reentrance to the superconducting state. If a shift in Andreev bound states is the source of the abrupt reentrance, then one could excite quasiparticles out of these states with microwave pulses as a function of static magnetic field. Indeed, measuring and controlling quasiparticle populations is of current interest to the superconducting qubit community since quasiparticles are the source of decoherence in superconducting qubits.[61, 62] Therefore, borrowing techniques from the superconducting qubit community would assist future reentrance measurements in superconducting nanowires.

References

[1] R.A. Webb and S. Washburn. Physics Today 41.12 (1988): 46-53.

[2] J. Clarke and F.K. Wilhelm, Nature (London) **453**, 1031 (2008).

[3] M.H. Devoret and R.J. Schoelkopf, Science **339**, 1169 (2013).

[4] M. A. Reed, J. N. Randall, R. J. Aggarwal, R. J. Matyi, T. M. Moore, and A. E. Wetsel, Phys. Rev. Lett., **60**, 535 (1988).

[5] L.P. Kouwenhoven, C.M. Marcus, P. L. McEuen, S. Taruch and R.M. Westervelt and N.S. Wingreen, *Electron Transport in Quantum Dots* (Springer, Netherlands, 1997).

[6] E. B. Foxman, P. L. McEuen, U. Meirav, N.S. Wingreen, Y. Meir, P. A. Belk, N. R. Belk, M. A. Kastner and S. J. Wind, Phys. Rev. B, **47**, 10020(R) (1993).

[7] A.A. Middleton and N.S. Wingreen, Phys. Rev. Lett.**71**, 3198 (1993).

[8] M. Kardar, G. Parisi and Y.-C. Zhang, Phys. Rev. Lett **56**, 889 (1986).

[9] Y. Imry, *Introduction to Mesoscopic Physics* (Oxford University Press, New York 2002), Second Edition.

[10] B. J. van Wees, H. van Houten, C. W. J. Beenakker, J. G. Williamson, L. P. Kouwenhoven, D. van der Marel and C. T. Foxon, Phys. Rev. Lett. **60**, 848 (1988).

[11] M. Tinkham, *Introduction to Superconductivity* (McGraw-Hill, New York, 1996), 2nd ed.

[12] H. K. Onnes, Comm. Phys. Lab. Univ. Leiden, **122**, 124 (1911).

[13] W. Meissner and R. Ochsenfeld, The Science of Nature, **21**, 44 (1933).

[14] J. Bardeen, L. N. Cooper and J. R. Schrieffer, Phys. Rev. **108**, 1175 (1957).

[15] W. A. Little, Phys. Rev. **156**, 396 (1967).

[16] J. S. Langer and V. Ambegaokar, Phys. Rev. **164**, 498 (1967); D. E. McCumber and B. I. Halperin, Phys. Rev. B **1**, 1054 (1970).

[17] N. Giordano, Phys. Rev. Lett. **61**, 2137 (1988).

[18] A. Bezryadin, C. N. Lau and M. Tinkham, Nature (London) **404**, 971 (2000).

[19] P. Santhanam, thesis (unpublished), Yale University (1985).

[20] A. M. Kadin, W. J. Skocpol, and M. Tinkham, J. Low Temp. Phys. **33**,481 (1978).

[21] A. Schmid and G. Schon, J. of Low Temp. Phys. **20**, 207 (1975).

[22] M. Stuivinga, J.E. Mooij, and T.M. Klapwijk, J. of Low Temp. Phys. **46**, 555 (1982).

[23] A.F. Andreev, Sov. Phys. JETP **22**, 455 (1966).

[24] G. E. Blonder, M. Tinkham, and T. M. Klapwijk, Phys. Rev. B **25**, 4515 (1982).

[25] I. O. Kulik, Sov. Phys. JETP **30**, 944 (1969).

[26] C. I. Duruoz, R. M. Clarke, C. M. Marcus, and J. S. Harris, Jr., Phys. Rev. Lett. **74**, 3237 (1995).

[27] A. J. Rimberg, T. R. Ho, and J. Clarke, Phys. Rev. Lett. **74**, 4714 (1995).

[28] R. Parthasarathy, X.M. Lin, and H. M. Jaeger, Phys. Rev. Lett. **87**, 186807 (2001).

[29] R. Parthasarathy, X.M. Lin, K. Elteto, T. F. Rosenbaum, and H. M. Jaeger, Phys. Rev. Lett. **92**, 076801 (2004).

[30] J. E. Lukens and R.J. Warburton and W.W. Webb, Phys. Rev. Lett. **25**, 1180 (1970).

[31] R. S. Newbower and M.R. Beasley and M. Tinkham, Phys. Rev. B, **5**, 864 (1972).

[32] P. Santhanam, C. P. Umbach, and C. C. Chi, Phys. Rev. B **40**, 11 392 (1989).

[33] M. L. Tian, N. Kumar, S.Y. Xu, J. G. Wang, J. S. Kurtz, and M. H.W. Chan, Phys. Rev. Lett. **95**, 076802 (2005); M. L. Tian, N. Kumar, J. Wang, S. Xu, and M. H.W. Chan, Phys. Rev. B **74**, 014515 (2006).

[34] Y. Chen, S.D. Snyder and A.M. Goldman, Phys. Rev. Lett. **103**, 127002 (2009); Y. Chen, S.D. Snyder and A.M. Goldman, Phys. Rev. B **83**, 054505 (2011).

[35] Y. Chen, Y.-H. Lin, S.D. Snyder, A.M. Goldman, and A. Kamenev, Nat. Phys. **10**, 567 (2014).

[36] B. Cord, Vistec EBPG Wiki, Minnesota Nanofabrication Center, University of Minnesota, `http://wiki.umn.edu/EBPG` (2015).

[37] B. Hafner, Scanning Electron Microscopy Primer, Characterization Facility, University of Minnesota, `http://www.charfac.umn.edu/instruments/sem_primer.pdf` (2015).

[38] M. Kawasaki, K. Takahashi, T. Maeda, R. Tsuchiya, M. Shinohara, O. Ishiyama, T. Yonezawa, M. Yoshimoto, and H. Koinuma, Science **226**, 1540 (1994).

[39] G. Koster, B. L. Kropman, G. J. H. M. Rijnders, D. H. A. Blank and H. Rogalla, Appl. Phys. Lett. **73**, 2920 (1998).

[40] D. W. Reagor and V. Y. Butko, Nature Materials **4**, 593 (2005).

[41] H. Yuan, H. Shimotani, A. Tsukazaki, A. Ohtomo, M. Kawasaki, and Y. Iwasa, Adv. Funct. Mater. **19**, 1046 (2009).

[42] C. H. Ahn, A. Bhattacharya, M. Di Ventra, J.N. Eckstein, C. Daniel Frisbie, M.E. Gershenson, A.M. Goldman, I.H. Inoue, J. Mannhart, A.J. Millis, A.F. Morpurgo, D. Natelson and J.-M. Triscone, Rev. Mod. Phys., **78**,1185 (2006).

[43] D.S. Fisher, Phys. Rev. Lett. **50**, 1486 (1983).

[44] N. Martys, M. Cieplak, and M. O. Robbins, Phys. Rev. Lett. **66**, 1058 (1991).

[45] D. S. Fisher, in *Nonlinearity in Condensed Matter*, edited by A. R. Bishop et al. (Springer-Verlag, New York, 1987).

[46] C. L. Kane and M. P. A. Fisher, Phys. Rev. Lett. **68**, 1220 (1992).

[47] A. Chang, L. Pfeiffer, and K. West, Phys. Rev. Lett. **77**, 2538 (1996).

[48] M. Bockrath, D .H. Cobden, J. Lu, A. G. Rinzler, R. E. Smalley, L. Balents and P. L. McEuen, Nature (London), **397**, 598 (1999).

[49] L. Venkataraman, Y. S. Hong, and P. Kim, Phys. Rev. Lett. **96**, 076601 (2006).

[50] V. V. Deshpande, M. Bockrath, L. I. Glazman, and A. Yacoby, Nature (London), **464**, 209 (2010).

[51] J. Nelson, K.V. Reich, M. Sammon, B.I. Shklovskii, and A.M. Goldman, Phys. Rev. B **92**, 085424 (2015).

[52] G. Gruner, Rev. Mod. Phys. **60**, 1129 (1988).

[53] J. H. F. Scott-Thomas, S. B. Field, M. A. Kastner, H. I. Smith, and D. A. Antoniadis, Phys. Rev. Lett. **62**, 583 (1989).

[54] R. C. Neville, B. Hoeneisen, and C. A. Mead, J. of Appl. Phys. **43**, 2124 (1972).

[55] K. A. Muller and H. Burkard, Phys. Rev. B **19**, 3593 (1979).

[56] S. W. Stanwyck, P. Gallagher, J. R. Williams, and D. Goldhaber-Gordon, Appl. Phys. Lett. **103**, 213504 (2013).

[57] D.Y. Vodolazov, Phys. Rev. B **75**, 184517 (2007).

[58] W. A. Little and R. D. Parks, Phys. Rev. Lett. **9**, 9 (1962).

[59] H. Vloeberghs, V. V. Moshchalkov, C. Van Haesendonck, R. Jonckheere, and Y. Bruynseraede, Phys. Rev. Lett **69**, 1268 (1992).

[60] V.V. Moshchalkov, L. Gielen, H. Vloeberghs, M. Dhallé, G. Neuttiens, R. Jonckheere, C. Van Haesendonck and Y. Bruynseraede, Appl. Superconductivity **1**, 391 (1993).

[61] E. M. Levenson-Falk, F. Kos, R. Vijay, L. Glazman, and I. Siddiqi, Phys. Rev. Lett. **112**, 047002 (2014).

[62] C. Wang, Y.Y. Gao, I.M. Pop, U. Vool, C. Axline, T. Brecht, R.W. Heeres, L. Frunzio, M.H. Devoret, G. Catelani, L.I. Glazman and R.J. Schoelkopf, Nature Comm. **5**, (2014).

[63] J. C. Licini, G. J. Dolan, and D. J. Bishop, Phys. Rev. Lett. **54**, 1585 (1985).

[64] K. Ueno, T. Nojima, S. Yonezawa, M. Kawasaki, Y. Iwasa, and Y. Maeno, Phys. Rev. B **89**, 020508(R) (2014).

[65] M. Eden, in Proceedings of the Fourth Berkeley Symposium on Mathematieal Statistics and Probability, edited by F. Neyman (University of California, Berkeley, 1961), Vol. IV.

[66] R. Landauer, IBM Journal of Research and Development **1**, 223 (1957).

[67] G. Deutscher, Rev. Mod. Phys. **77**, 109 (2005).

[68] L.P. Gor'kov, Zh. Eksperim. i. Teor. Fix **36**, 1918 (1959) [Soviet Phys. - JETP **9**, 1364 (1959)].

[69] P.G. deGennes, *Superconductivity of Metals and Alloys* 2nd ed (Addison-Wesley Publishing Co., Inc., 1989).

[70] C.M. Varma, J. Low Temp. Phys. **126**, 901 (2002).

[71] S.D. Synder, thesis (unpublished), University of Minnesota (2012).

[72] Quantum Design Inc., Quantum Design PPMS brochure, http://www.qdusa.com/sitedocs/productBrochures/1070-002.pdf (2016).

[73] B.D. Josephson, Phys. Lett **1**, 251 (1962).

[74] B.D. Josephson, Adv. Phys. **14**, 419 (1965).

[75] S. Tomonaga, Prog. Theor. Phys. **5**, 544 (1950).

[76] J. M. Luttinger, J. Math. Phys. **4**, 1154 (1963).

[77] M. Lee, J. R. Williams, S. Zhang, C. D. Frisbie, and D. Goldhaber-Gordon, Phys. Rev. Lett. **107**, 256601 (2011).

[78] M. Li, T. Graf, T. D. Schladt, X. Jiang, and S. S. P. Parkin, Phys. Rev. Lett. **109**, 196803 (2012).

[79] T.M. Bretz-Sullivan and A.M. Goldman, Appl. Phys. Lett. **107**, 113106 (2015).

[80] T.M. Bretz-Sullivan and A.M. Goldman, Phys. Rev. B **93**, 184509 (2016).